W&M ScholarWorks

2011

Quantum turbulence in two dimensional Bose-Einstein condensates

Bo Zhang
College of William & Mary - Arts & Sciences

Follow this and additional works at: https://scholarworks.wm.edu/etd

Part of the Condensed Matter Physics Commons

Recommended Citation

QUANTUM TURBULENCE IN TWO DIMENSIONAL BOSE-EINSTEIN CONDENSATES

Bo Zhang

Tai An, Shan Dong, China

Master of Science, College of Willam and Mary, 2006
Bachelor of Science, Beijing Normal University, 2004

A Dissertation presented to the Graduate Faculty
of the College of William and Mary in Candidacy for the Degree of
Doctor of Philosophy

Department of Physics

The College of William and Mary
May 2011

APPROVAL PAGE

This Dissertation is submitted in partial fulfillment of
the requirements for the degree of

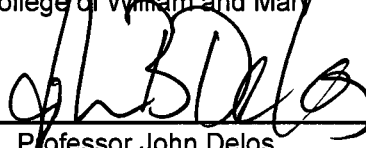Doctor of Philosophy

Bo Zhang

Approved by the Committee, January, 2011

Committee Chair
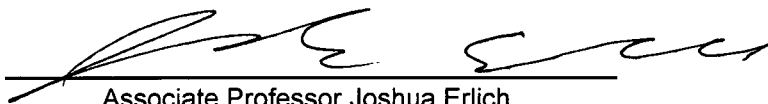Professor George Vahala
Department of Physics
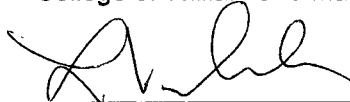College of William and Mary

Assistant Professor Seth Aubin
Department of Physics
College of William and Mary

Professor John Delos
Department of Physics
College of William and Mary

Associate Professor Joshua Erlich
Department of Physics
College of William and Mary

Associate Professor Linda Vahala
Electrical and Computer Engineering
Old Dominion University

ABSTRACT PAGE

We examine the energy cascades and quantum vortex structures in two-dimensional quantum turbulence through a special unitary time evolution algorithm. An early attempt at using the Lattice Boltzmann Method proved successful in correctly representing some features of the Nonlinear Schrodinger System (NLS), such as the phase shift following the one-dimensional soliton-soliton collision, as well as the two-dimentional modulation instability. However, to accurately evaluate NLS, the implicit Euler method is required to resolve the time evolution, which is computationally expensive. A more accurate and efficient method, the Quantum Lattice Gas model is employed to simulate the quantum turbulence governed by the Gross-Pitaevskii equation, an equaiton that describes the evolution of the ground state wave function for a Bose-Einstein condensate (BEC). It is discovered that when the ratio of the internal energy to the kinetic energy is below 0.05, an unexpected short Poincare recurrence occurs independent of the initial profile of the wave function. It is demonstrated that this short recurrence is destroyed as the internal energy is strengthened. To compare the two-dimensional quantum turbulence with its classical counterpart, the incompressible energy spectra of quantum turbulence is analyzed. However, the result reveals no sign of dual cascades which is a hallmark of the classical incompressible two-dimensional fluid (inverse energy cascade to large scales with a direct cascade of enstrophy to small scales). It is the spectra of the compressible energy that can exhibits multiple cascades, but this is strongly dependent on the initial condition.

To Father, Mother and peta-scale

TABLE OF CONTENTS

ACKNOWLEDGMENTS

LIST OF TABLES

LIST OF FIGURES

CHAPTER 1

Introduction

The classical incompressible fluid is characterized by the only dimensionless parameter - the Reynolds number, which is defined as $R = \dfrac{\lambda_s u}{\nu}$. λ_s is the characteristic length of the system, u is the mean velocity and ν is the viscosity. As R increases, a classical fluid undergoes greater instability. When R reaches the critical value R_T, the fluid transforms from laminar flow to turbulence, c.f. 1.1. Turbulent flow is chaotic and unpredictable. A complete understanding of turbulence presents a great challenge to the scientific community [3]. One difficulty among the many challenges is that the vortex in classical turbulence is not well defined. The vorticity is continuous and the size of each vortex is difficult to determine. However, in the quantum turbulence, which is loosely defined as the tangles of vortex lines (in three dimension) or irregularly/regularly distributed vortices (in two dimension), the circulation of the vortex is quantized and the size of vortex could be well characterize by the coherence length. More importantly, the embodiments of quantum turbulence, superfluid helium or dilute Bose-Einstein Condensate (BEC) gas, exhibit zero viscosity which is equivalent to $R = \infty$. This makes quantum turbulence an almost ideal example for understanding classical turbulence [4, 5]. Analysis of the energy transfer

among different scales in quantum turbulence may shed some light on understanding the existence of energy cascades in classical turbulence.
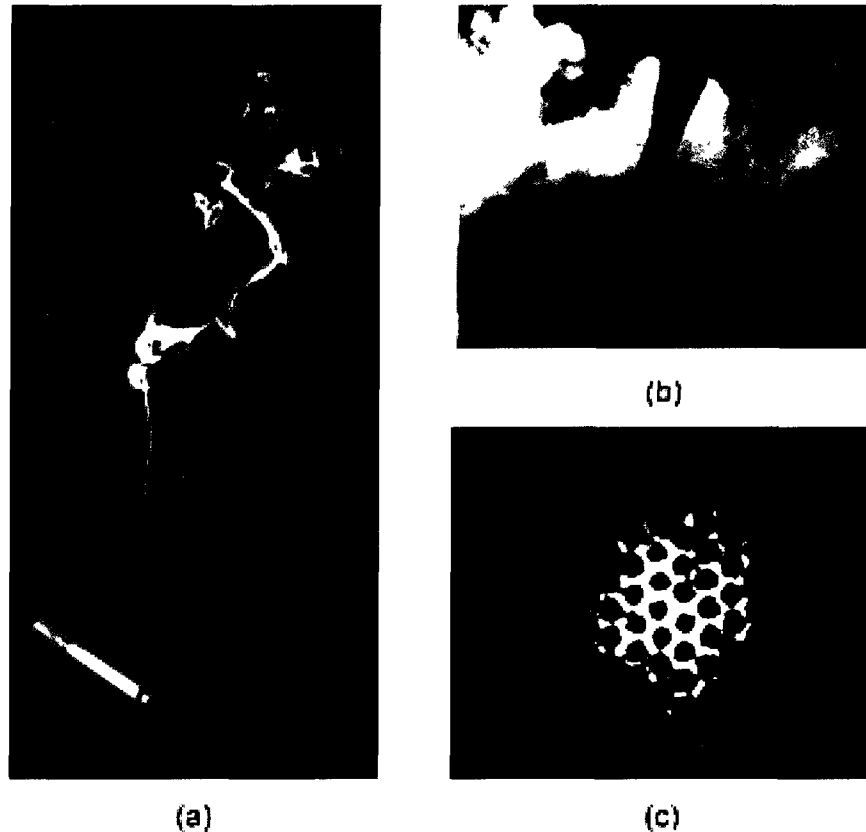
FIG. 1.1: (a): The transition from laminar flow to the turbulence. (b): a classical vortex in nature. (c): quantum vortex lattice in BEC, credit: Eric Cornell group.

Recently, *Henn et al.* have reported that the turbulent driven BEC gas experiences a different expansion pattern than the normal BEC gas [ ]. Once the anisotropic trap is removed, the normal BEC gas undergoes "ratio inversion" [ ] as illustrated in Fig 1.2. For the turbulent driving BEC gas, the x-y ratio during the expansion remains almost the same as the initial value. A more thorough examination of quantum turbulence will help explain this novel feature of the BEC gas.
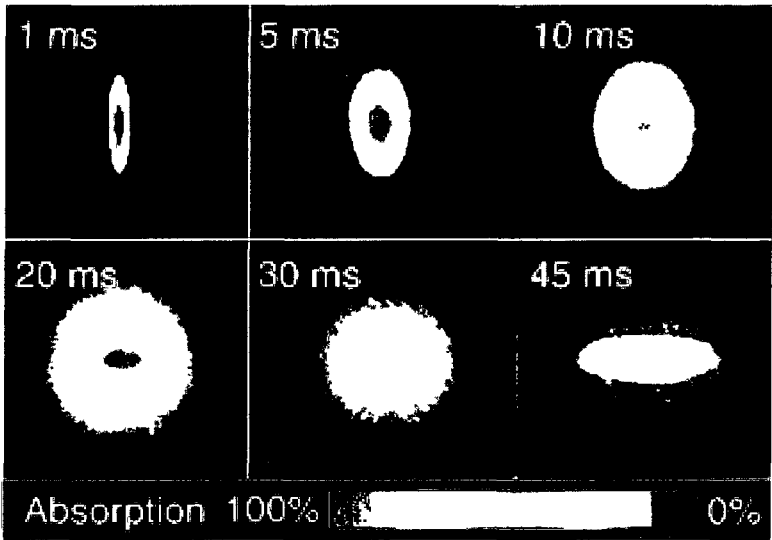
FIG. 1.2: Time-of-flight expansion of a BEC. Credit: Wolfgang Ketterle group, MIT, 1996

The x-y ratio of the trapped BEC cloud is inverted after the trap is turned off to allow the gas freely expands.

This dissertation is organized as follows: in Chap 2, a general theoretical description of quantum turbulence is given; In Chap 3, an early attempt of the Lattice Boltzmann model (LBM) is carried out to simulate some nonlinear Schrödinger systems; Chap 4 explains the construction of the Quantum Lattice Gas method (QLG), which is more accurate and stable than LBM; Chap 5 and Chap 6 present the numerical results obtained under the condition of weak interaction and medium interaction, with focus on the unexpected Poincaré recurrence and the energy cascades in 2D quantum turbulence; Chap 7 concludes this thesis.

CHAPTER 2

Theoretical model for dilute BEC gas

2.1 Gross-Pitaevskii Equation

The interaction between atoms in a ground-state BEC gas can be effectively described by the Dirac δ function: $g_0\delta(\mathbf{r} - \mathbf{r}')$. The coupling constant $g_0 = \dfrac{4\pi\hbar^2 a_s}{m}$, with a_s being the scattering length. The total energy of the system, under a mean-field approach, is:

$$E = N \int d\mathbf{r}[\frac{\hbar^2}{2m}|\nabla\psi|^2 + \frac{g_0 N}{2}|\psi|^4 + V(\mathbf{r})|\psi|^2],\tag{2.1}$$

$V(\mathbf{r})$ being the external potential, and N being the number of particle. The normalization condition for ψ is $\int d\mathbf{r}|\psi|^2 = 1$. The time independent wave function ψ must minimize the total energy of the system while conserving the total number of particles. Applying the variational method to Eq 2.1, one obtains the time independent Gross-Pitaevskii equation:

$$\mu\psi = -\frac{\hbar^2}{2m}\nabla^2\psi + V(\mathbf{r})\psi + g_0 N|\psi|^2\psi,\tag{2.2}$$

where μ is chemical potential which appears as the Lagrangian multiplier.

The time dependent GPE could be derived by minimizing the action of the Schrodinger

field. The lagrangian density governing the GP system reads:

$$\mathscr{L} = \frac{i\hbar}{2}(\bar{\psi}\partial_t\psi - \psi\partial_t\bar{\psi}) - [\frac{\hbar^2}{2m}|\nabla\psi|^2 + \frac{g_0 N}{2}|\psi|^4 + V(\mathbf{r})|\psi|^2]. \qquad (2.3)$$

The Euler-Lagrangian equation from $\mathscr{L}$ gives the time dependent GPE:

$$i\hbar\partial_t\psi = -\frac{\hbar^2}{2m}\nabla^2\psi + V(\mathbf{r})\psi + g_0 N|\psi|^2\psi. \qquad (2.4)$$

The stationary solution to Eq 2.4 is:

$$\psi(\mathbf{r}, t) = e^{-i\mu t/\hbar}\psi(\mathbf{r}),$$

which produces Eq 2.2. The inclusion of $e^{i\mu/\hbar}$ is due to the fact that the total energy is reduced by μ when one boson is removed from the system. This clearly manifests that the GP equation is a description of a many body system rather than a single particle.

It is important to notice that the GPE described above is defined on 3D space. The BEC can not be developed in 2 or 1 dimension without an external potential [8]. This could also be seen from the dimension of the coupling constant g_0. Only in 3D, g_0 has the proper unit: $[g_0] = energy \times length^3$. However, for the 3D BEC gas, if the external potential is sufficiently strong along one dimension, for example, along the z-direction, a large energy gap $\Delta E = \hbar\omega_z \equiv \frac{\hbar^2}{ma_z^2}$ will be introduced to prevent excitation in z-direction, where a_z is the characteristic length scale for the trap in the z-direction. With the degree of freedom in z-direction being frozen, the wave function could be separated as: $\psi(\mathbf{r}) = \psi(\mathbf{x})\psi(z)$, and the 3D BEC gas can be effectively treated as a 2D phenomenon. Accordingly, the 2D time dependent GPE reads:

$$i\hbar\partial_t\psi(\mathbf{x}, t) = -\frac{\hbar^2}{2m}\nabla^2\psi(\mathbf{x}, t) + V(\mathbf{x})\psi(\mathbf{x}, t) + g_{2D}N|\psi(\mathbf{x}, t)|^2\psi(\mathbf{x}, t), \qquad (2.5)$$

with $g_{2D} = \frac{g_0}{a_z}$ being the 2D coupling constant.

2.2 Scaling of GPE

A GP system can be characterized by multiple scales. The proper scaling is important for numerical simulations to correctly reflect the dynamics and structure of a BEC gas. When the external potential is absent, the behavior of a GP system is dominated by 2 competing factors: the kinetic energy and the internal interaction. When the kinetic energy dominates, the system could be treated as a diffusive one. On the other hand, when the energy is mainly composed of internal energy, the *Thomas-Fermi* approximation is valid, which states that the density is almost a constant: $\rho(\mathbf{r}) \simeq \dfrac{\mu}{g_{2D}N}$ and the kinetic energy is negligible. Therefore it is beneficial to introduce the length scale: the *coherence length* ξ to characterize the system. At the scale $l \sim \xi$, the kinetic energy and internal energy are at the same order. By equating the two energy terms, one obtains $\xi(\mathbf{x}) = \dfrac{\hbar}{\sqrt{2mg_{2D}N|\psi(\mathbf{x})|^2}}$.

For quantum fluid studies, it is convenient to represent the spatial dependent density $|\psi(\mathbf{x})|^2$ by the bulk density of the system ρ_0. After this substitution, ξ can well characterize the size of the vortices, as we shall see in Sect 2.3. The bulk density ρ_0 is proportional to the chemical potential $\mu = g_{2d}N\rho_0$. Under this treatment, $\xi = \dfrac{\hbar}{\sqrt{2m\mu}}$ becomes a constant, which could be used as the scaling unit for a GP system. The characteristic frequency could be chosen as $\omega_0 = \dfrac{\mu}{\hbar}$, which is the frequency for the stationary state.

Perform the following scaling:

$$\mathbf{x} \to \mathbf{x}\xi,$$

$$t \to t/\omega_0,$$

$$\psi \to \psi/\xi$$

one can obtain the dimensionless GPE:

$$i\partial_t\psi = -\nabla^2\psi + g|\psi|^2\psi. \tag{2.6}$$

The definition of the dimensionless parameter g is: $g \equiv \dfrac{g_{2D} N}{\hbar \omega_0} = \dfrac{1}{\rho_0 \xi^2}$. For a weakly coupled 2D GP system, $g \ll 1$, which indicates $\xi \gg a$ with a being the averaged inter-particle distance. This is consistent with the 3D weakly coupled BEC gas. Notice that the derivation above is under the normalization restraint: $\rho_0 L^2 = 1$, L being the size of the system. For the convenience of computation, the normalization constant could be some value other than 1. Therefore if the normalization constant $\alpha \equiv \rho_0 L^2 \ll 1$, the dimensionless coupling constant g could be of the order $\mathcal{O}[1]$ while the system is still weakly interacting in nature.

2.3 Hydrodynamic Description

To have a better understanding of the quantum fluid, the Madelung transformation $\psi = \sqrt{\rho} e^{i\phi/2}$ is applied to Eq 2.6, and the GPE is now transformed into the following coupled equations:

$$\partial_t \rho + \nabla \cdot (\rho \nabla \phi) = 0; \tag{2.7}$$

$$\partial_t \phi + \frac{1}{2}(\nabla \phi)^2 + 2g\,\rho - 2\frac{\nabla^2 \sqrt{\rho}}{\sqrt{\rho}} = 0. \tag{2.8}$$

If one defines velocity $\mathbf{v} \equiv \nabla \phi$, equation Eq 2.7 is recognized as the continuity equation of the fluid, and the second equation Eq 2.8 is identified as the Bernoulli equation for an inviscid irrotational fluid for which the vorticity $\omega \equiv \nabla \times \mathbf{v} = 0$. Moreover, the pressure can be identified as:

$$p(\rho) = 2g\rho^2 - 2\sqrt{\rho}\nabla^2\sqrt{\rho},$$

a function purely dependent on density, which is a characteristic of a barometric fluid. Notice that the above analogy is only valid provided the wave function is smooth and well behaved.

When the scattering length is positive ($a_s > 0$), the atom-atom interaction is repulsive and admits the vortex solution. For the single line vortex, the amplitude is axisymmetric on the 2D plane and obeys the Dirichelet boundary condition: $|\psi(r = 0)| = 0$, $|\psi(r \rightarrow \infty)| = \mu/g$. The circulation of the quantum vortex is quantized: $\Gamma = \oint_c d\mathbf{l} \cdot \mathbf{v} = 4n\pi$, n is the winding number of the vortex. If the path $\oint_c$ does not encircle the vortex core, the circulation $\Gamma = 0$. Equivalently, the vorticity is a Dirac-δ function:$\omega = \nabla \times \mathbf{v} = \Gamma\delta(\mathbf{x} - \mathbf{x_0})$ with $\psi(\mathbf{x_0}) = 0$. For the vortex solution with winding number $n = 1$, the asymptotic behavior for the wave function $\psi = A(r)e^{i\theta}$ is:

$$r \rightarrow 0 : A(r) \sim r$$
$$r \rightarrow \infty : A(r) \sim 1 - \frac{1}{2r^2}.$$

Based on this asymptotic solution, a Padé approximation [9], ref Appendix B is constructed. From Fig 2.1, it could be seen that at the scale $x \sim \xi$, the wave function ap-
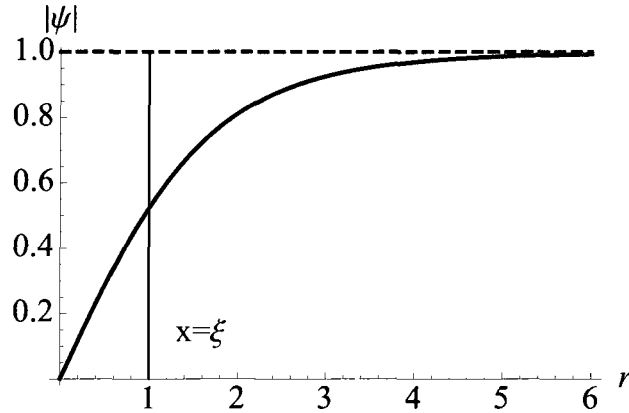
FIG. 2.1: Vortex amplitude at radial direction

This result is obtained via Padé approximation for winding number 1 and $\mu = g = 1$. $|\psi(r = \xi)| = 0.523|\psi(r = \infty)|$, $|\psi(r = \infty)| = 1$.

proaches its bulk value.

For a vortex with a winding number n, the line energy density, to logrithm accuracy, is estimated to be [8] $\varepsilon \sim n^2 \ln(\frac{D}{n\xi})$, with D being the scale of the system and $D \gg \xi$. The vortex with a large winding number has higher energy. Therefore, a vortex with winding number $n = l$ is unstable and it will split into l vortices with winding number $n = 1$. Equivalently, it is energetically unfavorable for two vortices with the same winding number to merge. This is in contrast with the vortex behavior in 2D classical turbulence, in which case the vortices with same rotation tend to merge and form larger eddies due to the presence of the viscosity.

The wave function of the vortex is smooth. However, the direction of the velocity is not well defined at the vortex core and the amplitude of the velocity diverges: $\mathbf{v} \sim 2e_\theta/r$. Therefore the Bernoulli equation Eq 2.8 is inconvenient for analyzing the vortex dynamics and turbulence. To circumvent this obstacle, we adopt Nore's approach [10]: to derive the conservation laws from Noether theory.

The invariance of $\mathscr{L}$ Eq 2.3 with respect to the phase rotation, space translation and time translation yields the mass conservation, momentum conservation and energy conservation respectively. Here we list these conservation laws derived by Nore et al when $V = 0$ and the validation of these results are given in Appendix A as well as the inclusion of an external potential:

$$\partial_t \rho + \nabla \cdot [\rho \mathbf{v}] = 0 \; ; \tag{2.9}$$

$$\partial_t(\rho \mathbf{v}) + \nabla \cdot [\rho \mathbf{v} \otimes \mathbf{v} + 4\nabla\sqrt{\rho} \otimes \nabla\sqrt{\rho} + (g\rho^2 - \nabla^2\rho)\,\mathbb{1}] = 0 \; ; \tag{2.10}$$

$$\partial_t(\frac{1}{2}\rho|\mathbf{v}|^2 + g\rho^2 + 2|\nabla\sqrt{\rho}|^2) = \tag{2.11}$$

$$- \nabla \cdot [\,2g\rho^2\mathbf{v} + \frac{1}{2}\rho\mathbf{v}\,|\mathbf{v}|^2 + \frac{1}{\rho}\nabla \cdot (\rho\mathbf{v})\nabla\rho - 2\sqrt{\rho}\mathbf{v}\,\nabla^2\sqrt{\rho}\,].$$

In the above formulas, $\mathbb{1}$ is an identity matrix, $\rho \equiv |\psi|^2$ is the probability density, $\rho\mathbf{v} \equiv i(\psi\nabla\bar{\psi} - c.c.)$ is the probability current. Around the origin $r \sim 0$, it is obvious that Eq 2.9

is well behaved. In Eq 2.10, the troubling terms as $r \to 0$ are:

$$\rho \mathbf{v} \otimes \mathbf{v} \sim 4 \mathbf{e}_\theta \otimes \mathbf{e}_\theta;$$

$$4 \nabla \sqrt{\rho} \otimes \nabla \sqrt{\rho} \sim 4 \mathbf{e}_r \otimes \mathbf{e}_r,$$

both of which are ill defined. However, the sum of these two terms is finite: $\mathbf{e}_r \otimes \mathbf{e}_r + \mathbf{e}_\theta \otimes \mathbf{e}_\theta = \mathbb{1}$. In Eq 2.11, the ill defined terms are:

$$\frac{1}{2} \rho \mathbf{v} |\mathbf{v}|^2 \sim 4 \frac{\mathbf{e}_\theta}{r},$$

$$2 \sqrt{\rho} \, \mathbf{v} \, \nabla^2 \sqrt{\rho} \sim 4 \frac{\mathbf{e}_\theta}{r},$$

the difference of which is zero as $r \to 0$. Therefore, all three conservation laws defined above are well behaved over all the domain. To see the connection between the GPE governed quantum fluid and the classical fluid, one could combine Eq 2.9 and Eq 2.10 and obtain the following equation:

$$\rho(\partial_t \mathbf{v} + \mathbf{v} \cdot \nabla \mathbf{v}) = -2\rho \nabla (g\rho - \frac{\nabla^2 \sqrt{\rho}}{\sqrt{\rho}}), \qquad (2.12)$$

which is the Euler equation for a inviscid barotropic fluid. The pressure consists of two parts: $2g\rho$ is the classical pressure term and $-2\dfrac{\nabla^2 \sqrt{\rho}}{\sqrt{\rho}}$ is the quantum pressure. Based on the energy conservation Eq A.3 in Appendix A, one could decompose the energy into four constituents, namely:

$$\textit{kinetic energy:} \quad E_{kin} = \int d\mathbf{x} \rho |\mathbf{v}|^2$$

$$\textit{internal enerngy:} \quad E_{int} = 2g \int d\mathbf{x} \rho^2$$

$$\textit{quantum energy:} \quad E_{qua} = 4 \int d\mathbf{x} |\nabla \sqrt{\rho}|^2$$

$$\textit{external potential:} \quad E_{ext} = 4 \int d\mathbf{x} V \rho.$$

When the external potential is not explicitly dependent on time, the total energy is conserved, which is pivotal for validating the numerical simulations.

One important feature of the GP fluid is its compressibility. In classical compressible fluids, the compressibility enables the formation of sound waves which could persist in the fluid. A similar property also exists in a GP fluid. Assume that $\{\rho_0(\mathbf{x}, t), \mathbf{v}(\mathbf{x}, t)\}$ is the solution to the fluid equations Eq 2.9 and Eq 2.10. Furthermore, assume the solution $\rho_0(\mathbf{x}, t)$ is smooth, and slowly varying in the configuration space, i.e. the variation of density is small over a unit distance: $\dfrac{|\nabla \rho_0|}{\rho_0} \ll 1$. Since the velocity $\mathbf{v}$ is defined as $\dfrac{1}{\rho_0} Im[\psi \nabla \bar{\psi}]$, it is also of order $\dfrac{|\nabla \rho_0|}{\rho_0}$. Therefore the velocity can be treated as a small quantity compared with the density. Now consider a small perturbation to the solution ρ_0: $\delta \rho$, which is of the same order as $\mathbf{v}$. If a small perturbation of the probability density ρ_0 could persist in the system, it must satisfy (at least initially) the linearized fluid equations:

$$\partial_t(\delta \rho) + \nabla \cdot [\rho_0 \mathbf{v}] = 0; \tag{2.13}$$

$$\partial_t(\rho_0 \mathbf{v}) = -g\rho_0 \nabla(\delta \rho) + \nabla^2 \nabla(\delta \rho). \tag{2.14}$$

A plane wave-like solution of Eq 2.13 of the form $\delta \rho = e^{-i\omega t + i\mathbf{k} \cdot \mathbf{x}}$ yields the dispersion relation:

$$\omega^2 = g\rho_0\, k^2 + k^4. \tag{2.15}$$

This is the *Bogoliubov dispersion relation* used to describe weak elementary excitations in quantum fluid. At low wave number, Eq 2.15 reduces to $\omega = \sqrt{g\rho_0}k$, which is the dispersion relation for sound wave. The sound wave plays an important role in the decay of 2D quantum turbulence, as we shall see in Chap 6.

2.4 Energy cascade in turbulence

2.4.1 3D Classical turbulence

The motion of fully developed classical incompressible turbulence can be character-ized by the existence of eddies of all sizes. The energy dissipation can be described by the *Richardson cascade*, which states that in the inertial range, energy transfers with negligible loss from the largest eddies to the smaller eddies until they are of size λ_0. Below the scale λ_0, the energy dissipates via viscosity and is transformed into heat. Based on the *Richard-son cascade* scenario, the energy dissipation in turbulence could be categorized into three ranges:

- Energy range: $l \sim \lambda_s$, this range contains most energy of the system;

- Inertial range: $\lambda_s > l > \lambda_0$, this is the range for energy transfer into smaller scales with almost no loss;

- Dissipation range: $l \sim \lambda_0$, viscosity transforms the kinetic energy of small eddies into heat.

Another important property of fully developed turbulence is that the angular momentum of the system is mostly carried by the largest eddies. At the scales within the inertial range, the turbulence becomes more and more isotropic. To estimate the energy distribution at the various scales in turbulence, a self-similar structure is assumed, which states that the fluctuation of velocity over different scale follows the equation:

$$\delta \mathbf{v}(\mathbf{r}) \equiv \mathbf{v}(\mathbf{r} + \mathbf{r}_0) - \mathbf{v}(\mathbf{r}_0) = \lambda^{-\beta} \delta \mathbf{v}(\lambda \mathbf{r}),$$

both λ, β being dimensionless numbers. Based on the assumed incompressibility, self-similarity and isotropy of the turbulence, dimensional analysis reveals that the energy den-
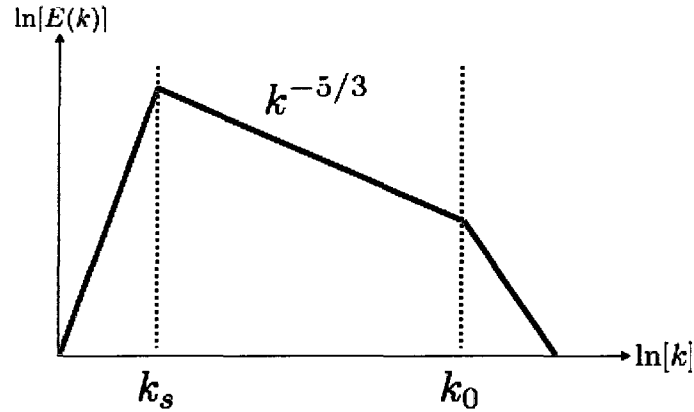
FIG. 2.2: Cascades in 3D classical turbulence.

Energy range (green line): $k < k_s$; Inertial range (blue line): $k_s > k > k_0$; Dissipation range (red line): $k > k_0$.

sity per unit mass $E(k)$ has the simple form [11]:

$$E(k) = C\epsilon_d^{2/3} k^{-5/3}, \tag{2.16}$$

where C is a constant, ϵ_d is the energy flux $\epsilon_d = \dfrac{\Delta u^3}{\lambda_s}$, with the dimension $\dfrac{Length^2}{Time^3}$. The quantity Δu is the velocity fluctuation over the system size λ_s. Notice that ϵ_d is defined upon large scale quantity, it is k independent in the inertial range. This formula was first obtained by Kolmogorov in 1941 [12, 13] and has been verified experimentally [14]. A schematic plots is shown in Fig 2.2 to illustrate the Kolmogorov cascades in fully developed turbulence.

2.4.2 2D classical turbulence

In incompressible 2D classical turbulence, there exists another important constant of motion in the inertial range besides energy: the enstrophy, which is defined as the total squared vorticity: $Z = \int d\mathbf{x} |\nabla \times \mathbf{v}|^2$. The conservation of both kinetic energy and enstro-

phy fundamentally alters the behavior of the 2D turbulence.

In Fourier space, the energy balance equation derived from the Navier-Stokes equation is [15]:

$$(\partial_t + 2\nu k^2)\varepsilon(k) = T(k),$$

$\varepsilon(k)$ is energy density and $T(k)$ is energy transfer rate which solely consists of triad interactions. In the inertial range, $T(k)$ satisfies $\int dk\, T(k) = 0$ and $\int dk\, k^2 T(k) = 0$. The conservation of energy and enstrophy then reads:

$$Energy\ conservation\ :\ \frac{d}{dt}\int_0^\infty dk\,\varepsilon(k) = -2\nu\int dk\,k^2\varepsilon(k);$$
$$Enstrophy\ conservation\ :\ \frac{d}{dt}\int_0^\infty dk\,k^2\varepsilon(k) = -2\nu\int dk\,k^4\varepsilon(k).$$

When the effect of viscosity ν is negligible, the total energy and enstrophy are conserved. Assume that at $t = 0$, energy and enstrophy are injected at some wavenumber $k = k_0$. At $t = T$, the energy and enstrophy spread into two narrow range $[k_1, k_1 + \delta k]$, $[k_2, k_2 + \delta k]$ with $k_1 < k_0 < k_2$. The conservation requires that

$$\varepsilon(k_0) = \varepsilon(k_1) + \varepsilon(k_2);$$
$$k_0^2\varepsilon(k_0) = k_1^2\varepsilon(k_1) + k_2^2\varepsilon(k_2).$$

The ratios for the energy and enstrophy between k_1 and k_2 are:

$$\frac{\varepsilon(k_1)}{\varepsilon(k_2)} = \frac{k_2^2 - k^2}{k^2 - k_1^2};$$
$$\frac{k_1^2\varepsilon(k_1)}{k_2^2\varepsilon(k_2)} = \frac{k_1^2(k_2^2 - k^2)}{k_2^2(k^2 - k_1^2)}.$$

Since $k_1 < k_2$, more energy is transferred to k_1 than enstrophy. Accordingly, more enstrophy cascades to high k than energy [16]. A more rigorous analysis has been done by R.Kraichnan [15] and G.K.Batchelor [17]. Based upon the assumption of incompressibility, isotropy and self-similarity, it can be demonstrated that there exists dual cascade in the

inertial range, namely the inverse energy cascade and the direct enstrophy cascade:

$$Inverse\ cascade: \varepsilon(k) \propto k^{-5/3};$$

$$Direct\ cascade: \varepsilon(k) \propto k^{-3}.$$

The existence of dual cascade is a unique feature of 2D turbulence. On one hand, the
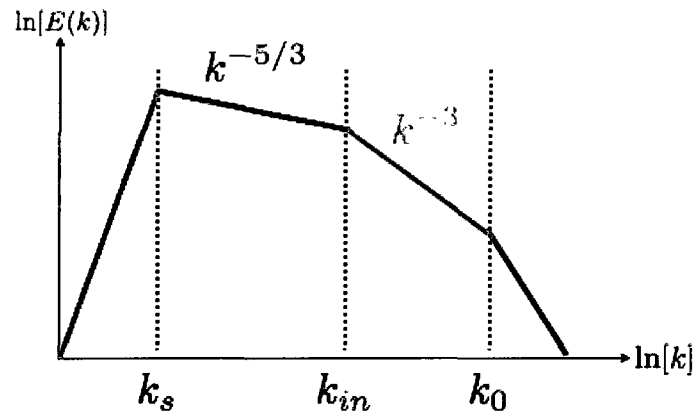
FIG. 2.3: Dual cascade in 2D turbulence.

The inertial range is split into two distinct regime: inverse cascade (blue line) and direct cascade (cyan). At the scale k_s, the size of the system prevents the formation of larger eddies, while at k_0, dissipation becomes important. K_{in} is the energy/enstrophy injection range.

inverse cascade dictates that the energy is transferred to larger scales, which is manifested by the coalescence of eddies. When the eddies grow in size, they are less susceptible to viscous dissipation, until the eddies matches the system size and subject to the boundaries. On the other hand, the direct cascade determines the vorticity which is cascaded to smaller scales. This leads to formation of small swirls at the boundary of the large eddies which carries the energy. When the size of the small eddies reaches the inertial limit, the vorticity is dissipated away through viscosity. This dual cascades is schematically displayed in Fig 2.3.

It is important to notice that when the system is bounded or subject to the periodical boundary condition, the spectra of 2D dual cascades will be changed. It is pointed out in [18] the slope for low k cascade $-\alpha$ and the high k cascade $-\beta$ should satisfy the inequality: $\beta > 5$; $\alpha + \beta > 8$.

2.4.3 Quantum turbulence

The cascades in the quantum turbulence remains a hotly debated subject.

For 3D quantum turbulence, it is generally believed that there exist two distinguishable regimes: the classical regime and the quantum one. In the classical regime, the length scale is much larger than the inter-vortex distance $l_c \gg l_{vort}$. In this regime the quantum fluid resembles the classical inviscid fluid and the *Kolmogorov cascade* is expected. In the quantum regime, which is characterized by the scale $l_{vort} > l_q > \xi$, vortex lines could reconnect with nearest neighbors, deform into vortex rings, and twist into helix form to develop Kelvin waves [19]. It has been suggested in [19] that the transition from Kolmogorov cascade to Kelvin cascade is smooth, while in [20, 21] it is argued that an energy stagnation exists at the transition due to the unmatched energy flux constant in the two regimes.

For 2D quantum turbulence, the energy cascade is much simplified due to the point like structure of the vortex. The vortex could decay away either through elementary excitations or sound emission [22]. However, the quantum 2D turbulence lacks two important features enjoyed by its classical counterpart: incompressibility and the conservation of enstrophy. Since the vortices can be created from the fluid via instability, the enstrophy, if still defined as the integration of squared vorticty, is not a constant. Therefore, at the classical regime $l_c \gg l_{vort}$, it is unclear whether a dual cascade exists in 2D quantum turbulence.

To compare quantum turbulence with the classical turbulence quantitatively, it is necessary to decompose the kinetic energy $\int dx\, \rho\, |\mathbf{v}|^2$ into the incompressible and compress-

ible parts. To separate the two components, we adopt the approach mentioned in [10, 23], and consider the density weighted velocity $\mathbf{q} \equiv \sqrt{\rho}\mathbf{v}$. The kinetic energy density in Fourier space is $\varepsilon_{kin}(\mathbf{k}) = |\tilde{\mathbf{q}}(\mathbf{k})|^2$. The incompressible component is defined as $\mathbf{k} \cdot \tilde{\mathbf{q}}_{ic} = 0$, while the compressible part becomes $\tilde{\mathbf{q}}_c = \tilde{\mathbf{q}} - \tilde{\mathbf{q}}_{ic}$. The decomposition of kinetic energy takes the following form:

$$Compressible: \quad \tilde{\mathbf{q}}_c = \frac{\mathbf{k} \cdot \tilde{\mathbf{q}}}{k^2}\mathbf{k};$$

$$Incompressible: \quad \tilde{\mathbf{q}}_{ic} = \tilde{\mathbf{q}} - \frac{\mathbf{k} \cdot \tilde{\mathbf{q}}}{k^2}\mathbf{k};$$

$$E_{kin} = (2\pi)^2 \int d\mathbf{k}|\tilde{\mathbf{q}}|^2 = (2\pi)^2[\int d\mathbf{k}|\tilde{\mathbf{q}}_c|^2 + \int d\mathbf{k}|\tilde{\mathbf{q}}_{ic}|^2] = E_c + E_{ic}.$$

The energy spectra in d dimension could then be defined as:

$$\varepsilon_{c,ic} = k^{d-1} \int d\theta |\tilde{\mathbf{q}}_{c,ic}|^2.$$

With this definition, it has been stated in [23, 24] that a $k^{-5/3}$ power law for incompressible energy is observed. However, the interpretation for the spectrum is quite different. In [23], the power law is interpreted as the result of the direct cascade (enstrophy cascade), c.f. Fig 2.4. In [24], the $k^{-5/3}$ is interpreted as the inverse cascade (energy cascade) illustrated in the 2D classical case. It is also reported in [1] that a dual cascade is observed when the external potential (harmonic oscillator) is present (Fig 2.6).

In our numerical simulation, the incompressible spectra slope is around -3, and no $k^{-5/3}$ power law is observed. Without an artificial dissipation term to subdue the compressible energy, the incompressible energy induced by the rotation near vortices is quickly transferred to sound emission.
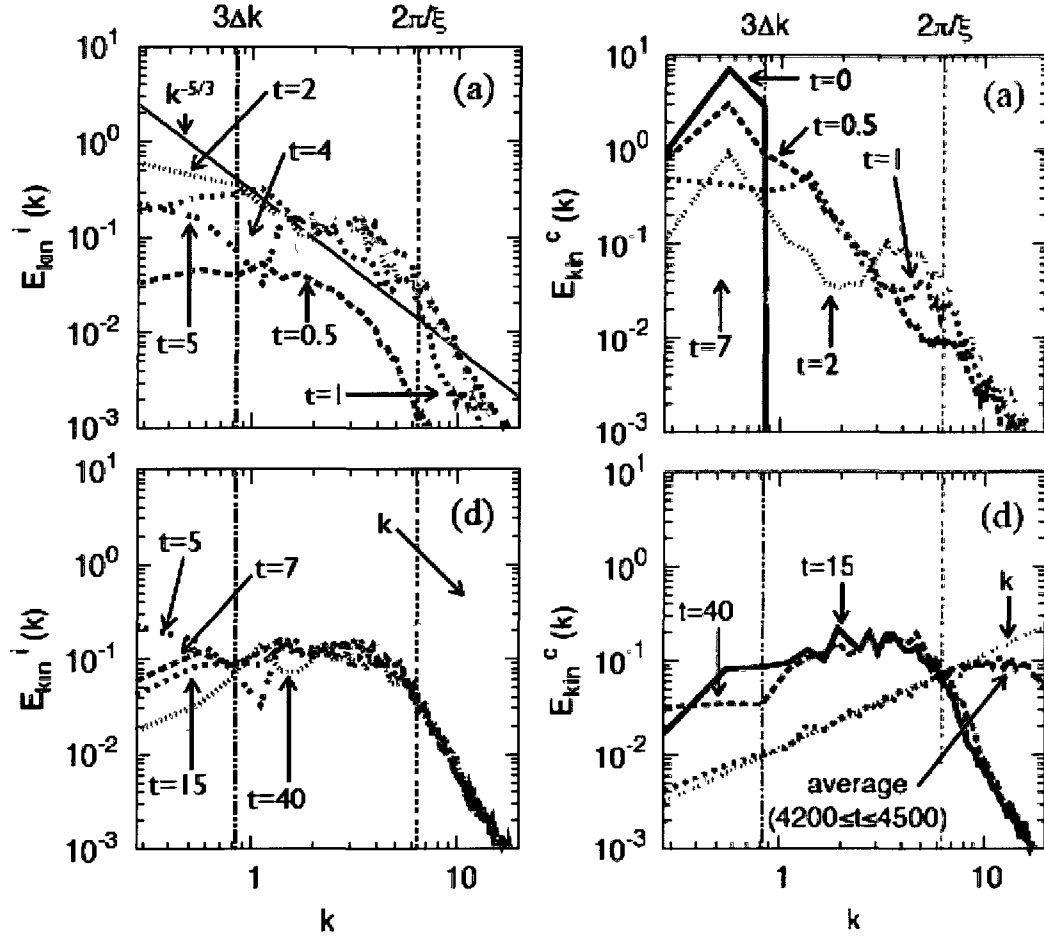
(a) Incompressible spectrum (Log-Log plot) (b) Compressible spectrum (Log-Log plot)

FIG. 2.4: Results from Tsubota group.

Credit: *Tsubota et al* [23]. (a): Incompressible energy spectrum at early stage of simulation ($t \leq 5$). (b): Compressible energy spectrum at early stage of simulation ($t \leq 7$). (c): Incompressible energy spectrum at late stage ($7 \leq t \leq 40$). (d) Compressible energy spectrum at late stage ($15 \leq t \leq 40$). The initial wave function $\psi = e^{i\theta(\mathbf{r},0)}$ has amplitude of 1. The phase is random in Fourier space: $\tilde{\theta}(\mathbf{k},0) = \theta_0 e^{i\alpha(\mathbf{k})}$ for $|\mathbf{k}| \in [\Delta k, 3\Delta k]$, and 0 otherwise, where $\Delta k = \frac{2\pi}{L}$ and $\alpha(\mathbf{k})$ is a random real number. The coherence length $\xi = 1$. To ensure continuity at the boundary, $\alpha(\mathbf{k}) = -\alpha(-\mathbf{k})$. The simulation was performed on 256^2 grid with 4th order Runge-Kutta method. The coupling constant $g = 1$. It is claimed in [23] that the direct energy cascade in 2D quantum turbulence is caused by the compressible energy and a Komolgorov $k^{-5/3}$ law is observed before the vortices decayed away (the upper left plot). However, this $k^{-5/3}$ is transient, which is quickly destroyed by the elementary excitations. This is confirmed by the fact that no $k^{-5/3}$ is observed in the lower left plot.

(a)   (b)
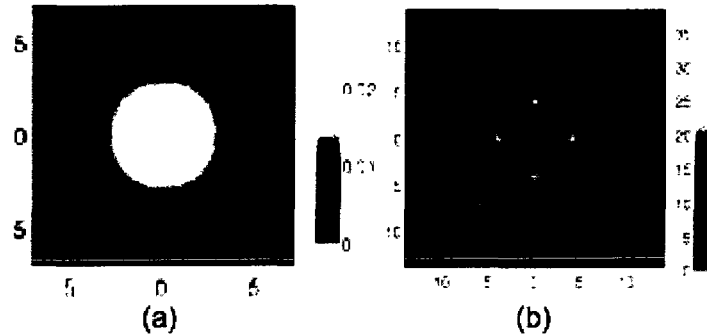
FIG. 2.5: Initial condition used by *Horng et al.* Excerpted from [ ].

The initial wave function consists of four vortices with winding number 1 embedded in a Gaussian back-ground. The external potential, a harmonic oscillator $V_{ext} = \frac{1}{2}(x^2 + y^2)$, is added to the GP equation. Fig (a): amplitude distribution; Fig (b): enstrophy distribution, the white dots indicates the position of the vortices. Adaptive Runge-Kutta method is used in the simulation.
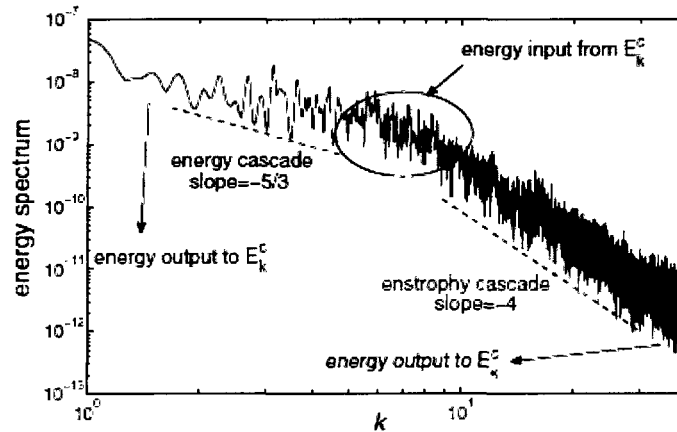
FIG. 2.6: Spectrum obtained in [ ].

Credit: *Horng et al.* The spectrum is obtained at $t = 100$, when the incompressible and compressible kinetic energy don't vary significantly. It is claimed in [ ] that the compressible energy functions as an energy injection source for the incompressible energy. Dual cascades are observed, with the inverse cascade following the $k^{-5/3}$ law and the direct cascade obeying k^{-4} power law.

2.5 Poincaré recurrence

The Poincaré recurrence theorem states that in an energy conserved system with bounded phase space, the system will return to a state arbitrarily close to its initial one after some time T_P. For a classical system, this statement seems to contradict the irreversibility dictated by the second law of thermodynamics. A typical argument to resolve this paradox is to claim that $T_P \rightarrow \infty$. However, for some systems, the Poincaré recurrence time can be very short. Among 2D mappings, Arnold's cat is one prominent example to demonstrate a short Poincaré recurrence time.

Defined on a unit square, Arnold's cat mapping reads:

$$\Gamma : (x, y) \rightarrow Mod[(2x + y, x + y), 1].$$

This mapping preserves the area, and is chaotic, ergodic, and reversible. To visualize it, one could discretize an image into $N \times N$ fragments, each of them is tagged by its position (i, j), $i \in [1, N]$, $j \in [1, N]$. Arnold's cat mapping is equivalent to relocating the image fragment (i, j) to (i', j'):

$$\Gamma : (i', j') \rightarrow Mod[(2i + j, i + j), N].$$

An example is given in Fig 2.8. The image size is 150×150 pixels. The Poincaré recurrence time is $T_P = 300$. A more interesting example of Arnold's cat mapping is shown in Fig 2.7 , in which case the picture is up side down at semi Poincaré period $T_P/2$. In our quantum lattice gas simulations, we encountered an unexpectedly short Poincaré recurrence when the averaged ratio of the internal energy to the kinetic energy is small. We also observed at semi-Poincaré period, vortices are depleted from the system. If the initial condition has vortices as input and is symmetric, a self-similar structure is observed at $1/4$ and $3/4$ Poincaré recurrence period. Detailed analysis can be found in 5.

(a) T=0   (b) T=28   (c) T=57

(d) T=85   (e) T=114
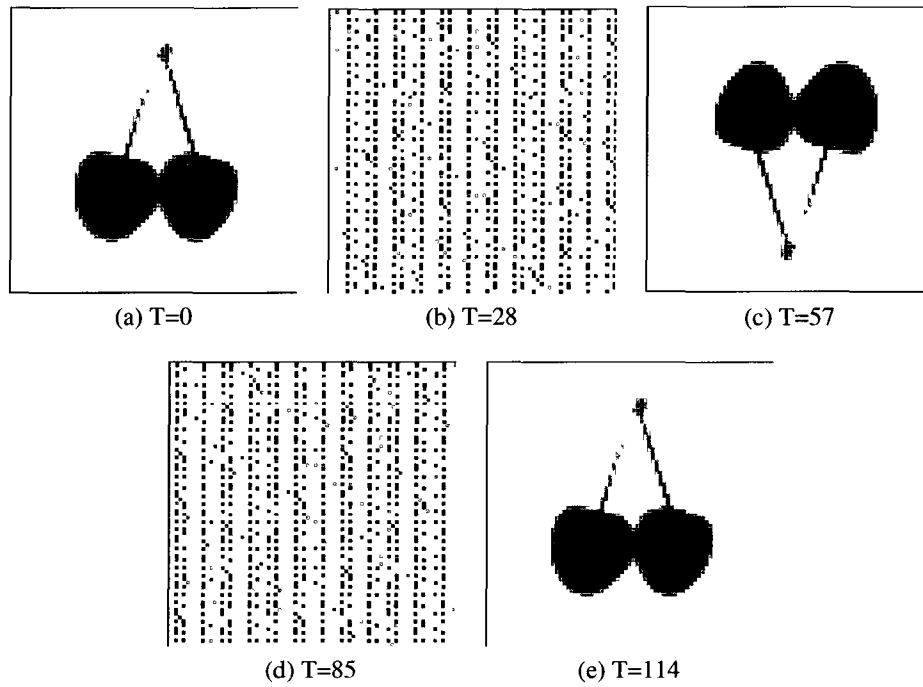
FIG. 2.7: Reversed image at $T = 57$ with Poincaré period being $T_p = 114$.

The image size is 74 pixels. Source: Wikipedia

(a) T=0   (b) T=75

(c) T=150   (d) T=225

(e) T=299   (f) T=300
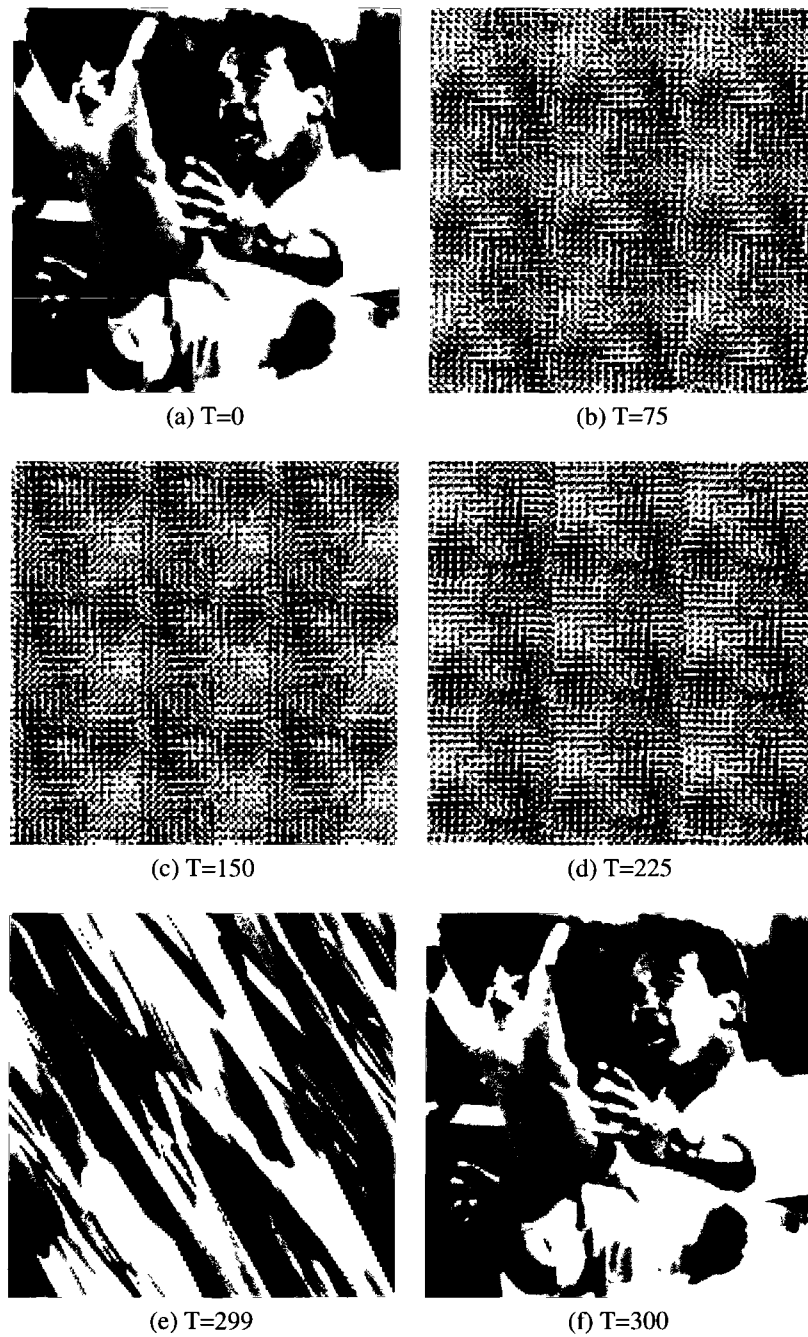
FIG. 2.8: Arnold's cat mapping.

Picture size 150×150 pixels. Poincaré recurrence time $T_p = 300$. Note that there is no semi-Poincaré period. Also, one should note that in the Arnold's cat map, the actual value of the Poincaré recurrence time has an nonlinear dependence on the number of pixels in the initial condition.

CHAPTER 3

Lattice Boltzmann Method

3.1 Overview

Lattice Boltzmann (LB) method was initially developed as an alternative for studying the behavior of classical turbulence. Using the Chapman-Enskog scale analysis, the LB algorithm reproduces Navier-Stokes equation up to the order of $\mathcal{O}(\varepsilon^2)$, where ε is the Knudsen number [25], defined to be the ratio of mean free path λ to the size of the system L: $\varepsilon = \lambda/L$. Later, it has been demonstrated by Succi that LB is naturally suitable for simulating the Dirac equation and therefore LB could simulate Schrodinger equation in the large wave-length limit [26]. In this research, a different approach is taken to apply LB onto nonlinear quantum system. Our approach treats the Nonlinear Schrodinger equation (NLS) as a diffusion equation with imaginary time. This treatment enable LB model to approach the NLS up to the order of $\mathcal{O}(\varepsilon^2)$, which is not dissimilar to the derivation of Navier-Stokes equation from LB. There exist two types of LB depending on the treatment of the time derivative in NLS, the explicit LB (exLB) scheme and the implicit-explicit LB (imLB) scheme. We have performed numerical simulations to demonstrate that the imLB

achieved better stability and higher accuracy. However, the root finding algorithm involved in imLB, such as Newton-Raphson method, renders it computationally expensive and vulnerable for scaling on a large cluster. In the end, this method will be replaced by a more stable and accurate method - Quantum Lattice Gas (QLG) model.

3.2 Description of the model

3.2.1 LB for Classical turbulence

Consider a classical system consisting of N interacting particles, each of which has mass m. When there is no external force, the evolution of distribution function $f(\mathbf{x}, \mathbf{p}, t)$ for one particle obeys the Boltzmann equation:

$$\frac{\partial}{\partial t} f + \frac{1}{m} \mathbf{p} \cdot \nabla f = -\Omega_{coll}, \tag{3.1}$$

Ω_{coll} standing for effect of particle collisions. Generally speaking, the collision operator Ω_{coll} could be very complicated, as it can include binary, trinary and even higher order collisional terms. A simplified collision operator - the the BGK operator - was proposed by Bhatnagar, Gross and Krook in 1954 [27]. BGK operator is given:

$$\Omega_{coll} = \frac{1}{\lambda}(f - f^{eq}), \tag{3.2}$$

where λ is the relaxation time and f^{eq} is the equilibrium distribution function. The BGK operator provides a simple picture for the evolution of a classical gas system : if the distribution function f is "further" away from its local equilibrium, the "faster" it evolves towards f^{eq}. Combining Eq 3.1 and Eq 3.2, one obtains the Boltzmann equation :

$$\frac{\partial}{\partial t} f + \frac{1}{m} \mathbf{p} \cdot \nabla f = -\frac{1}{\lambda}(f - f^{eq}). \tag{3.3}$$

Albeit the simple appearance of BGK operator, equation Eq 3.3 is algebraically nonlinear in macroscopic variables but linear in $\{f\}$. The detailed information about inter-particle collision is contained in the construction of equilibrium distribution function f^{eq} as well as the relaxation time λ, which could be nonlinear functions of f.

Based upon how Eq 3.3 is integrated, one can obtain two different version of Boltzmann equation, an explicit Boltzmann scheme and an implicit-explicit Boltzmann scheme. Integrating Eq 3.3 for a small time interval δt, one obtains:

$$f(\mathbf{x} + \delta\mathbf{x}, t + \delta t, \mathbf{p}) = f(\mathbf{x}, t, \mathbf{p}) - \frac{1}{\lambda \delta t} \int_t^{t+\delta t} d\tau \, [f(\mathbf{x}, \tau, \mathbf{p}) - f^{eq}(\mathbf{x}, \tau, \mathbf{p})], \qquad (3.4)$$

where $\delta\mathbf{x} = \mathbf{p}\,\delta t$ and for simplicity, λ is assumed to be a constant, independent of time. If Euler's forward method is used to evaluate the integration on the RHS of Eq 3.4, explicit Boltzmann equation (exBE) is obtained:

$$f(\mathbf{x} + \delta\mathbf{x}, t + \delta t, \mathbf{p}) = f(\mathbf{x}, t, \mathbf{p}) - \frac{1}{\lambda} [f(\mathbf{x}, t, \mathbf{p}) - f^{eq}(\mathbf{x}, t, \mathbf{p})]. \qquad (3.5)$$

A more accurate assessment of the integration on RHS of Eq 3.4 is to combine Euler's forward and backward method, which leads to impicit-explicit Boltzmann equation (imBE) :

$$f(\mathbf{x} + \delta\mathbf{x}, t + \delta t, \mathbf{p}) = f(\mathbf{x}, t, \mathbf{p}) - \frac{1 - \theta}{\lambda} [f(\mathbf{x}, t, \mathbf{p}) - f^{eq}(\mathbf{x}, t, \mathbf{p})]$$
$$- \frac{\theta}{\lambda} [f(\mathbf{x}, t + \delta t, \mathbf{p}) - f^{eq}(\mathbf{x}, t + \delta t, \mathbf{p})], \qquad (3.6)$$

where θ is a tunable parameter to weight the explicit and implicit components. Later it can be shown that the imBE formula is more stable and accurate than the exBE, however, it makes the computation more expensive.

To transform the continuous Boltzmann equation into a computation-friendly LB , a lattice is introduced on which the bits $\{f_i\}$ populate. One performs coarse-graining of the

distribution function f and its equilibrium form f^{eq} in the momentum space:

$$f(\mathbf{x}, t, \mathbf{p}) \rightarrow f(\mathbf{x}, t, \mathbf{p}_j) \equiv f_j(\mathbf{x}, t);$$

$$f^{eq}(\mathbf{x}, t, \mathbf{p}) \rightarrow f^{eq}(\mathbf{x}, t, \mathbf{p}_j) \equiv f_j^{eq}(\mathbf{x}, t).$$

After this discretization process, one achieves the explicit LB equation from Eq 3.5:

$$f_j(\mathbf{x} + \delta x, t + \delta t) = f_j(\mathbf{x}, t) - \frac{1}{\lambda}[f_j(\mathbf{x}, t) - f_j^{eq}(\mathbf{x}, t)]. \tag{3.7}$$

The implicit LB equation could also be obtained through the same manner:

$$f_j(\mathbf{x} + \delta \mathbf{x}, t + \delta t) = f_j(\mathbf{x}, t) - \frac{1 - \theta}{\lambda}[f_j(\mathbf{x}, t) - f_j^{eq}(\mathbf{x}, t)]$$
$$- \frac{\theta}{\lambda}[f_j(\mathbf{x}, t + \delta t) - f_j^{eq}(\mathbf{x}, t + \delta t)], \tag{3.8}$$

Based on different discretization of the momentum, LB model could be categorized into different topologies: the LB modes. For example, among one dimensional LB modes, the one-dimensional three-bit model, D1Q3, consists of three elements - the three bits: f_0, f_{+c}, f_{-c}, where c is a constant momentum. Fig 3.1 shows some frequently used modes.

(a) D1Q3   (b) D2Q9   (c) D3Q15
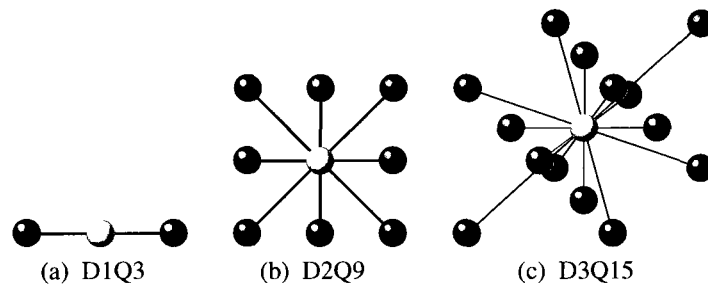
FIG. 3.1: Examples for different LB modes.

Different color stands for different velocity. For example, in two-dimensional nine-bit model, D2Q9, white stands for stationary bit, green dots stands for bits with velocity c, red dots stands for bits with velocity $\sqrt{2}c$, where c is a constant.

These bits could be viewed as the integration of distribution function in different domain of the momentum, e.g.

$$f_0 = \int_{-c}^{+c} f(\mathbf{v})d\mathbf{v}$$

$$f_{+c} = \int_{+c}^{+\infty} f(\mathbf{v})d\mathbf{v}$$

$$f_{-c} = \int_{-\infty}^{-c} f(\mathbf{v})d\mathbf{v}.$$

In classical turbulence simulation, the following two steps are crucial:

- a proper multi-scale analysis

- a set of correctly discretized $\{f_j^{eq}\}$

To recover Navier-Stokes equation, a Chapman-Enskog scale analysis is used. The Chapman-Enskog scale analysis is based on the fact that in a classical fluid, the dynamics of different scales coexist. For example, while the flow carries particles through advection process, the particles could also diffuse towards the regions with less density. Generally speaking, the advection process will take much shorter time to complete than the diffusion process. The dimensionless Knudsen number ε is used to gauge the dynamics that happen at various scales. ε could be chosen as the ratio of a mesoscopic quantity, which describes inter-particle action and a macroscopic quantity which characterizes the whole system. For example, $\varepsilon = \frac{\delta L}{L}$, where δL is the mean free path of particle and L is the physical length of the system. The Chapman-Enskog analysis can be expressed as the serial expansion of operators and physical quantities at different scales:

$$\nabla \to \varepsilon \nabla \tag{3.9a}$$

$$\partial_t \to \varepsilon \partial_{t_1} + \varepsilon^2 \partial_{t_2} + \mathcal{O}(\varepsilon^3) \tag{3.9b}$$

$$f \to f^{(0)} + \varepsilon f^{(1)} + \varepsilon^2 f^{(2)} + \mathcal{O}(\varepsilon^3) \tag{3.9c}$$

It could be seen that from the construction of LB equation Eq 3.7, most information about the dynamics of the system is concentrated onto the equilibrium state $\{f_j^{eq}\}$. A correctly designed equilibrium should reflect the symmetry of the system, obey Galilean invariance, and conserve any constants of motion. It turns out that the form of the equilibrium $\{f_j^{eq}\}$ depends highly on the topology of the LB modes. For each LB mode, there will be a set of unique weights to be attached to the bits $\{f_j^{eq}\}$.

A detailed derivation from LB equation to Naiver-Stokes equation can be found in [28]. It should be noted that all the f_js in LB has solid physics basis: the discretized distribution function can not be a negative number. A negative value of f_j during the numerical simulation could cause an explosive instability. Luckily, for the classical case, the second law of thermodynamics impose a strong restraint on the evolution of the distribution functions $\{f_j\}$:

$$\delta S = \sum_i w_i f_i \ln(f_i)|_{t+\delta t} - \sum_i w_i f_i \ln(f_i)|_t < 0,$$

according to which an Entropic Lattice Boltzmann (ELB) model [29] could be designed to overcome the numerical instability of LB. It has been reported that ELB successfully enhances the stability of LB at large Reynold number [30].

3.2.2 LB for Nonlinear Quantum system

In a classical system, one demands that the summation of f_j equals the distribution function. In order to achieve NLS through LB, the similar requirement is applied :

$$\sum_j f_j(\mathbf{x}, t) \equiv \psi(\mathbf{x}, t),$$

where $\psi(\mathbf{x}, t)$ is the wave-function.

In quantum case, the $\{f_j\}$ is complex valued and lacks a direct physics interpretation. Therefore, the restraints on the form of $\{f_j\}$ are very few and the construction of $\{f_j^{eq}\}$ becomes much simplified. The LB model used for simulating NLS can be viewed as a numerical method based on finite difference. Since the NLS could be viewed as a diffusion equation with imaginary time, it is necessary that a diffusion ordering be applied to LB:

$$\nabla \to \varepsilon\nabla \tag{3.10a}$$

$$\partial_t \to \varepsilon^2\partial_t \tag{3.10b}$$

$$f \to f^{(0)} + \varepsilon f^{(1)} + \varepsilon^2 f^{(2)} + \mathcal{O}(\varepsilon^3) \tag{3.10c}$$

Applying Eq 3.10 to the explicit LB Eq 3.7 and performing Tylor seriers expansions, the equations for the first three orders are:

$$\varepsilon^0 : \quad f_j^{(0)} = f_j^{eq} \tag{3.11a}$$

$$\varepsilon^1 : \quad \mathbf{c_j} \cdot \nabla f_j^{(0)} = -\frac{f_j^{(1)}}{\lambda} \tag{3.11b}$$

$$\varepsilon^2 : \quad \partial_t f_j^0 - \frac{1}{2}(2\lambda - 1)\delta t \sum_{\alpha\beta} c_{j\alpha}c_{j\beta}\partial_{x_\alpha}\partial_{x_\beta}f_j^{(0)} = -\frac{f_j^{(2)}}{\lambda\delta t}, \tag{3.11c}$$

where $\mathbf{c_j}$ stands for the velocity of the bit f_j. We sum over all the discretized f_j on both sides of Eq 3.11, and impose the constraints:

$$\sum_j f_j^{(0)} = \sum_j f_j^{eq} \equiv \psi \tag{3.12a}$$

$$\sum_j \mathbf{c_j} f_j^{(0)} \equiv \mathbf{q} \equiv 0 \tag{3.12b}$$

$$\sum_j c_{j\alpha}c_{j\beta}f_j^{(0)} \equiv c_s^2\delta_{\alpha\beta}\psi, \tag{3.12c}$$

where c_s^2 is a positive real number and $\delta_{\alpha,\beta}$ is the Kronecker delta. With these constraints, one can see that LB resembles the Schordinger equation for a free particle :

$$\partial_t\psi - \frac{1}{2}(2\lambda - 1)c_s^2\delta t\nabla^2\psi = 0. \tag{3.13}$$

By setting the relaxation time $\lambda \equiv \frac{1}{2} + \frac{i}{c_s^2 \delta t}$, one could obtain the free partial's Schordinger equation up to the accuracy of $\mathcal{O}(\varepsilon^4)$. If one appends the nonlinear potential term

$$\mathcal{N} = i\delta t\, g \left| \sum_j f_j^{(eq)} \right|^2 f_j^{(0)}$$

to the RHS of Eq 3.7, and repeats the procedure described above, the NLS is obtained:

$$i\partial_t \psi = -\nabla^2 \psi + g\, |\psi|^2\, \psi \tag{3.14}$$

The derivation of NLS from implicit LB is exactly the same as the explicit LB case provided that the relaxation time λ is replaced by the modified relaxation time $\lambda^* = \lambda - \theta$.

In the general case there are typically more bits in the set of $\{f_j\}$ than the available constraints provided by Eq 3.12, which enables greater freedom for the choice of f_j s than the classical case. In our research, we adopt Zhong's approach [31]:

Assuming that N bits in the set $\{f_j\}$ have the same speed c_n, the equilibrium $\{f_j^{eq}\}$ can be constructed as followings (with $0 < \alpha < 1$):

$$f_0^{eq} = (1 - \alpha)\psi$$

$$f_{c_n}^{eq} = \frac{\alpha}{n}\psi.$$

The explicit LB mainly contains two steps:

- collision: this is done through the BGK operator

- streaming: the local information at $(\mathbf{x}, t)$ is streamed into the next lattice site $(\mathbf{x}+\delta\mathbf{x}, t+ \delta t)$.

The streaming step is computationally inexpensive, which could be done easily through shift of memories. As for the collision step, all the computation are localized. These two features of LB make it an efficient method for large scale computation, e.g. calculation

involving $\mathcal{O}(10^5)$ processors. For imLB, the potential is chosen to be equal mix between the implicit part and the explicit one:

$$\mathcal{N} = i\delta t\theta|\sum_{\jmath} f_{\jmath}^{eq}(t + \delta t)|^2 f_{\jmath}(t + \delta t) + i\delta t(1 - \theta)|\sum_{\jmath} f_{\jmath}^{eq}(t)|^2 f_{\jmath}(t).$$

Appending the above equation to Eq 3.8, the equation relating $f_{\jmath}(t + \delta t)$ then becomes (for simplicity, δt is set to be 1 here):

$$f_{\jmath}^{eq}(t + 1) = \alpha_{\jmath}\sum_{\jmath} f_{\jmath}(t + 1); \alpha_0 = 1 - \alpha, \alpha_{\jmath} = \alpha/n(j \neq 0).$$

$$f_{\jmath}(t + 1) + \frac{\theta}{\lambda}(f_{\jmath}(t + 1) - f_{\jmath}^{eq}(t + 1)) + i\,\theta f_{\jmath}(t + 1)\left|\sum_{\jmath} f_{\jmath}^{eq}(t + 1)\right|^2 = g_{\jmath}(t). \quad (3.16)$$

$g_{\jmath}(t)$ is a complex number obtained through collision and streaming steps at t . The non-linear equations Eq 3.16 to be solved amounts to one quintic equation. To solve it , the Newton-Raphson method is employed. The NR method starts with a trial point x_0 and approximates the exact solution via the iteration routine:

$$x_{n+1} = x_n - \frac{f(x_n)}{f'(x_n)},$$

where $f'(x)$ is the derivative at x. To determine the solution, one can use the criteria:

$$\text{Convergence:} |x_{n+1} - x_n| < \eta,$$

with η being a small number.

Fig 3.2 illustrates the algorithms for exBE and imBE. The initial condition set to be $f_{\jmath}^{eq} = f_{\jmath}$. The potential term in LB will perturb the system and drive it away from initial equilibrium. It is important to note that for all the derivations mentioned above, we avoided the discussion about boundary conditions. In classical fluid simulation, the zeroth moment $\sum_{\jmath} f_{\jmath}$ is the density of the system and its first moment $\sum_{\jmath} c_j f_{\jmath}$ is the
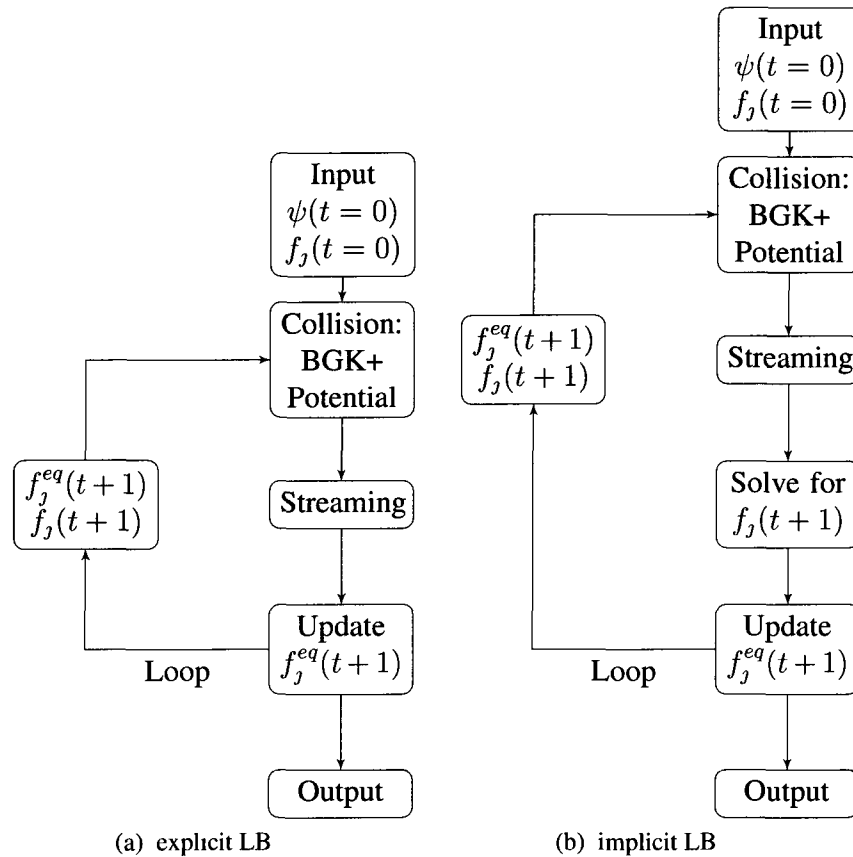
FIG. 3.2: Flowcharts for imBE and exBE.

momentum. At the boundary, one could require that the density goes to certain constant and velocity at the boundary vanishes. However, in the quantum case, the probability current $\mathbf{j} = i(\psi \nabla \psi^* - \psi^* \nabla \psi)$ has no direct correspondence in f_js. This introduces an extra difficulty when one applies LB to a bounded system. For simplicity, we constrain ourselves to periodical boundary condition in our simulations.

3.3   Numerical Tests

3.3.1   One Dimensional Soliton-Soliton Collision

There are few nonlinear systems which have analytical solutions. Among these few soluble systems, the one dimensional nonlinear Schrodinger equation:

$$i\partial_t \psi + \partial_{xx} \psi + g|\psi|^2 \psi = 0 \qquad (3.17)$$

provides the easiest test for the LB model. If the coupling constant $g > 0$, the particles in the system attract each other and hence a stable bright soliton solution could be found. If $g < 0$, the system becomes repulsive and a dark soliton solution exists. In this test, our focus is on the attractive nonlinear system with g=1:

$$i\partial_t \psi + \partial_{xx} \psi + |\psi|^2 \psi = 0. \qquad (3.18)$$

The analytical solution to equation Eq 3.18 represents a propagating soliton:

$$\mathcal{S}(a,b) = a\sqrt{2} \, sech[a(x - b\,t)]\, e^{i\,[\frac{bx}{2} - (\frac{b^2}{4} - a^2)\,t]}, \qquad (3.19)$$

where a is the amplitude of the soliton and b is the velocity. To better assess the robustness of LB method, we choose two solitons with different amplitude and opposite velocity as initial input. The two solitons are chosen to be non-overlapping wave functions:

$$\mathcal{S}_{t=0} = \mathcal{S}(a,b) + \mathcal{S}(a',-b).$$

The most notable features of the soliton-soliton collision are that:

- Soliton's shape remains unchanged after the collision,

- After each collision, each soliton will undergo a constant phase shift.

(a) Soliton-Soliton Collision

(b) Small Soliton Phase Shift

(c) Large Soliton Phase Shift
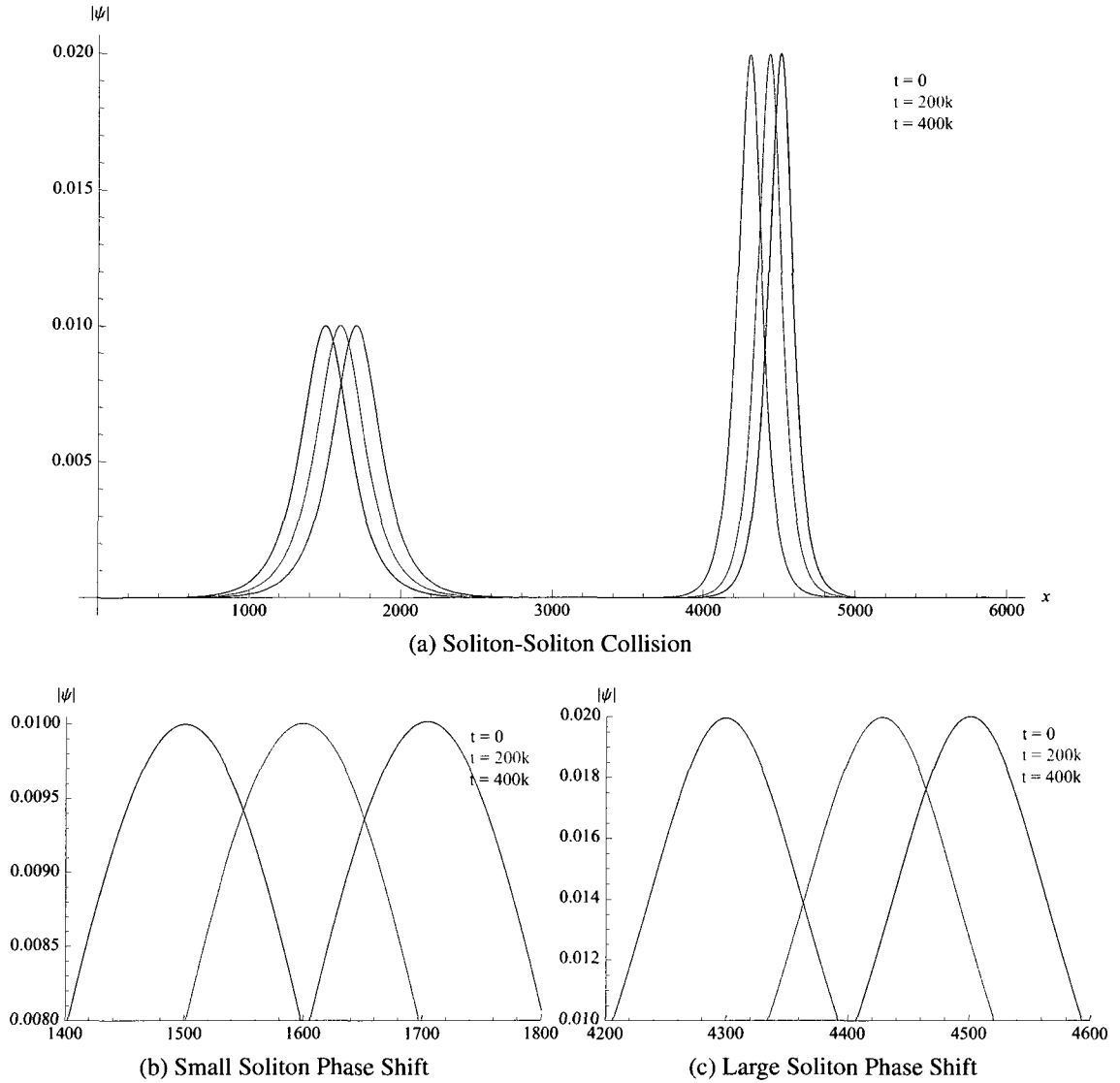
FIG. 3.3: Soliton-Soliton collision.

Space displacement $\delta x = 1$, time displacement $\delta t = 1$. The diffusion scaling will be reflected by the choice of amplitudes of the solitons. The parameters are $b = 0.03, a = 0.00707, a' = 0.01414, \theta = 0.48$, relaxation time $\lambda = 0.5 + 1.5i$. Each bit has the same weight: $\alpha_j = 0.333$. The number of collisions are 4 in this simulation.

We performed a test on a 6000 grid with imLB method. The LB mode D1Q3 was employed. The result for a 4×10^5 iteration run is demonstrated by Fig 3.3. From Fig 3.3, it could be observed that the shapes of solitons after 4 collision remains unchanged. The phase shifts after each collision can also be identified. For the small amplitude soliton, the phase shift is almost a constant: $\delta = 100$. However, for the large amplitude soliton there is an irregular phase shift: $\delta = 75$ for the first 2 collisions and $\delta = 125$ for the second 2 collisions. We think two factors probably contribute to this irregularity:

- The amplitude: if the amplitude is too large, the diffusion ordering is not valid and the LB scheme breaks down.

- Solution for the nonlinear equation: the Newton-Raphson iteration introduced larger errors if the amplitude of f_j is too large. This deviation could accumulate during the 400'000 iterations and get amplified at the boundaries where the two solitons collide.

To improve the LB's accuracy, the amplitudes of the solitons are lowered by half. The result, as shown in Fig 3.4, demonstrates improved performance for controlling the phase shifts. However, the amplitude for the larger amplitude soliton increases gradually.

In [31], only 1D soliton propagation was tested for the LB schemes. In our simulation, both soliton propagation and soliton-soliton collision are presented, which demonstrates that LB method can successfully reproduce the 1D NLS system.

3.3.2 Transverse Instability of 2D soliton train

Another interesting problem to study is the 2 dimensional modulation instability, which has been extensively reviewed in [32]. For a 2 dimensional NLS, there exists one eigen-solution $\psi_0(x, y, t)$ which describes a set of propagating solitons. When a transverse perturbation $\delta\psi \sim e^{ipy}$ is applied to the propagating soliton train, the soliton undergoes
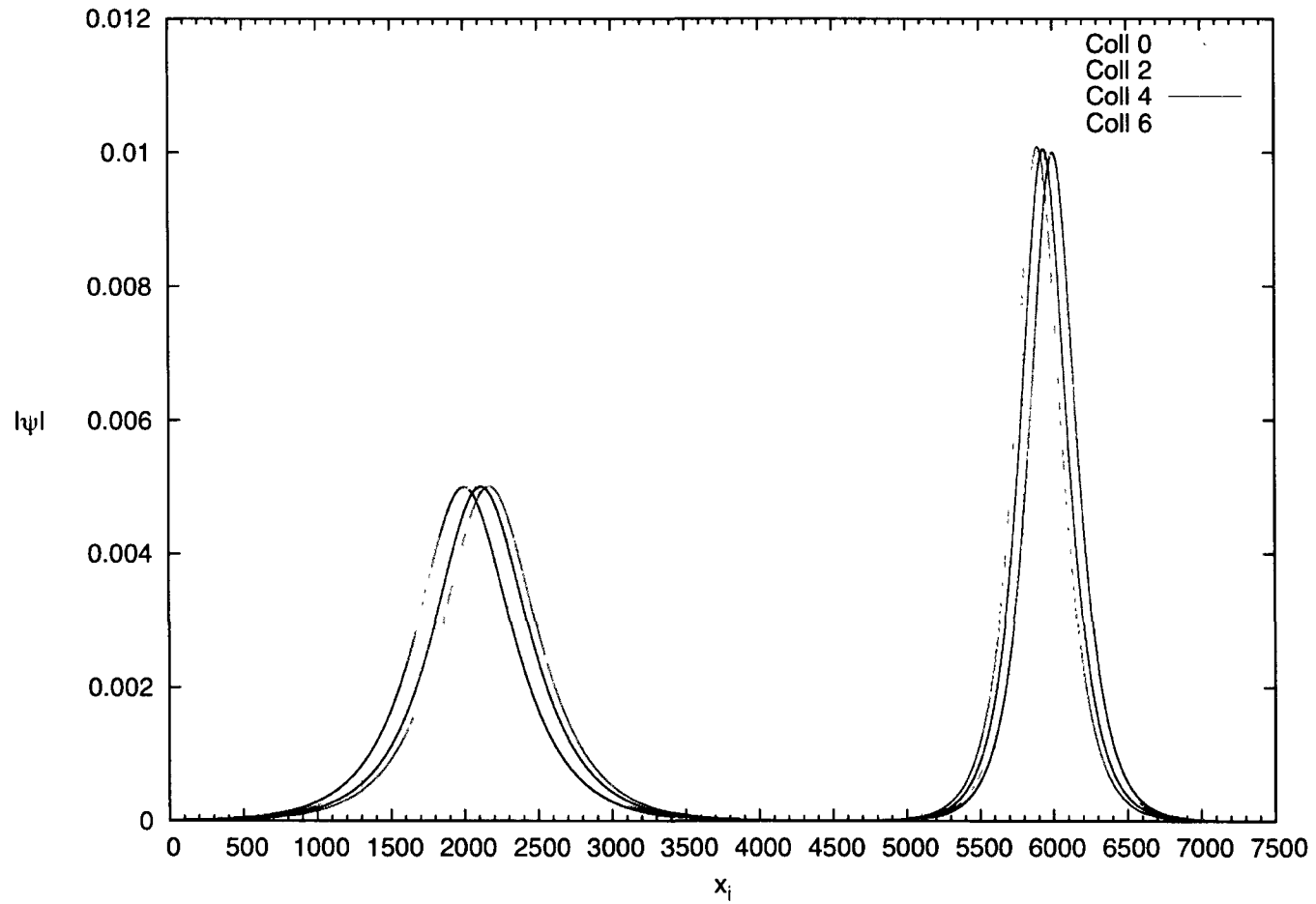
FIG. 3.4: Soliton-Soliton collision at small amplitude.

The parameters are: a=0.003536, a'=0.007071, b=0.03, $\theta = 0.48$.Relaxation time $\lambda = 0.5 + 1.5i$ The spatial dimension is 7500, iteration time is 7.5×10^5.

self-focusing along the transverse direction and become modulated. To understand this transverse modulation, linear stability analysis[33] is employed.

The 2 dimensional NLS reads:

$$i\partial_t\psi + \partial_{xx}\psi + \partial_{yy}\psi + |\psi|^2 = 0. \tag{3.20}$$

The soliton train solution of the equation above takes the form of:

$$\psi(x,y,t) = \sqrt{2}a\, Sech[a(x - bt)]e^{i(2bx-(4b^2-a^2)t)}.$$

To study the soliton train's stability in transverse direction, one could perform a Galilean transform such that in the new reference frame $\mathcal{R}_N$, the soliton train does not propagate. The advantage for this procedure is that it eliminate the need of parameter b. To obtain the evolution of the perturbed soliton in the lab frame, one only needs to perform an inverse Galilean transform. With this in mind, one performs the analysis of transverse instability in the frame $\mathcal{R}_N$ in which the eigen-solution of 2D NLSE reads:

$$\Psi_0(x,y,t) = \phi(x)e^{ia^2t} \equiv \sqrt{2}a\, Sech(ax)\, e^{ia^2t} \tag{3.21}$$

To assess the stability of the soliton train, a linear perturbation is applied to Eq 3.21 :

$$\delta\psi(x,y,t) \equiv \Psi(x,y,t) - \Psi_0(x,y,t) = [u_0(x,y) + iw_0(x,y)]e^{ia^2t+\Gamma t}, \tag{3.22}$$

where $u_0(x,y) = \eta u(x)e^{ipy}, w_0(x,y) = \eta w(x)e^{ipy}$ are the normal modes, p is the transverse wavenumber and $\eta \ll 1$. Inserting Eq 3.22 into Eq 3.20, the linearized equations are:

$$(\partial_{xx} - a^2 - p^2 + 3a^2 Sech[ax]^2)u[x] = \Gamma w[x]$$
$$(\partial_{xx} - a^2 - p^2 + a^2 Sech[ax]^2)w[x] = -\Gamma u[x]. \tag{3.23}$$

The exact eigen-solutions to Eq 3.23 are difficult to determine. However, at $p \sim 0$, there exists one asymptotic solution:

$$u[x] = 0$$

$$w[x] = \sqrt{2}a Sech[ax]$$

$$\Gamma = \sqrt{4a^2 p^2 - c_0 p^4}, \tag{3.24}$$

where $c_0 = \frac{4}{3}(1 + \frac{\pi^2}{3})$. If the transverse wavenumber $p \in [0, 2a/\sqrt{c_0}]$, Γ becomes a positive real number with the amplitude for the total wave-function $|\Psi| \propto \left|1 + \eta i e^{ipy} e^{\Gamma t}\right|$. As time increases, the amplitude increases exponentially and at $py = m\pi$ with m being an odd number, the soliton becomes highly modulated.

An implicit D2Q9 LB mode is used to simulate the 2D transverse instability. The transverse modulation can clearly be seen from Fig 3.5. The number of peaks corresponds to the transverse wave number p. In this simulation, $p = 7 \times 2\pi/L_y$, therefore 7 peaks are formed while the soliton train propagates along x-direction.

3.3.3 Conclusion

In this work, LB has been employed to simulate the 1D soliton-soliton collision and transverse instability of a 2D soliton train. LB has proven that it can successfully reveal some aspects of the physics of the 1D and 2D NLS system. For example, in the 1D soliton collision test, for 7.5×10^5 iteration, the soliton shape remains largely unchanged after the collision, and in 2D simulation, the soliton train is observed to become self-focusing based on LB's result. However, the LB methods suffer from the following inefficiencies:

- the implicit LB requires solving for a quintic equation, which compromises LB's scaling behavior;
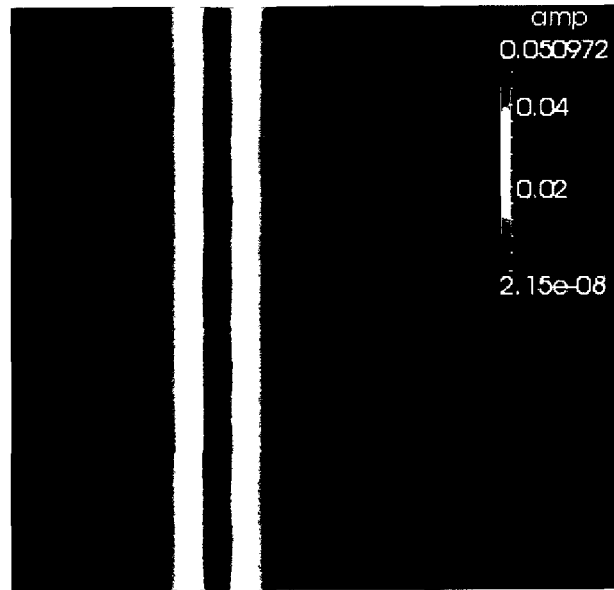
(a) t=0
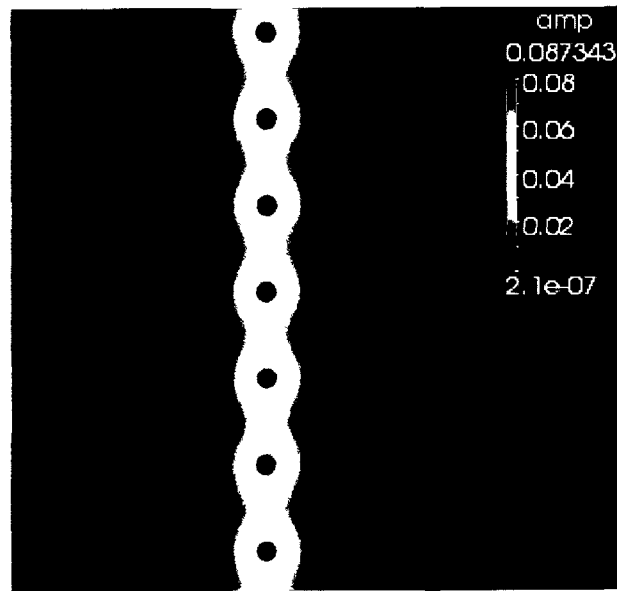
(b) t=2000

FIG. 3.5: Amplitude plots for Transverse Modulation.

The initial condition parameters are: $grid = 600^2, a = 0.05, b = 0.05, \theta = 0.5, \lambda = 0.5 + 1.5i, \eta = 0.02$. The initial wave-function is given a phase e^{i2bx}. The result is that the soliton train will propagate along x-direction and undergoes transverse modulation at the same time.

- during the simulation, it has been uncovered that LB is highly empirical - the conservation of the constant of motion highly depends on the choice for θ: the splitting factor between implicit and explicit parts in Eq 3.6;

- comparing with other highly accurate method, e.g. the pseudo-spectra method, LB's collide-streaming operation is neither unitary nor symplectic, therefore the conservation of density and total energy can not always be satisfied in the NLS system.

Due to these inefficiencies, we deemed the LB method not to be optimal for the study of quantum turbulence, which requires a highly scalable and accurate method to examine the vortex dynamics within a finite domain. The Quantum Lattice Gas (QLG) method happens to meet such requirement and it will replace LB to become the major tool to probe quantum turbulence in the following studies.

CHAPTER 4

Quantum Lattice Gas Algorithm

4.1 Description of the algorithm

Quantum Lattice Gas (QLG) algorithm is originally designed to optimize computation on the quantum computers [34, 35]. On quantum computers, the unit of information storage is a qubit. Unlike a classical bit, the value of which is either 0 or 1, the value of a qubit could be 0, 1, and any interpolation between them. An atom's spin wave function can be employed to realize the qubit:

$$|q\rangle = \alpha |0\rangle + \beta |1\rangle ,$$

with $|\alpha|^2 + |\beta|^2 = 1$. Another distinct feature of the qubit is the entanglement of multiple qubits. Two entangled qubits form the Bell states [36]:

$$|00\rangle = \frac{1}{\sqrt{2}}(|0\rangle \otimes |0\rangle + |1\rangle \otimes |1\rangle)$$

$$|11\rangle = \frac{1}{\sqrt{2}}(|0\rangle \otimes |0\rangle - |1\rangle \otimes |1\rangle)$$

$$|10\rangle = \frac{1}{\sqrt{2}}(|0\rangle \otimes |1\rangle + |1\rangle \otimes |0\rangle)$$

$$|01\rangle = \frac{1}{\sqrt{2}}(|0\rangle \otimes |1\rangle - |1\rangle \otimes |0\rangle).$$

on a Hilbert space of 2^2 dimensions.

QLG algorithm is constructed on a lattice populated by these Bell states. Applying a series of local unitary collision and unitary streaming operations at each lattice site, the QLG algorithm can model, in the long wavelength limit, the dynamics of the GP system. Since the streaming operator connects the neighboring qubits, in essence, the QLG algorithm belongs to the category of the finite difference method for calculating the Laplacian $-\nabla^2$. The time derivative is obtained by using Euler's explicit method.

To simulate the GP system, a square-root-of-swap ($\sqrt{SWAP}$) operator is used as the unitary collision operator. The $\sqrt{SWAP}$ operator reads:

$$\Lambda = \begin{pmatrix} 1 & 0 & 0 & 0 \\ 0 & \frac{1-i}{2} & \frac{1+i}{2} & 0 \\ 0 & \frac{1+i}{2} & \frac{1-i}{2} & 0 \\ 0 & 0 & 0 & 1 \end{pmatrix}$$

This $\sqrt{SWAP}$ operator could be reduced to a rank 2 matrix acting on a subspace spanned by the Bell states. The local unitary collision of the qubits becomes:

$$\begin{pmatrix} q_0 \\ q_1 \end{pmatrix} \rightarrow \begin{pmatrix} \frac{1-i}{2} & \frac{1+i}{2} \\ \frac{1+i}{2} & \frac{1-i}{2} \end{pmatrix} \begin{pmatrix} q_0 \\ q_1 \end{pmatrix}.$$

One can define the collision operator on the 2×2 subspace to be $\hat{\mathcal{C}} = \frac{1}{2}\begin{pmatrix} 1-i & 1+i \\ 1+i & 1-i \end{pmatrix}$. To encode the dynamics of quantum wave function into qubits, a set of streaming operators are required. The streaming operators used for simulating GPE are [36]:

$$\hat{\mathcal{S}}_{\Delta x_i, 0} = n + e^{\Delta x_i \partial_{x_i}} \bar{n}$$

$$\hat{\mathcal{S}}_{\Delta x_i, 1} = \bar{n} + e^{\Delta x_i \partial_{x_i}} n,$$

where $n = \frac{1}{2}(1 - \sigma_z)$, $\bar{n} = \frac{1}{2}(1 + \sigma_z)$, $\sigma_z = \begin{pmatrix} 1 & 0 \\ 0 & -1 \end{pmatrix}$. Δx_i is the distance shifted along $\mathbf{e}_i$ direction. The subscript α in $\hat{\mathcal{S}}_{i,\alpha}$ indicates which qubit is operated on. Interleaving the non-commuting collision and streaming operators, one can obtain the unitary evolution operator:

$$\hat{\mathcal{I}}_{x_i, \alpha} = \hat{\mathcal{S}}_{-\Delta x_i, \alpha} \hat{\mathcal{C}} \hat{\mathcal{S}}_{\Delta x_i, \alpha} \hat{\mathcal{C}}$$

$$\hat{\mathcal{U}}_\alpha = \hat{\mathcal{I}}_{x\alpha}^2 \hat{\mathcal{I}}_{y\alpha}^2 \tag{4.1}$$

One can define the wave function $\psi(\mathbf{x}, t) \equiv q_0(\mathbf{x}, t) + q_1(\mathbf{x}, t)$. Applying the evolution operator on a set of qubits and addition of the two qubits, one finds the following evolution equation [37]:

$$\psi(\mathbf{x}, t + \Delta t) = \psi(\mathbf{x}, t) + i\Delta x^2 \frac{1}{2} \nabla^2 \psi + (-1)^\alpha \mathcal{O}[\Delta x^3].$$

When the diffusion order is taken: $\Delta x^2 = \Delta t$, this equation recovers the Schrodinger equation for a free particle under $\Delta t \to 0$. Notice that the error at $\mathcal{O}[\Delta x^3]$ takes the opposite sign for the evolution operator affiliated with the different qubit, therefore the error could be reduced to $\mathcal{O}[\Delta x^4]$ if the evolution operator of both qubits are used: $\{q\} \to \hat{\mathcal{U}}_0 \hat{\mathcal{U}}_1 \{q\}$.

To incorporate the effect of potential, one needs to incorporate an additional unitary term to the evolution operator $\hat{\mathcal{U}}_\alpha$:

$$\Omega[V(\mathbf{x})] = e^{-i\Delta t V(\mathbf{x})}.$$

To approximate the GPE equation, one could project the initial wave function $\psi(\mathbf{x}, 0)$ onto the two qubits:

$$q_0(\mathbf{x}, 0) = \psi(\mathbf{x}, 0)\alpha_0 \, ; \, q_1(\mathbf{x}, 0) = \psi(\mathbf{x}, 0)\alpha_1,$$

$\alpha_0 + \alpha_1 = 1$, then apply the evolution operator on the qubits:

$$\begin{pmatrix} q_0(\mathbf{x}, t + \Delta t) \\ q_1(\mathbf{x}, t + \Delta t) \end{pmatrix} = \hat{\mathcal{U}}_0 \, \Omega[V(\mathbf{x}, t + \frac{\Delta t}{2})/2] \, \hat{\mathcal{U}}_1 \, \Omega[V(\mathbf{x}, t)/2] \begin{pmatrix} q_0(\mathbf{x}, t) \\ q_1(\mathbf{x}, t) \end{pmatrix}. \qquad (4.2)$$

Performing a Taylor expansion of the RHS of Eq 4.2 under diffusion scaling ($\Delta t = \Delta x^2$), one obtains:

$$\bar{q}(\mathbf{x}, t + \Delta t) = [\mathbb{1} + i\Delta t(\sigma_x \nabla^2 - V(\mathbf{x}, t))]\bar{q}(\mathbf{x}, t) + \mathcal{O}(\Delta t^2), \qquad (4.3)$$

where $\bar{q} = \left(\begin{smallmatrix} q_0 \\ q_1 \end{smallmatrix}\right)$ and $\sigma_x = \left(\begin{smallmatrix} 0 & 1 \\ 1 & 0 \end{smallmatrix}\right)$. By summing the two components of $\bar{q}$ in Eq 4.3 one arrives at:

$$\psi(\mathbf{x}, t + \Delta t) = [1 + i\Delta t(\nabla^2 - V(\mathbf{x}, t))]\psi(\mathbf{x}, t) + \mathcal{O}[\Delta t^2]. \qquad (4.4)$$

In the limit $\Delta t \to 0$, Eq 4.4 becomes the GPE with the potential $V(\mathbf{x})$ being substituted by $g|\psi|^2 + V$:

$$i\partial_t \psi = -\nabla^2 \psi + g|\psi|^2\psi + V\psi = \hat{\mathcal{H}}(t)\psi(t), \qquad (4.5)$$

where $\hat{\mathcal{H}}$ is the Hamiltonian.

Notice that in deriving the GPE from QLG, the symmetrized form of the potential $\Omega[V(\mathbf{x}, t)/2]$ is used. This is done in order to minimize the systematic error. To see how this work, one could start with the exact solution of Eq 4.5:

$$\psi(t) = \psi(t_0) - i \int_{t_0}^t \hat{\mathcal{H}}(t')\psi(t') \, dt', \qquad (4.6)$$

It is convenient to choose $t = t_0 + \Delta t$. Using trapezoidal rule to approximate the time integral and separate the explicit wave function from the implicit one, Eq 4.6 is rewritten

as:

$$[1 + i\frac{\Delta t}{2}\hat{\mathcal{H}}(t_0 + \Delta t)]\psi(t_0 + \Delta t) = [1 - i\frac{\Delta t}{2}\hat{\mathcal{H}}(t_0)]\psi(t_0). \tag{4.7}$$

Since the wave function is the summation of the qubits, it is reasonable to require that the qubits $\bar{q}$ also obey the equation with the same form of Eq 4.7. Upto $\mathcal{O}[\Delta t^2]$, the operator $[1 - i\frac{\Delta t}{2}\hat{\mathcal{H}}(t_0)]$ could be approximated with the unitary evolution operator $\hat{\mathcal{U}}_\alpha \, \Omega[V(t_0)/2]$. Notice that the operator on R.H.S of Eq 4.7 is the conjugate transpose of the one on L.H.S, when projected onto the qubits space, Eq 4.7 transforms into:

$$\Omega[V(t_0 + \Delta t)/2]\hat{\mathcal{U}}_\beta^\dagger \, \bar{q}(t_0 + \Delta t) = \hat{\mathcal{U}}_\alpha \, \Omega[V(t_0)/2] \, \bar{q}(t_0). \tag{4.8}$$

Apply on both sides the inverse operator of $\Omega\hat{\mathcal{U}}$, the qubits at $t_0 + \Delta t$ becomes

$$\bar{q}(t_0 + \Delta t) = \hat{\mathcal{U}}_\beta \, \Omega[V(t_0 + \Delta t)/2]\hat{\mathcal{U}}_\alpha \, \Omega[V(t_0)/2]. \tag{4.9}$$

Since the interleaved operator affiliated with the different qubit could reduce the error, the qubit indicator could be chosen: $\alpha = 1$ and $\beta = 0$. For a GP system, the troublesome part in the above equation is the implicit potential $V(t_0 + \Delta t)$ which is dependent on the probability density $|\psi|^2$. The standard method for obtaining the implicit potential is Newton-Raphson root finding algorithm. This is an expensive operation. To avoid this, the potential at $t_0 + \Delta t/2$ is used instead:

$$\bar{q}(t_0 + \frac{\Delta t}{2}) = \hat{\mathcal{U}}_1 \Omega V(t_0)/2;$$

$$V(t_0 + \Delta t) \cong V(t_0 + \frac{\Delta t}{2}) = \left|\sum_\gamma q_\gamma(t_0 + \Delta t/2)\right|^2.$$

With this substitution, one arrives at Eq 4.2.

From the derivation above, it could be observed that the symmetrized QLG algorithm resembles the Crank-Nicholson (C-N) method, using the Cayley form [38]:

$$\psi(t + \Delta t) = [1 - i\frac{\Delta t}{2}\hat{\mathcal{H}}]^{-1}[1 + i\frac{\Delta t}{2}\hat{\mathcal{H}}]\psi(t).$$

Therefore, it is expected that the QLG could achieve the same accuracy as C-N method, but has the strong advantage of being a unitary algorithm.

Since the derivation of GPE from QLG is dependent on the diffusion scaling, in numerical simulations, the temporal step $\Delta t = T/n_t$ and discretization of the domain $\Delta x = L/n_s$, both n_t and n_s being natural numbers, should satisfy $\Delta t = \Delta x^2 \equiv a$. Under this scaling, the GPE has the following expression:

$$i\partial_t \psi = -\nabla^2 \psi + a\,g|\psi|^2\psi + a\,V\psi. \tag{4.10}$$

The coherence length ξ, defined in Chap 2, is related with the temporal steps and coupling constants through the following relation:

$$\xi^2 = \frac{1}{\rho_0\,a\,g}.$$

The bulk density is defined as $\rho_0 = \dfrac{1}{L^2} \displaystyle\int_\Omega |\psi(t=0)|^2$, with Ω being the 2D area L^2 and $\psi(t=0)$ the initial wave function.

4.2   Conservation of the mean density

One great feature of the QLG algorithm is its unitarity: both evolution operator and potential term are unitary operation. To extract the wave function from the qubits, one needs to perform the addition which mounts to the operation $\bar{q} = \hat{A}q \equiv (1 + \sigma_x)q$. Up to the order $\mathcal{O}[\varepsilon^2]$, the unitary operator $\hat{\mathcal{U}}$ commutes with the addition $\hat{A}$. Therefore the probability and energy are conserved upto $\mathcal{O}[\Delta t^2]$ during the numerical simulation. The accuracy demonstrated by the QLG algorithm is comparable with other highly accurate methods, e.g. pseudo-spectra method [2].

Since QLG automatically conserves the norm of the qubits, the numerical loss in the

mean density is largely due to the overlapping of the two qubits:

$$\delta\bar{\rho} = \int d\mathbf{x}\left(|\psi|^2 - |\bar{q}|^2\right) = \int d\mathbf{x}\left(q_0^* q_1 + q_0 q_1^*\right).$$

When q_0 is kept purely imaginary and q_1 is purely real, or vice versa, the overlap between the two qubits vanishes and the conservation of density can be exactly enforced. To achieve this goal, two modification are made in the QLG algorithm:

- the initial profile of qubits is chosen so that $q_0 = Re[\psi]$, $q_1 = i\,Im[\psi]$;

- the potential operator Ω is substituted by the non-diagonal matrix:

$$\Omega_N = \begin{pmatrix} \cos[V\Delta t] & -i\,\sin[V\Delta t] \\ -i\,\sin[V\Delta t] & \cos[V\Delta t] \end{pmatrix},$$

such that $\sum_\gamma (\Omega_N \cdot \bar{q})_\gamma = e^{-iV\Delta t}\,\psi$.

Under the shifting operation, neither q_0 nor q_1 changes phase. After the collision operator is applied twice, the phases of q_0 and q_1 are swapped, e.g. q_0 is changed to be imaginary and q_1 to be real. The QLG contains an even number of collision operator, therefore one of the qubits is purely real and the other one imaginary. It is easy to check that the new potential operator Ω_N keeps the relative phase to be $\pi/2$ for the 2 qubits. With the phase of each qubit remaining unchanged, the overlap between q_0 and q_1 vanishes and the mean density conservation is guaranteed unconditionally.

4.3   Validation of QLG

It is well known that when the interaction between atoms is attractive, the GP equation

$$i\partial_t\psi + \frac{\partial^2}{\partial x^2}\psi + |\psi|^2\psi = 0$$

admits soliton solution. A bright soliton solution takes the form of :

$$S = \sqrt{2}\,a\,exp\left[i\{b\,x/\sqrt{2} - (b^2/4 - a^2)t\}\right]\,sech\left[a(x\sqrt{2} - b\,t)\right],$$

where a gauges the amplitude and b controls the speed of the soliton. The one dimensional soliton-soliton collision has two notable features:

- The shape of each soliton remains unchanged after collision;

- A constant phase shift (displacement of the peak of soliton) occurs for each soliton involved in the collision process.

To validate the QLG algorithm, a soliton-soliton collision simulation was performed by Vahala et.al. [2]. In the simulation, two solitons with different amplitudes are well separated such that their overlap is small. The total initial wave function takes the form:

$$\psi_0 = a\sqrt{2}\,e^{ib\,x/2}\,sech[a(x - x_0)] + a_1\sqrt{2}\,e^{ib_1\,x/2}\,sech[a_1(x - x_1)],$$

with $a_1 = 2a$ and $b = -b_1$. The simulation is carried on a lattice with its size being 6000. The amplitude and the phase shift after collision are displayed in 4.1 and 4.2 respectively. It can be seen that the solitons' shape remain unchanged after collision and the phase shift of each soliton remains a constant. Therefore, it is persuasive that QLG can be used to simulate a quantum system accurately.

4.4 Scalability

To probe the dynamics of quantum turbulence at small scales, a large lattice is required for spatial resolution. An optimized parallel algorithm is demanded to conduct the simulation efficiently. The QLG algorithm inherits remarkable scaling behavior due to the fact that most of the algorithm is conducted locally. The weak scaling and strong scaling behavior for the 3D QLG algorithm are demonstrated respectively in Table 4.1 and
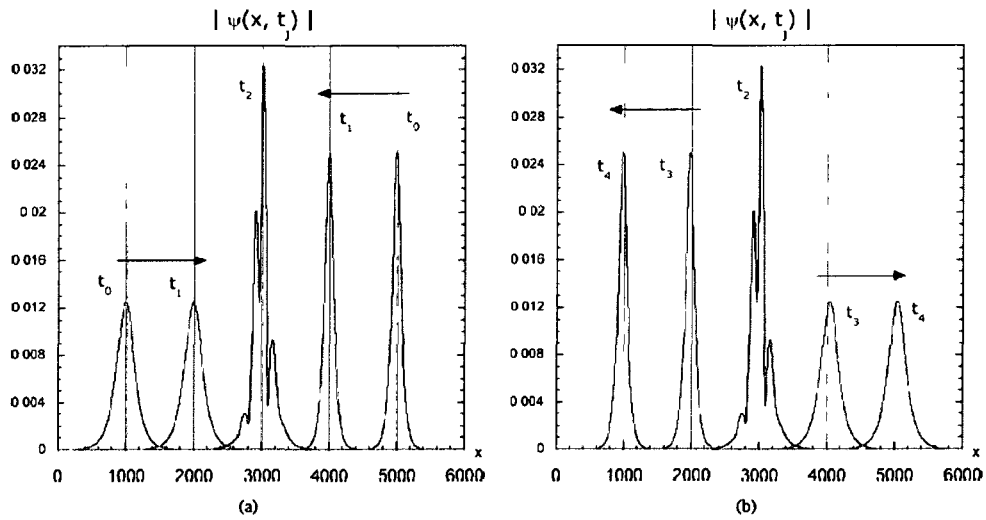
FIG. 4.1: 1D soliton-soliton collision under QLG. Credit: Vahala et. al. [2] The initial soliton are depicted by the green line in Fig (a). Time interval $\delta t = 30'000$. Each time interval contains one soliton-soliton collision. From Fig(b), it can be seen that after 4 collisions, the solitons' shape remain unchanged.
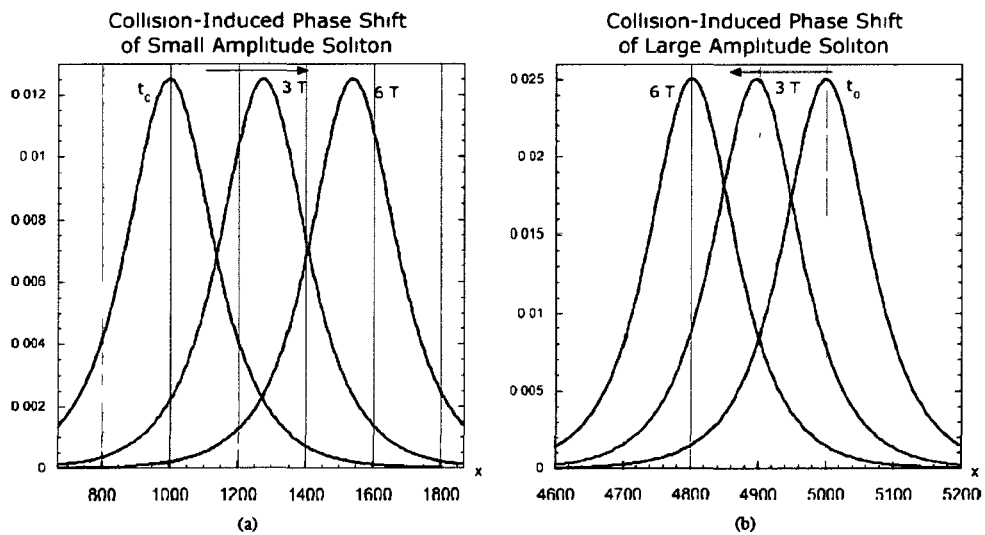
FIG. 4.2: Phase shift in
1D soliton-soliton collision under QLG. Credit: Vahala et.al.[2] The 1 soliton period $T = 180'000$. Fig(a): phase shift for small amplitude soliton. Fig(b): phase shift for large amplitude soliton. One period contains 2 soliton collision. It can be seen that the phase shift of both soliton remain a constant after 12 collisions.

Fig 4.3. Both scaling tests are done on the IBM Blue G/P "Intrepid" at Argonne National Laboratory.

4.5 Remarks

Boundary conditions play an important role in the evolution of a turbulent system. When a bounded system is studied with the LB model, the boundary conditions are enforced by switching to momentum space from the bits [28]. Consider the D2Q9 model for instance, a 9×9 matrix could transform the 9 bits $\{f_i\}$ into physical tensors such as density ρ and current j, and the higher macroscopic moments. The physical tensors transform as demanded by the physical boundary conditions, such as bounced-back boundary condition in which the momentum is reflected. Subsequently, the transformed physical quantities could be mapped back to the bits.

This could be accomplished through LB because the bits $\{f_i\}$ have clear connection with the momentum. However, in QLG, there is no direct connection between the probability current and the qubits. Therefore in the following QLG numerical simulations, one restricts the boundary condition to be periodic.

Another interesting problem to study is the effect of rotation on a dilute BEC gas. However, the implementation of rotating frame is not trivial for QLG. To approximate the GPE, QLG method uses a series of local unitary collision and streaming operators, which are homogeneous on all lattice sites. To simulate the rotating frame, one probably needs inhomogeneous streaming operations, e.g. the qubits far away from rotating axis will be streamed further than those close to the axes, which could impose a significant increase in computing expense. In this quantum turbulence study, one only applies QLG to a non-rotating system.

GRID	#CORES	WALL CLOCK	IDEAL	GFLOPS	%PEAK
400^3	64	368.1	368.1	33.5	15.4
800^3	512	371.6	368.1	265.8	15.3
1600^3	4096	372.2	368.1	2122.7	15.2
3200^3	32768	375.5	368.1	16850.3	15.1

TABLE 4.1: Weak Scaling of QLG.

In the ideal case, the computing time should remain a constant when the number of computing nodes increases at the same rate as the amount of tasks. For example, when the grid doubles in 3D simulation, the number of cores needs to be increased by 2^3 to maintain the computing time to be a constant. As shown in the wall-clock column, the QLG's weak scaling is almost close to the ideal case.
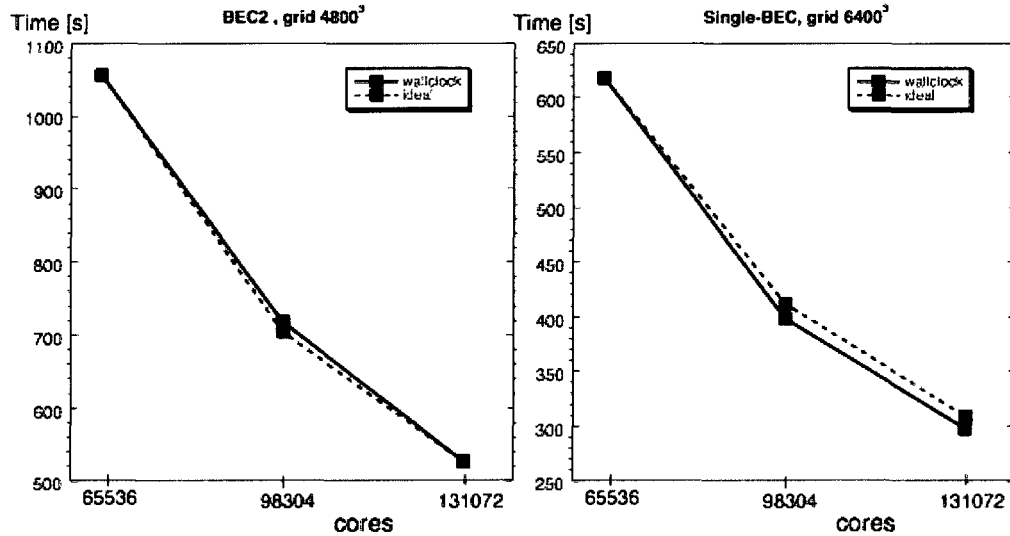
FIG. 4.3: Strong Scaling of QLG.

For an ideally parallelized algorithm, the computing time should be halved when the number of cores doubles while the amount of tasks remain unchanged. As demonstrated in the plots above, QLG's strong scaling is very close to the ideal case up to 131'072 cores. Indeed we find superlinear scaling for large grids (6400^3).

CHAPTER 5

Weak internal energy regime

If the internal interaction in a GP system is smaller or comparable with the kinetic energy ($g \lesssim \mathcal{O}[1]$), the diffusion ordering is appropriate to reflect the dynamics, and the QLG algorithm is valid for treating the potential perturbatively. To probe the dynamics of the quantum fluid, it is important to track the vortices. In the 2D case, it is convenient to use phase distribution to pinpoint the location of the vortices appearing at the end of the branch cut. Alternatively, the distribution of the density weighted vorticity could also reveal the distribution of the vortices [1]. The density weighted vorticity is defined as $\omega_q = (\nabla \times \sqrt{\rho}\mathbf{v}) \cdot \mathbf{e}_z$, where $\mathbf{e}_z$ is the unit vector along $\hat{z}$ axis. The two components of ω_q are:

- $A = \nabla\sqrt{\rho} \times \mathbf{v}$, which reflects the variation of density near the vortex core;

- $B = \sqrt{\rho}\nabla \times \mathbf{v}$, which could pinpoint the location of the vortex since $\nabla \times \mathbf{v} = \Gamma\delta(\mathbf{x} - \mathbf{x}_0)\mathbf{e}_z$.

Therefore, by tracking ω_q, one can extract information about both the vortex location and the density variation near the vortex cores. To reflect the global behavior of the vortices,

such as the fluctuations in the vortex number (density), the density weighted enstrophy $Z = \int d\mathbf{x}|\omega_q|^2$ is also computed.

In the following simulations, all the physical quantities are calculated through finite difference methods with the exception of the compressible and incompressible energy spectra, which are obtained through fast Fourier transform methods.

The color scheme for the distribution plots is 'Thermal' : blue stands for the low values and red represents the high values. The values of the global quantities, such as total density, total energy and total enstrophy are averaged over the grid.

5.1 Poincaré recurrence and self-similar vortex lattice

5.1.1 Vortices as initial input

In the first sets of numerical simulations, we assume vortices are presented in the initial wave function profile. The angular momentum of this initial state is chosen to be 0 and the periodic boundary conditions are enforced. To meet these two requirements, the total wave function is taken as the product of counter rotating vortex pairs: $\psi(\mathbf{x}) = \prod_i \psi_i(\mathbf{x})$. The wave function of each single vortex takes the form: $\psi_i(\mathbf{x}) = \tanh(|\mathbf{x} - \mathbf{x}_i|)e^{\pm i\, Arg(\mathbf{x} - \mathbf{x}_i)}$, where the density at the vortex core $\rho(\mathbf{x_i}) = 0$ and $Arg(\mathbf{x} - \mathbf{x}_i) \in [-\pi, \pi)$.

We first consider 4 vortices embedded in a Gaussian BEC cloud with the initial wave function as shown in Fig 5.1. The external potential $V = 0$, while the coupling constant $g = 5.0$. The grid size is $L^2 = 512^2$, and the total number of time iteration is $T = 50'000$.

The averaged density $\bar{\rho} = \frac{1}{L^2} \int d\mathbf{x}|\psi|^2$ and the averaged total energy $\bar{E}_{tot} = \frac{1}{L^2}E_{tot}$ are both well conserved: $\bar{\rho} = 1.465 \times 10^{-4}$, $\bar{E}_{tot} = 7.082 \times 10^{-7} \pm 1.321 \times 10^{-14}$.

Since this initial profile is not an eigen-solution of the GPE, the vortices undergo a rapid expansion and sound waves are generated, as illustrated in Fig 5.2a. Correspondingly,

(a) $|\psi|$ (b) ω_q
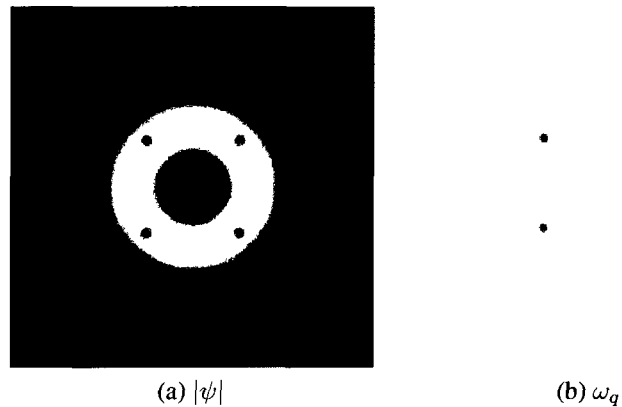
FIG. 5.1: Initial wave function with 4 vortices.

The total wave function $\psi_{tot}(\mathbf{x}) = he^{-a\,w_g\,r^2}\prod_{i=1}^{4}\psi_i(\mathbf{x} - \mathbf{x}_i)$ with $\psi_i(\mathbf{x} - \mathbf{x}_i) = \tanh(\sqrt{a}|\mathbf{x} - \mathbf{x}_i|)e^{\pm iArg(\mathbf{x}-\mathbf{x}_i)}$. The parameters are $h = 0.05, a = 0.01, w_g = 0.01$. The position of the vortices are $\{\mathbf{x}_i\} = (L/2 \pm L/8, L/2 \pm L/8)$. The vorticity plot demonstrates the direction of circulation of the vortices. Each vortex rotates in the opposite direction against its nearest neighbor.

(a) $|\psi(t = 200)|$ (b) First 2'000 iterations. Kinetic energy:
E_K, incompressible energy E_{IC}, compressible energy E_C

FIG. 5.2: Expansion of Vortices for the run with 4 embedded vortices in a Gaussian BEC cloud.

from Fig 5.2b one could see the compressible kinetic energy due to the generation of sound waves increases rapidly from almost 0, and the incompressible energy decreases dramatically.

The energy plots are displayed in Fig 5.3. The internal energy (Fig 5.3c)clearly demonstrates that the system exhibits a periodic behavior. This is very similar to the Poincare Recurrence observed in 3D quantum turbulence [36].

To examine this recurrence, one could follow the peaks of incompressible energy. Based on Fig 5.3b, we select 4 instances for a close examination: $t = 10'500$ (first black arrow), $t = 21'000$(first red arrow), $t = 31'300$(second black arrow) and $t = 41'900$(second red arrow). At these 4 times, the incompressible energy reaches a local maximum. At the moments pointed by the red arrows, the internal energy reaches 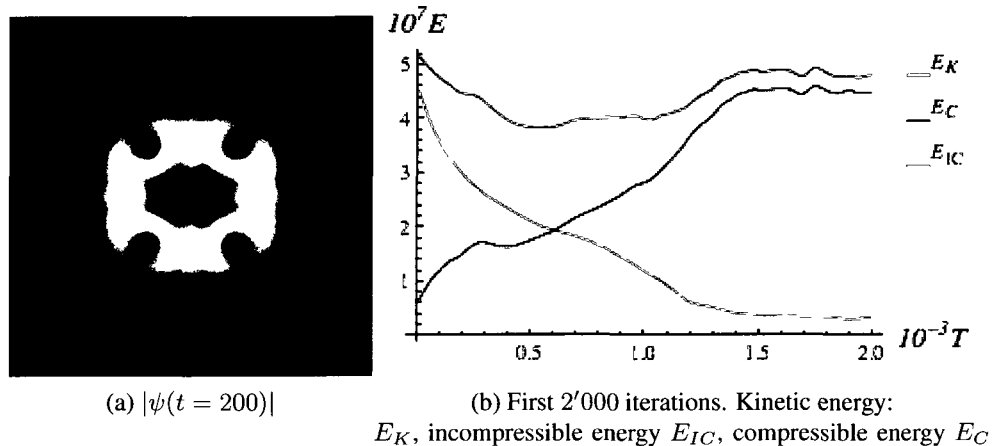local minimum embedded in a volcanic peak. The plots of the amplitude $|\psi|$ and the vorticity ω_q at these 4 times are displayed in Fig 5.4 and Fig 5.5 respectively.

At $t = 10'500$ and $t = 31'300$ (black arrows in Fig 5.3), a lattice with 16 vortices is formed. The lattice bears the same pattern of the vortices as initial wave function, while the number of Gaussian cloud quadrupled in the same domain. Simultaneously, the peak of the Gaussian cloud $(|\psi|_{max} = 0.0257)$ are almost half of the initial one's $(|\psi|_{max} = 0.05)$, which reflects the conservation of mean density. At $t = 21'000$, the number of Gaussian packets reduces to 1. This distribution of $|\psi|$ and ω_q would be the same as the initial condition if the origin of the system was shifted $x_0 \rightarrow x_0 + \frac{L}{2}e_x + \frac{L}{2}e_y$. At $t = 41'900$ the amplitude and vorticity distribution approximate the initial state, with the boundaries filled with sound wave interference and vortices.

When the distance between the neighboring vortices is reduced by $d_v = 2L/11$, the self-similar structure remains and the vortex lattice is still observed. The result is displayed in Fig 5.7. Again, similar to Fig 5.4 , $|\psi(t = 0)|_{max} = 0.05$, which is almost twice of

(a) Long time evo-
lution of the Kinetic E_K, Quantum E_Q, Internal E_I, Total E_T

(b) Long
time evolution of the Incompressible E_{IC}, Compressible E_C

(c) Long time evolution of the Internal E_I
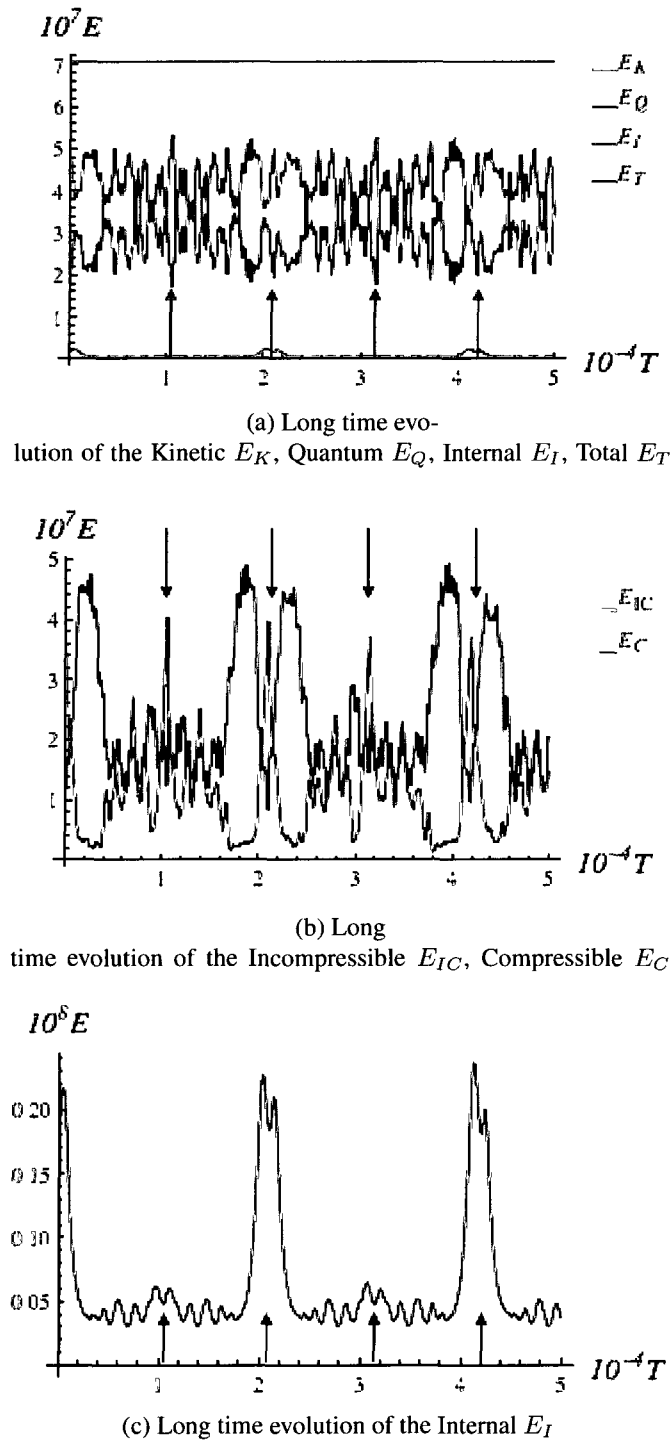
FIG. 5.3: Energy evolution with 4 vortices as initial input on a Gaussian BEC cloud.

(a) $t = 10'500$ (b) $t = 21'000$ (c) $t = 31'300$ (d) $t = 41'900$
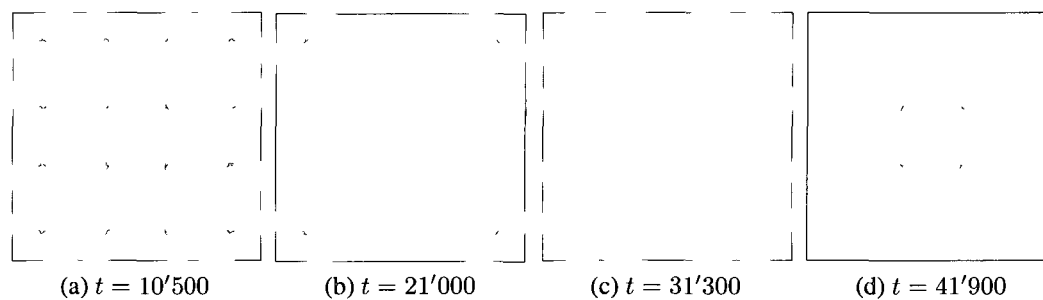
FIG. 5.4: Recurrence of $|\psi|$ for the run with 4 embedded vortices in a Gaussian BEC cloud.
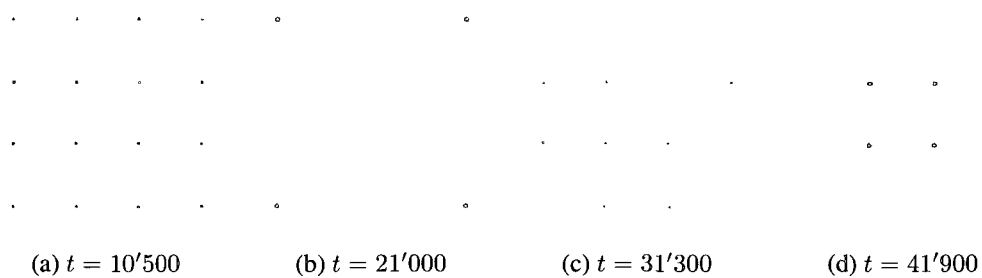
(a) $t = 10'500$ (b) $t = 21'000$ (c) $t = 31'300$ (d) $t = 41'900$

FIG. 5.5: Recurrence of ω_q for the run with 4 embedded vortices in a Gaussian BEC cloud.

(a) $t = 10'500$ (b) $t = 21'000$ (c) $t = 31'300$ (d) $t = 41'900$
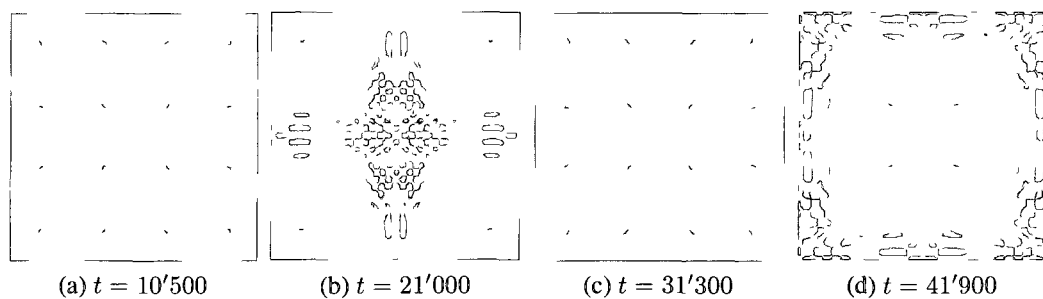
FIG. 5.6: Phase evolution for the run with 4 embedded vortices in a Gaussian BEC cloud.

(a) t=0, $|\psi|$

(b) t=0, ω_q

(c) t=0, phase

(d) t=10'500, $|\psi|$

(e) t=10'500, ω_q

(f) t=10'500, phase
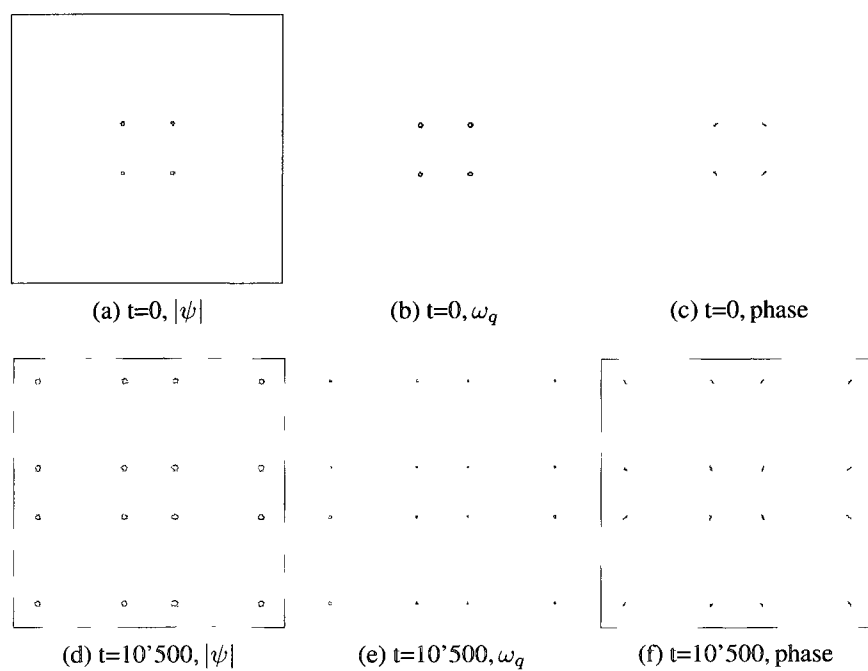
FIG. 5.7: Reduced vortex distance.

(a) t=0, $|\psi|$

(b) t=0, ω_q

(c) t=0, phase

(d) t=10'500, $|\psi|$

(e) t=10'500, ω_q

(f) t=10'500, phase

FIG. 5.8: 8 vortices as input.

(a) $t = 0$

(b) $t = 41'900$

FIG. 5.9: Phase shift.

The vortices could be identified by the singular point in phase plots. The white dash ring encircles clockwise rotating vortices (winding number -1), the black dash ring encircles counter-clockwise rotating vortices (winding number $+1$).

the value $|\psi(t = 10'500)|_{max} = 0.0256$. The 16 vortices at $t = 10'500$ demonstrates a self-similar structure as indicated by both the ω_q and the phase plots.

We now increase the number of initial vortices on the Guarssian BEC cloud from 4 to 8. The positions of these 8 vortices are $(L/2 \pm p_{1,2}L, L/2 \pm p_{2,1}L)$ with $p_1 = 0.075$, $p_2 = 0.175$. The other parameters remain the same as in the 4 vortex case.

As shown in Fig 5.8, at $t = 10'500$ the number of Gaussian packets embedded with vortices doubles and a self-similar structure is established.

To further check whether $t = 41'900$ is a Poincare Recurrence time, the phase at this instant is compared with that at $t = 0$. The result is shown in Fig 5.9. It is interesting to observe that the phase shift is different for the vortex with different winding number. The phase shift is $\delta_+ = \pi/4$ for the vortices with winding n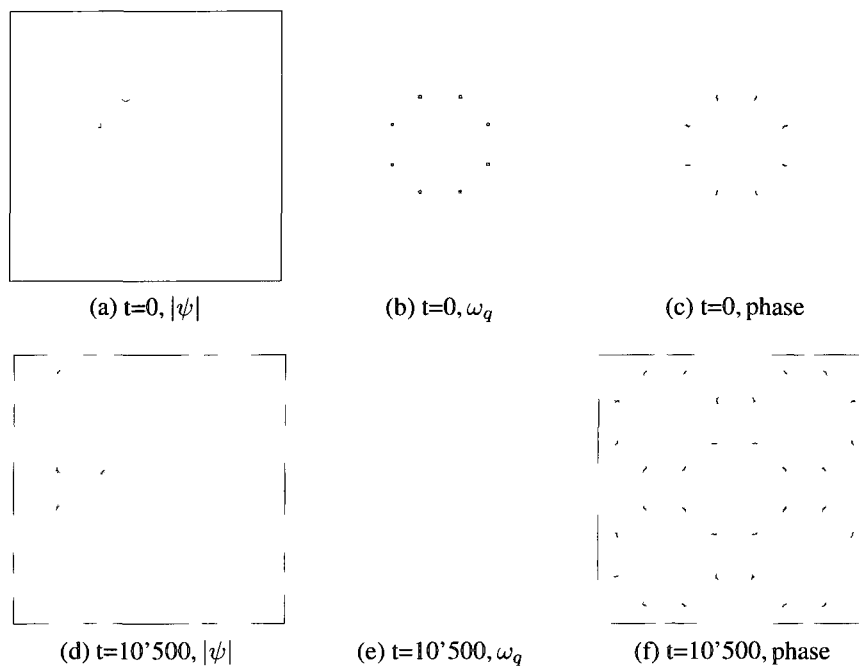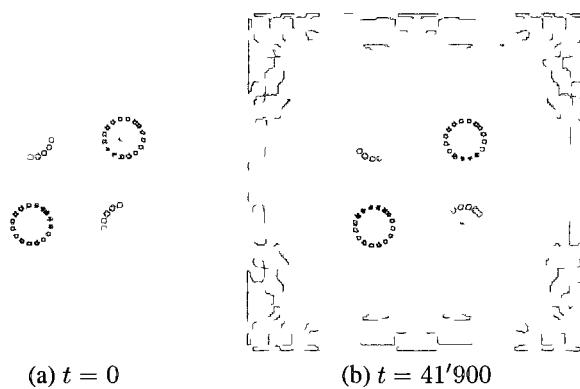umber $+1$, and $\delta_- = -\pi/4$ for those with winding number -1. Furthermore, in Fig 5.9, at the boundaries, there are many branch cuts which are the signature of quantum vortices. Despite the background sound waves, the amplitude is almost exactly restored to its original state, so that it is valid to define the time $t = 41'900$ to be a Poincaré period T_p.

5.1.2   Random phase initial condition without Gaussian cloud

A GP system with random phase fluctuation is highly energetically unstable. Randomly distributed vortices will be generated rapidly to develop turbulence. To generate the random phase, the bicubic interpolation [39] is used. The bicubic interpolation method approximate the desired 2D function $f(x, y)$ with the polynomial $p(x, y)$ defined on a unit square:

$$p(x, y) = \sum_{i=0}^{3} \sum_{j=0}^{3} a_{i,j} x^i y^j.$$

The coefficients $a_{i,j}$ are determined by the enforced continuity at 4 corners of the unit square. Typically, the continuity requirement is chosen to ensure $f(x, y)$, $\partial_x f(x, y)$, $\partial_y f(x, y)$,

$\partial_{x,y} f(x, y)$ to be continuous at the 4 corners. This amounts to 16 equations regarding the 16 coefficients $a_{i,j}$. A unique set of solution of these coefficient could be obtained. The general procedure could be described as the following:

- Discretize the domain into $m \times m$ unit squares, typically we choose $m = 8$;

- Generate 4 pseudo-random number at each corner of the unit square, totally 16 random numbers on the unit square.

- Periodicity is enforced at the boundarier;

- Compute the 16 coefficients $a_{i,j}$ from the random number generated.

To examine the impact of random fluctuation on the Poincaé recurrence, a bicubic fitted phase is employed as initial input. The simulation is run for $100'000$ iteration on a 512^2 grid. Both the averaged density and total energy are well conserved: $\bar{\rho} = 0.001 \pm 2.40 \times 10^{-15}$, $\bar{E}_{tot} = 1.390 \times 10^{-6} \pm 8.70 \times 10^{-16}$. The average ratio between internal energy and kinetic energy is $\bar{\gamma} = \dfrac{E_{int}}{E_{kin}} = 2.87 \times 10^{-3}$. The initial parameter set is given in Fig 5.10.

The evolution of the kinetic and quantum energy demonstrates the similar periodicity with the case of initial embedded vortices in a Gaussian BEC cloud.

A close examination based on Fig 5.11 reveals that around $t = 21'000$, $t = 41'900$, $t = 63'080$, $t = 83'980$, the kinetic energy rapidly increases. Compare Fig 5.3 with Fig 5.11, one could observe that at $t = 21'000$, the incompressible energy reaches local minimum. While at $t = 10'500$ and $t = 31'300$, the energy exchange between kinetic and quantum components is not distinct any more. The distribution of phase and vorticity at $t = 10'500$ is displayed in Fig 5.12. Unlike the 4 vortices case, a vortex lattice does not appear at $t = 10'500$. Instead, the vortices are randomly distributed.

What is unexpected is the disappearance of all vortices at times $t = l\dfrac{T_p}{2}$, $l = 1, 2, 3....$ When the vortices disappear, the enstrophy Z should decrease rapidly. This is exactly what

FIG. 5.10: Bicubic fitted random phase at $t = 0$.

The 512^2 grid is discretized into 8×8 subdomains for bicubic fitting. The wave function amplitude is homogenous: $h = 0.01$. Scaling parameter $a = 0.01$, the coupling constant $g = 5.0$. The phase range is $[-\pi, \pi]$. The $1st$ order derivative is periodic by construction.

we observed in the simulation. Fig 5.13 gives the details of the temporal fluctuation of the volume averaged enstophy, with the sharp minima at $l\frac{T_p}{2}$. The phase plots at the semi-Poincaé periods confirm the disappearance of the vortices. The phase and amplitude distributions of ψ are given at $t = 21'000$ and $t = 41'900$ in Fig 5.14. The range in the amplitude fluctuations at $t = T_p$ is $|\psi| \in [0.00, 0.02]$, which dramatically departs aways from the initial amplitude $|\psi| = 0.01$. Moreover, the comparison between Fig 5.14d and Fig 5.10 reveals that the phase distributions at $t = 0$ and $t = T_p$ are almost identical except for a global shift.

5.2 Energy Spectra

To study the incompressible and compressible kinetic energy spectra, we choose 4 vortices as the initial condition, as illustrated in Sect 5.1.1. For a $50'000$ iteration run, the spectra are sampled every 100 iteration. The incompressible energy spectra $s_{IC} = \partial_{\log(k)} \log[E_{ic}(k)]$, as well as the compressible energy spectra $s_C = \partial_{\log(k)} \log[E_c(k)]$ are
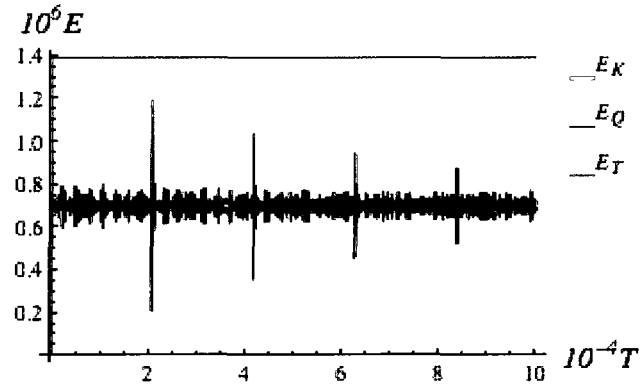
(a) Evolution of kinetic and quantum energy
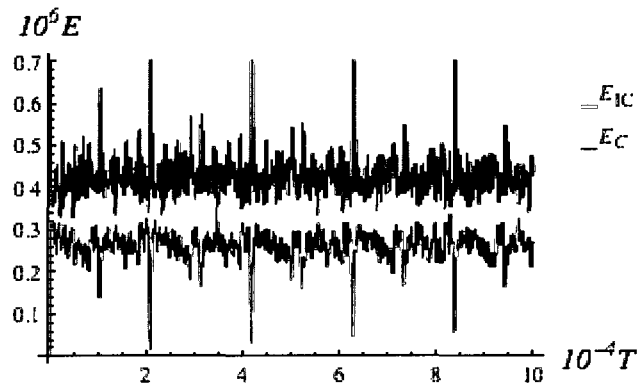
(b) Incompressible E_{IC} and Compressible E_C
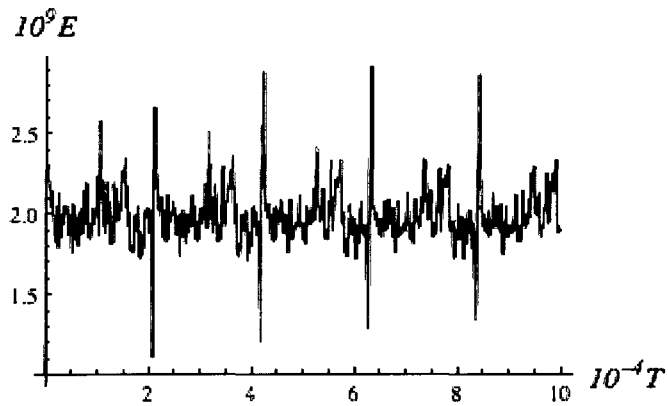
(c) Internal energy

FIG. 5.11: Energy evolution for random phase initial condition, without Gaussian cloud.

The sharp changes of the energies occur at semi Poincaré periods $\frac{lT_p}{2}, l = 1, 2, \dots$. At these times the incompressible energy decreases dramatically which indicates the depletion of all vortices. The vortices quickly emerges after these times and creates the more violent spacial fluctuation, which can be confirmed from the rapid increase of internal energy.

(a) ω_q (b) phase
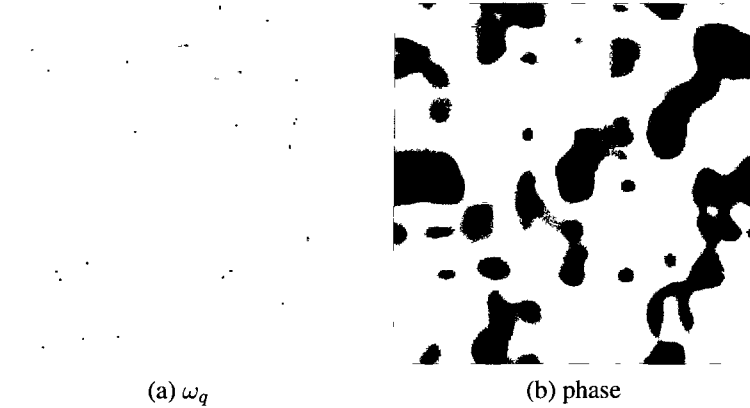
FIG. 5.12: Vortex distribution at t=10'500

In contrast to the case where vortices are embedded in a Gaussian cloud symmetrically, there is no self-similar structure developed at $\frac{T_p}{4}$. The vortices are randomly distributed (clearly viewed as the branch cuts in the phase plot) to form 2D quantum turbulence.

fitted using *Mathematica* for the wave number range $k \in [50, 100]$. The result is shown in Fig 5.15. At certain time, for instance $t \sim 17'000$, $t \sim 24'500$ and $t \sim 37'300$, s_{ic} becomes much steeper than -3. Additionally, the spectra become discontinuous at high wave number $k_h \sim 200$. We take $t = 24'500$ as an example to illustrate this change via the spectra plots Fig 5.16 and the phase evolution Fig 5.17 (the center of each phase plot is also magnified in the corresponding row). At $t = 24'400$, from Fig 5.17, one can discern that 6 branch-cuts at the center of the domain, which corresponds to 6 pairs of vortex and anti-vortex structures. The slope s_{ic} takes the standard value $s_{ic} = -3$. At $t = 24'500$, there are no singularities at over the whole domain. The vortices at the center have annihilated each other, leaving the system with no topological defects. This causes the incompressible spectra s_{ic} become discontinuous and a kink is formed as indicated by the circle in Fig 5.16. At $t = 24'600$, 4 branch-cuts emerge at the center and the incompressible slope s_{ic} approximates -3 again.

This is similar to what happens in 3D quantum turbulence [40]. In 3D case, it has
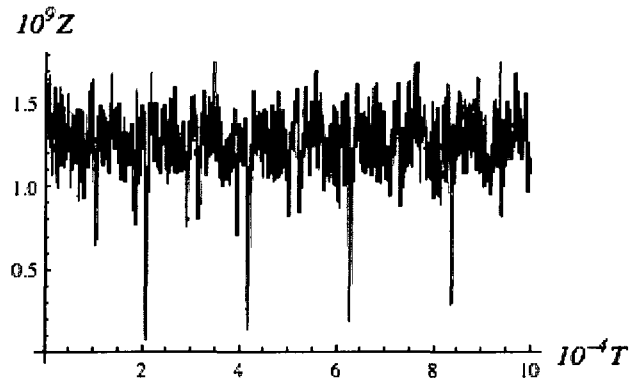
FIG. 5.13: Fluctuation of enstrophy.

(a) $|\psi|$, $t = 21'000$ (b) $|\psi|$, $t = 41'900$ (c) phase,$t = 21'000$ (d) phase,$t = 41'900$
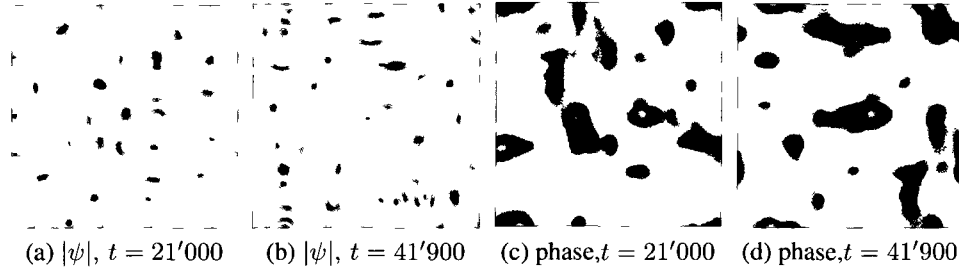
FIG. 5.14: Poincaré recurrence of random phase

Range of $|\psi|$: $[0.00,0.02]$. Albeit this radical deviation of $|\psi|$ from its initial value $|\psi(t = 0)| = 0.01$, the Poincaré recurrence can still be observed as suggested by the phase plot. The phase distribution at $t = 41'900$ is not much different than that at $t = 0$ (Fig 5.10).

been observed that the incompressible slope s_{ic} is around -3 as long as vortices exist in the system. When the vortex tubes or the vortex rings are depleted, the Kelvin-wave cascade is lost and the s_{ic} increases dramatically.

5.3   High winding number

To examine the impact of high winding number $n \geq 2$ on the Poincaré recurrence, the initial vortex wave function is chosen to be $\psi_v = \tanh(\sqrt{a}|\mathbf{x} - \mathbf{x}_i|)^n e^{\pm i n \, Arg(\mathbf{x} - \mathbf{x}_i)}$. The

(a) $s_{IC}(t)$ (b) $s_C(t)$
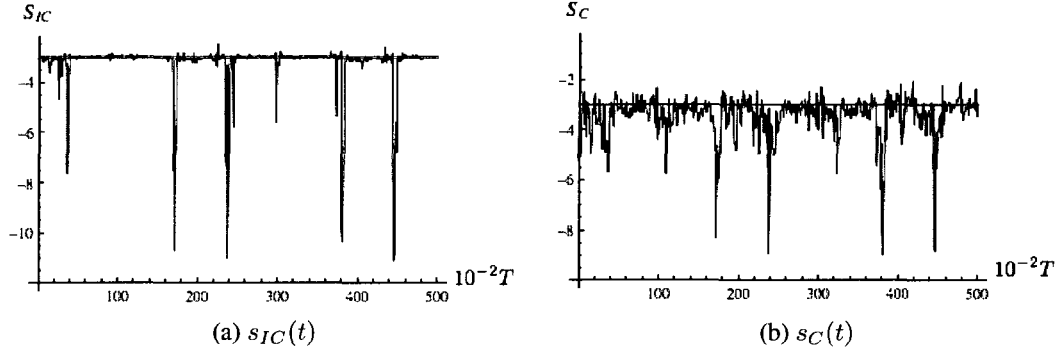
FIG. 5.15: Spectra for incompressible and compressible energy with 4 vortices as initial condition. The red line indicates the position of $k = -3$. The averaged slope for the incompressible energy is $\bar{s}_{IC} = -3.23$, while that for the compressible energy $\bar{s}_C = -3.46$.

vortex cores are located at $|\psi(\mathbf{x}_i)| = 0$.These vortices are embedded on a Gaussian BEC background so that the initial wave function is as illustrated in Fig 5.18. Both the density and total energy are well conserved in the simulations: $\bar{\rho} = 1.389 \times 10^{-4} \pm 1.212 \times 10^{-22}$; $\bar{E}_{tot} = 2.988 \times 10^{-6} \pm 1.533 \times 10^{-14}$.

With high winding number, the vortices become unstable and tend to split into the vortices with winding number 1. This is very quickly verified. Fig 5.19 demonstrates the splitting of the vortices after only 100 iterations. Since the initial degenerate state is an unstable one, the Poincaré recurrence should be viewed as reproduction of the state at the instant shortly after the degenerate vortex splitting. In this simulation, the time averaged ratio between internal energy and kinetic energy is $\bar{\gamma} = 3.628 \times 10^{-3}$. In this parameter regime, Poincaré recurrence is expected, which can be seen from Fig 5.20 at the times $\frac{1}{4}T_P, \frac{1}{2}T_P, \frac{3}{4}T_P, T_P$ pointed by the arrows. To compare with the 4 vortices case in Sect 5.1, the time instant $t = 10'500, 21'000, 31'300, 41'900$ are chosen for examination. The plots of amplitude, vorticity and phase are displayed in Fig 5.21. From the plots, it can be seen that the distribution of the vortices is very similar to that for the winding number 1

(a) $s_{ic} = -3.005$, t=24'400   (b) $s_{ic} = -5.828$, t=24'500   (c) $s_{ic} = -3.357$, t=24'600
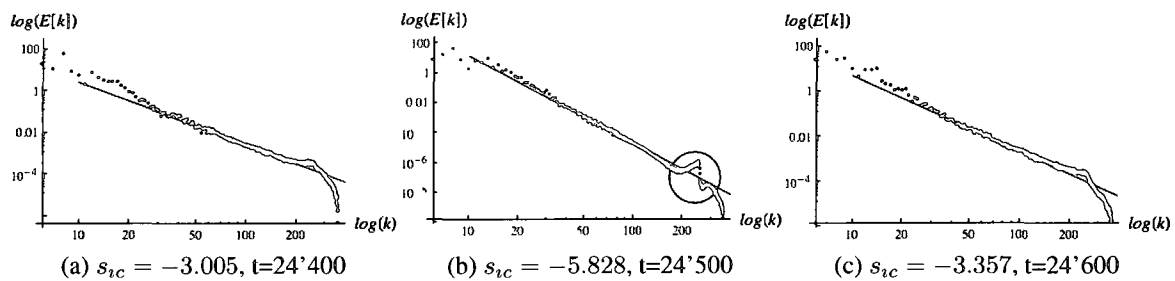
FIG. 5.16: Incompressible spectra around $t = 24'500$, fitting range $k \in [50, 100]$.

(a) phase,t=24'400   (b) phase,t=24'500   (c) phase,t=24'600

(d) blowup,center left,t=24'400   (e) blowup,center left,t=24'500   (f) blowup,center left,t=24'600
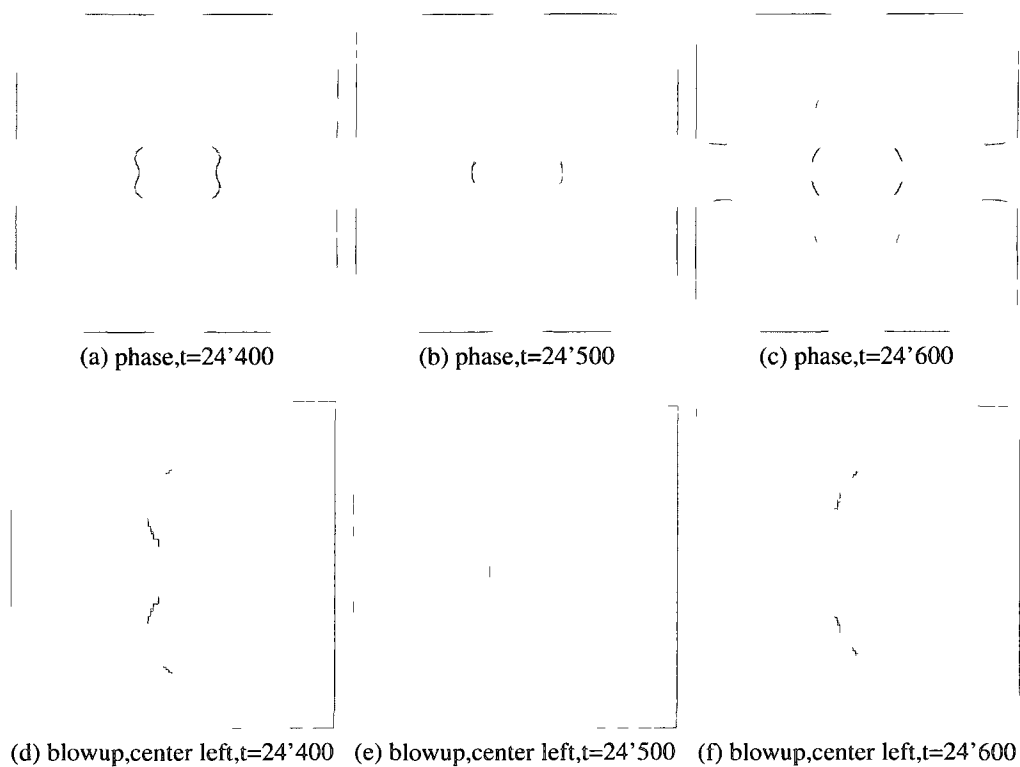
FIG. 5.17: Phase evolution around $t = 24'500$

(a) $|\psi|$ (b) ω_q (c) phase
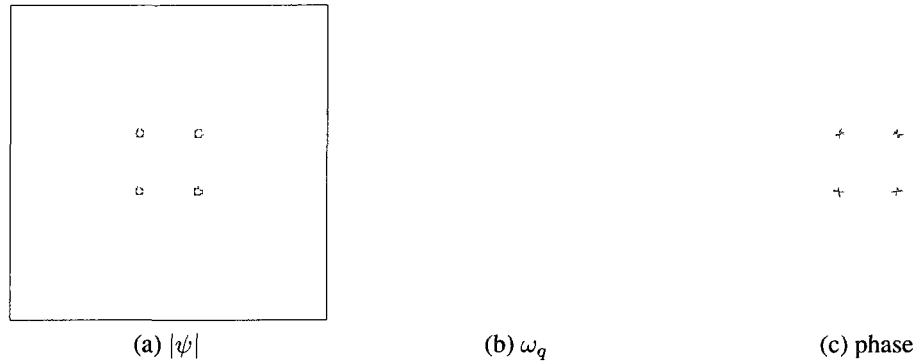
FIG. 5.18: Initial condition for winding number 2.

The initial wave function $\psi_0(\mathbf{x}) = h\,e^{-aw_g r^2} \prod_{i=1}^{4} \psi_v(\mathbf{x} - \mathbf{x}_i)$.The parameters are: $a = 0.01, g = 5.0, h = 0.05, w_g = 0.01$. The separation between neighboring vortices is $2L/11$. Winding number $n = 2$, which can be clearly identified from the 4π phase change around the singular points.

(a) ω_q (b) phase

FIG. 5.19: Splitting of degenerate vortices at $t = 100$.

In the vorticity ω_q plots, different color indicates different rotating direction of the fluid. The peaked dots corresponding to the location of the vortices. The plots are made within the domain in $[-128, 128] \times [-128, 128]$.

10^6E

3.0

2.5

2.0

1.5

1.0

0.5

$1 \quad 2 \quad 3 \quad 4 \quad 5 \quad 10^{-4}T$

$\_E_K$

$\_E_Q$

$\_E_T$
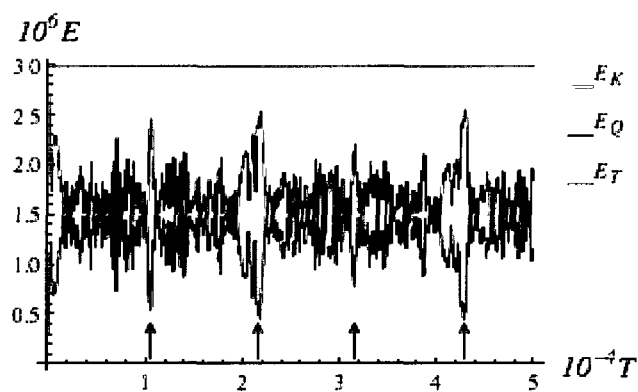
(a) Kinetic E_K, Quantum E_Q,Total E_T

10^6E

2.5

2.0

1.5

1.0

0.5

$1 \quad 2 \quad 3 \quad 4 \quad 5 \quad 10^{-4}T$

E_{IC}

$\_E_C$

(b) Incompressible E_{IC}, Compressible E_C

10^8E

2.5

2.0

1.5

1.0

0.5

$1 \quad 2 \quad 3 \quad 4 \quad 5 \quad 10^{-4}T$
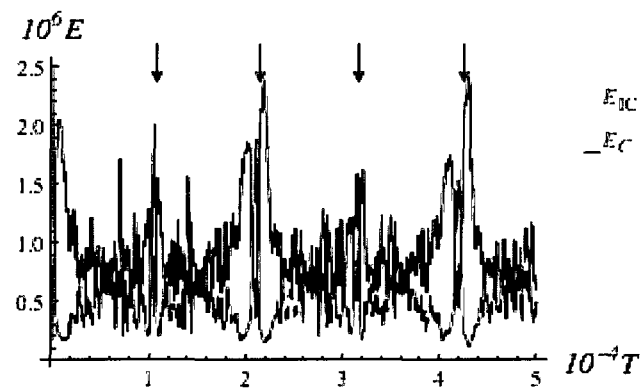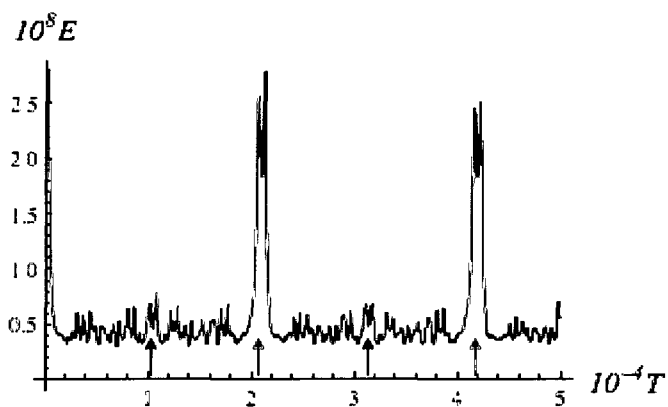
(c) Internal E_I

FIG. 5.20: Energy evolution of vortices embedded in a Gaussian cloud. The winding number is 2.

(a) $|\psi|$, t=10'500 (b) $|\psi|$, t=21'000 (c) $|\psi|$, t=31'300 (d) $|\psi|$, t=41'900

(e) ω_q, t=10'500 (f) ω_q, t=21'000 (g) ω_q, t=31'300 (h) ω_q, t=41'900

(i) phase, t=10'500 (j) phase, t=21'000 (k) phase, t=31'300 (l) phase, t=41'900
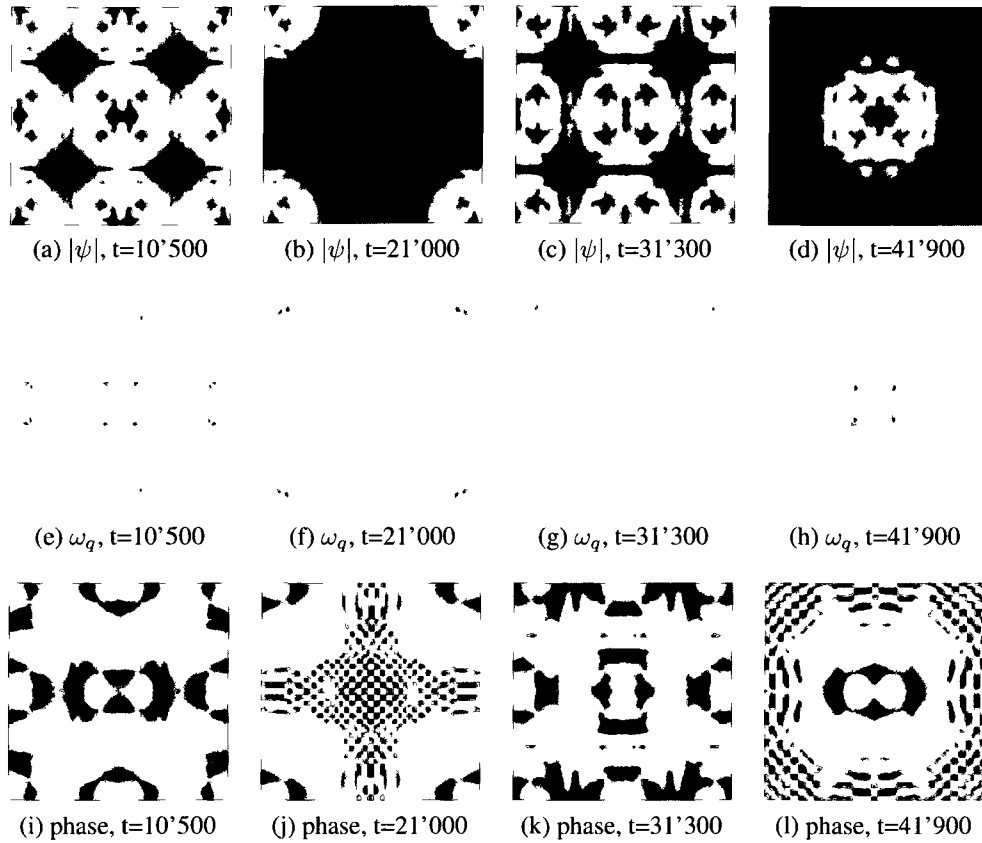
FIG. 5.21: The Poincaré recurrence for winding number 2 vortices.

The initial number of vortices is 4. Similar to the winding number 1 case, at $T_p/4$, $3T_p/4$ a self-similar structure develops. At $T_p/2$ the distribution of vortices is identical to the initial condition if the origins are shifted to $(L/2, L/2)$ with L being the domain size. At T_p, the distribution of vortices restore to its initial condition with more noise than that in the winding number 1 case.

case. A self-similar vortex structure at $t = 10'500$, $31'300$ can be clearly seen. The vortex distribution is almost identical to the $t = 41'900$ case, although more noise emerges at the boundary.

An interesting observation around $t = 10'500$, c.f. Fig 5.22, reveals that a pair of counter-rotating vortices are generated between the neighboring vortices with the same rotation. For the vortices pairs that rotate in the same direction, the space between them is filled with counter flows. When the relative velocity exceeds the critical value, the fluid become unstable and vortices will be generated to lower the energy of the system. This phenomenon is called Quantum Kelvin-Helmholtz instability (QKH) [41]. Experimentally, it has been shown that QKH could be important mechanism for vortex generation [6].

Another interesting result for $n = 2$ case is the reduction of vortex loss. The energy spectra are given in Fig 5.23. Unlike the $n = 1$ case, the slope of the incompressible spectra s_{ic} is always close to -3.0 for the fitting range $k \in [50, 100]$: $\bar{s}_{ic} = -3.086 \pm 0.010$; for compressible case $\bar{s}_c = -3.089 \pm 0.020$. This is very similar to what has been seen in 3D case [40] With high winding number as initial condition, the average density of the vortex singularities is higher than for the winding number 1 case. As a result, the energy exchange between different components becomes more frequent, as shown in Fig 5.20. Due to the higher vortex density, the QKH occurs more frequently to generate new vortices.Therefore, the averaged density of vortex singularities is higher and the probability for vortex depletion from the system become much smaller. Consequently, the spectra for the incompressible energy remains to be round -3.0 throughout the simulation.

(a) ω_q,t=10'500   (b) ω_q,t=10'600

(c) phase,t=10'500   (d) phase,t=10'600
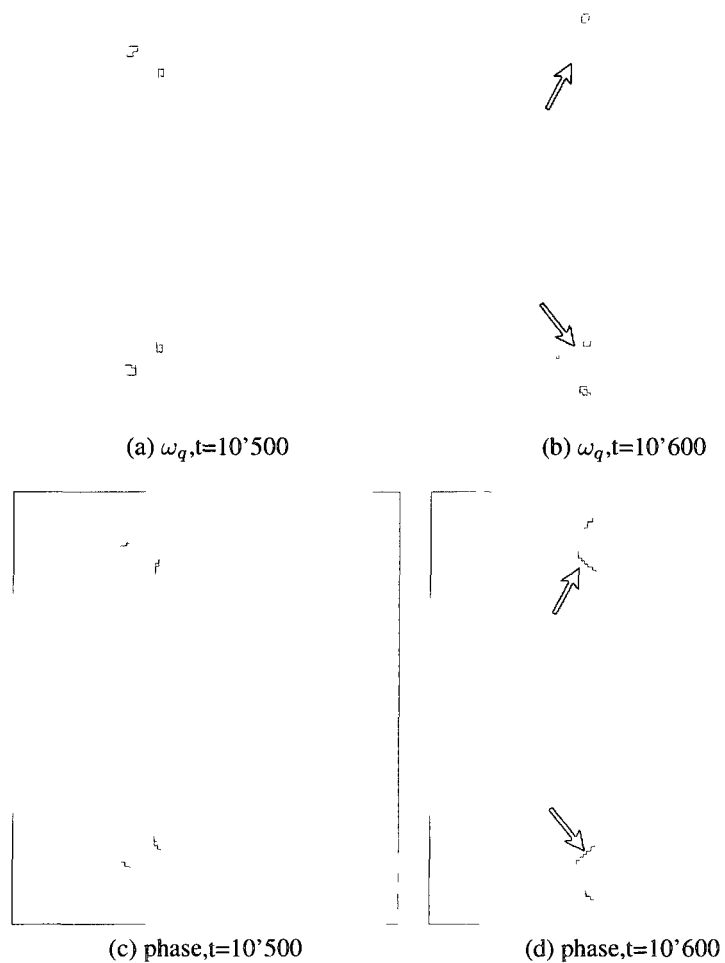
FIG. 5.22: Vortices generation.

The black arrows point towards the newly generated vortices. Notice that their rotation direction is opposite to each other as shown by the ω_q plots. The plotting domain is $[-256, -128] \times [-128, 128]$.

S_{IC}

S_C

(a) Incompressible
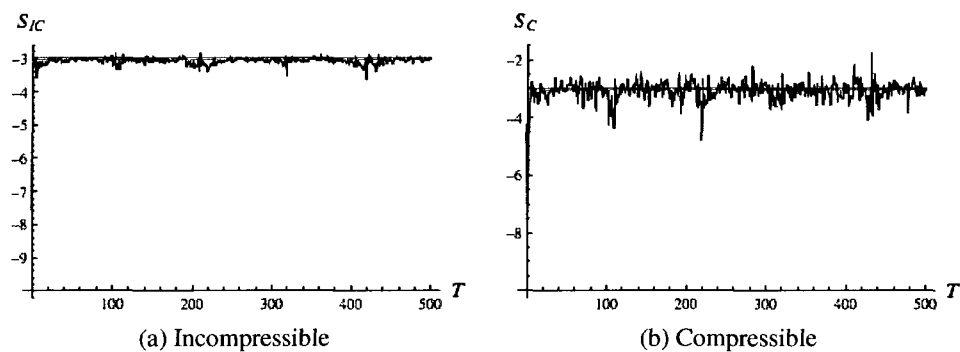
(b) Compressible

FIG. 5.23: Energy spectra for $n = 2$.

Red line indicates $k = -3.0$. Unlike the winding number 1 case, the slope of the incompressible kinetic energy is constraint to be around -3. This indicates that there is no complete depletion of the vortices during simulation.

CHAPTER 6

Medium internal energy regime

To connect the quantum turbulence with its classical counter part, the parameter regime of the quantum turbulence needs to be enlarged. This could be achieved through reducing the coherence length or by increasing the grid size. Effectively, the internal energy increases in both cases. When the internal energy is comparable with the kinetic energy, the applicable time T_b of QLG algorithm, defined to be when the energy conservation breaks down, becomes shortened. Fig 6.1c demonstrates the evolution of total energy at $\bar{\gamma} = 2.63$, where $\bar{\gamma}$ is the ratio of averaged internal energy to the averaged kinetic energy. It could be seen that the total energy has very small fluctuation within a narrow time window $t < T_b \sim 7'000$. Within this temporal range, the QLG could be deemed as an effective algorithm for simulating the GP system. The energy growth rate in Fig 6.1b has a similar growth form to the total energy evolution. It is not difficult to conjecture that the quantity $\partial_t^{(n)} E_T(t)$ is similar to $\partial_t^{(n-1)} E_T(t)$. Therefore, it can be surmised that the time evolution of the energy experiences an exponential increase after T_b. Also, the kinetic energy and quantum energy increases much faster than the internal energy. Furthermore, on comparing the growth of the kinetic energy E_K and the quantum energy E_Q, E_Q grows much faster

(a) Energy Conservation

(b) Growth rate of E_T

(c) E_T at $t < 8000$.

(d) Energy ratio E_Q/E_K
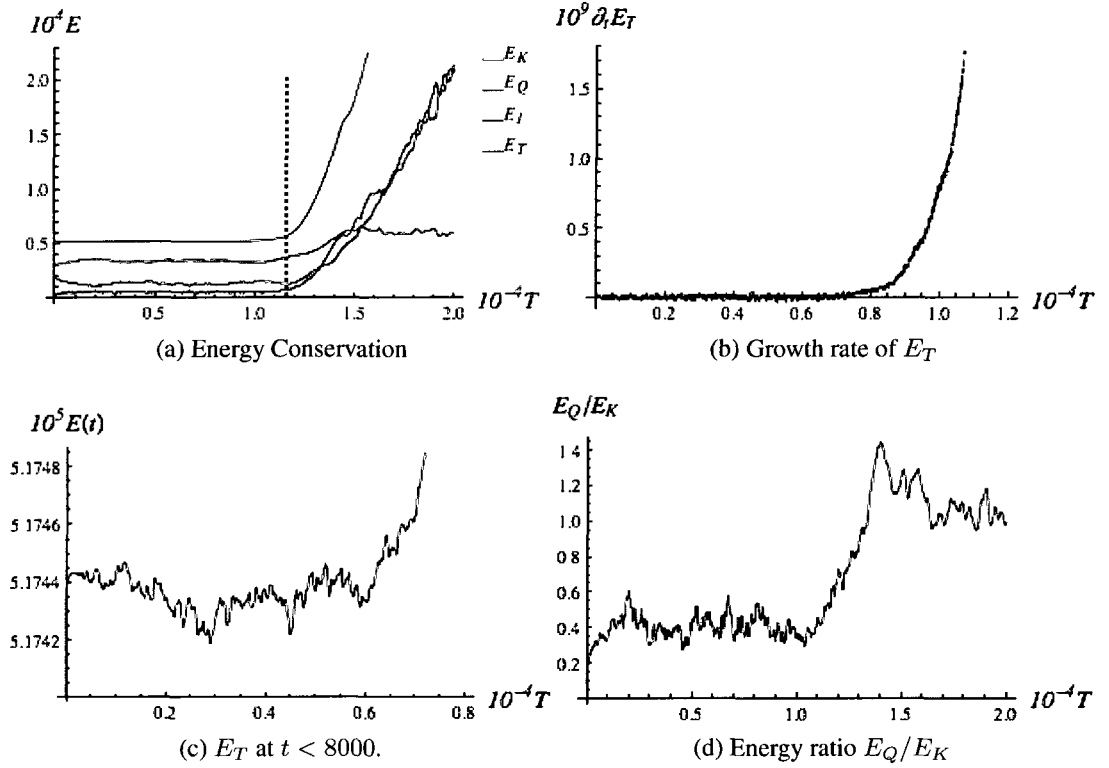
FIG. 6.1: Applicable range of QLG at high γ.

$\bar{\gamma}$ is defined to be the ratio of averaged internal energy to the averaged kinetic energy.The initial condition is 4 vortices obtained through Padé approximation (details in Appendix B). The time averaged energy ratio over $t \in [1, 8000]$ is $\bar{\gamma} = 2.623$. Time scaling parameter $a = 0.0625$, coupling constant $g = 1$, initial amplitude $h = 0.125$. Breakdown time $T_b \sim 8000$.

immediately after $t = T_b$ as indicated by Fig 6.1c. Since E_Q is defined to be $|\frac{\nabla\sqrt{\rho}}{\sqrt{\rho}}|^2$, it reflects fluctuations in the wave function amplitude, and the rapid increase of E_Q indicates that the fluctuations are too large for the current meshing parameter a to resolve. The same phenomenon is also observed in the simulation with random phase as initial input.

For the random phase initial condition, one important quantity related with the stability of the QLG algorithm is the fragmentation level, which is defined as the number of unit squares upon which bicubic fitting is applied. If the initial fragmentation level is too

high, the fluctuation of wave function amplitude will become more violent and shorten T_b. Indeed, as illustrated in Sect 6.2.1, T_b is simply inverse to the fragmentation level.

To alleviate the divergence in the total energy induced by such fluctuations, a higher temporal resolution is needed. One way to achieve this is through reducing the meshing parameter a, which equivalently reduces the potential strength ag. The other way is to use a new set of temporal/space meshing, as pointed in [42]. However, if the temporal/spacial mesh does not follow the diffusion order, the unitarity of QLG will be destroyed, which is definitely not desirable. In the ensuing simulation, we will concentrate on the valid temporal range of QLG $t < T_P$ to analyze the GP system.

6.1 Loss of Poincaré recurrence

When the time averaged ratio between internal energy and kinetic energy reaches the limit: $\bar{\gamma} \sim \mathcal{O}[10^{-2}]$, the Poincaré recurrence can't be observed. Fig 6.2 illustrates the energy plots at different γ, with the random phase initial condition.

In Fig 6.2a, the semi-Poincaré period is still visible around $t = \dfrac{T_p}{2} \sim 21'000$ at $\bar{\gamma} = 0.0567$. The rapid drop of enstrophy at this time (pointed out by the red arrow) indicates the depletion of vortices, which is exactly what is observed for the GP system with weak interaction. At $t \sim T_p$, no distinguishable peak in the kinetic energy or the quantum energy can be observed, and the enstrophy doesn't experience any sudden decline. When the internal energy is further increased, as in Fig 6.2c shows, no distinct feature around $t = \{\dfrac{1}{2}T_p, T_p\}$ could be observed. The total number of vortex doesn't reduce to 0 at any time, as reflected by the enstrophy plot. Therefore, it could be concluded that the Poincaré recurrence is destroyed.

6.2 Energy spectra

6.2.1 Random initial phase

To examine the features of 2D quantum turbulence, the random phase initial condition mentioned in Chap 5 is employed. The grid size L^2 is set to be 4096^2. The simulations were carried on the CRAY-XT4 cluster and an SGI Altix ICE with 512 cores. The wall clock time is about 6 hours for a $650'000$ iteration. Three tests are performed to investigate the break down time T_b with different fragmentation level (number of unit squares used for bicubic fitting) and energy ratio, c.f. Table 6.1, which demonstrates the inverse proportional relation between T_p and $\{\bar{\gamma}, m_f\}$, m_f being the initial fragmentation number used in bicubic fitting. The simulation with 8 fragmentation is selected here to illustrate the evolu-

Fragmentation level m_f	Energy Ratio $\bar{\gamma}$	Break down time T_b
8	0.922	650'000
16	0.917	135'000
16	0.665	225'000

TABLE 6.1: Break down time for QLG.

As expected, the more random the initial vortex state (higher m_f), the shorter the breakdown time T_b.

tion of the quantum turbulence. The effective simulation time is between $t \in [0, 650'000]$. The total energy is $\bar{E}_{tot} = 1.653 \times 10^{-7} \pm 2.015 \times 10^{-13}$. The evolution of each energy component is demonstrated in Fig 6.3, as well as variation of the enstrophy.

Since the random phase initial condition is highly energetic, a large number of vortices are rapidly generated. The generation of these vortices causes the probability density to fluctuate, which results in an increase in both the internal energy and the quantum energy. The circular motion introduced by the vortices is an important source of incompressible energy, and so the incompressible energy increases at this stage. This is confirmed in

Fig 6.4. A close examination reveals that the internal energy, enstrophy and incompressible energy reach the maximum respectively at $t \sim$ 12'250, 16'750, 25'000. These instants characterize the stage when the number of vortices reaches maximum. The next stage of the turbulent evolution is characterized by the energy transfer from incompressible energy to the compressible component. This indicates the decay in the number of vortices which can be confirmed from plot Fig 6.3d, which shows the gradual decrease of the enstrophy. The results obtained here are in good agreement with those in [23]. However, the spectra obtained in this simulation exhibit a quite different scenario.

It has been claimed in [23] that right after the vortex number reaches its maximum, the Kolmogorov 5/3 law is observed in the incompressible spectra. In our simulation, after the vortex number begin to decay, the energy spectra remain unchanged. Here the spectra at $t = 250'000$ are given as an example in Fig 6.5. The k^{-3} law is clearly observed. For the incompressible spectra, however, no 5/3 law can be obtained through fitting the data in low k region. However, for the compressible energy spectra, the region between dark dashed lines ($k \in [15, 30]$) in Fig 6.5b has a distinctive slope value $s_C = -5.484$, which is much larger than in the high k range. This could possibly suggest that the compressible energy spectrum may exhibit multiple cascades rather than the incompressible energy spectrum.

After the number of vortices starts to decay, the only major energy exchange is between the incompressible and the compressible energy, while the other energy components remains almost constant. In 3D, the collision of vortex rings produces the emission of rarefaction sound waves [43], which results in the increase of compressible energy. It could be conjectured that the same scenario can also be applied to 2D case. When the vortex density reaches the critical value, the probability for collision between counter-rotating vortices is at the maximum. The collisions prevent further generation of the vortices, and the incompressible energy, introduced mainly through circulation, is converted into sound

waves.

6.2.2 Vortices as initial input on a Gaussian BEC background

To further examine the robustness of the k^{-3} spectra, we perform the simulation with vortices as initial input. An eight-vortices set is chosen to be embedded in a Gaussian background, as illustrated in Fig 6.6. The simulation is performed on a 8192^2 grid on the Cray-XT4 cluster using 1024 cores. The computation time for 1×10^6 iteration is $20hrs$. The energy components are outputed every 100 iteration. The time evolution of each energy component is displayed in Fig 6.7.

Since the initial condition is far from an eigen-solution of the GP equation, the vortices will rapidly expand and generate sound waves. The expansion of vortices exceeds the expansion of the Gaussian wave packet, which results in the rapid buildup of the internal energy, a quantity closely related with density fluctuations. This process is accompanied by the dominance of the density diffusion from the center of the domain, which tends to minimize the fluctuation of the amplitude. After $t \sim 300'000$, the internal energy becomes almost a constant. The time averaged ratio $\bar{\gamma} = 0.144$ over $t \in [300'000, 1'000'000]$. At this stage, the vortices are generated and annihilated rapidly, as can be verified by the rapid fluctuation in the enstrophy (Fig 6.8). The spectra of both incompressible and compressible energy are very similar for $t > 300'000$. Both exhibit the monotonic k^{-3} power law at high k range as indicated by Fig 6.9. With fitting range $k \in [100, 1000]$, the time averaged incompressible spectra slope $\bar{s}_{ic} = -2.997 \pm 0.0008$.

To increase the energy ratio $\bar{\gamma}$, the size of the vortices is decreased by increasing the vortex radius factor w_v and the distance between the center of the domain and the vortex. The initial condition is detailed in Fig 6.10. The simulation is performed on on a 8192^2 grid using 1024 cores on a Cray XT4 cluster. The computation time is $24\,hrs$ for $1'161'400$

iterations. Comparing with the performance in Sect 6.2.1 (processors: 512; grid: 4096^2; walltime: $6\,hrs$; iterations $650'000$), it could be seen that the scaling is almost ideal. The discrepancy is resulted from the I/O as well as the incorporation of fast Fourier transform at each iteration step. The evolution of the energies is shown in Fig 6.11. The energy ratio $\bar{\gamma} = 0.386$. A close examination of the internal energy reveals that the initial energy evolves as in the simulation with $w_1 = 0.1$. The difference are, as shown in Fig 6.12:

- Smaller increase of internal energy: only a 0.0262% increase;

- Short-lasting expansion time: 4000 iterations.

Since the vortex is highly localized, the initial expansion of the vortices only affects the neighboring domain, which thus affects the energy components in a very limited way as compared to the expansion of the Gaussian packet. Additionally, since the vortices are further away from the center of the Gaussian peak, the fluctuations in the energy due to the expanding vortices is almost negligible. This local behavior is very similar to what happens to the vortex when the system is at the Thomas-Fermi limit in which case the kinetic energy caused by the circulation motion of vortices is negligible comparing with the nonlinear interaction. After the short expansion of the vortices, the density begins to diffuse away from the center of domain and drives the amplitude to be more homogenous. For $t > 4 \times 10^5$, the sum of the kinetic and quantum energy remains almost a constant, which signals the end of the expansion process. For this stage, the exchange between the compressible and incompressible energy is smoother. This could be explained by less vortex-generating activities. However, the incompressible energy spectra Fig 6.13, which almost doesn't alter during this stage, retains the k^{-3} power law. This is a strong indication of existence of vortices in the system.

One interesting observation is that the compressible energy spectra exhibits multiple dis-

tinct regions, which is a sign of the existence of multiple cascades. The plot Fig 6.14 reveals 3 distinct regions. The averaged slope $\bar{s}_C$ over $t \in [5 \times 10^4, 205 \times 10^4]$ is: -1.205 ± 0.021 for $k \in [50, 100]$; -3.037 ± 0.017 for $k \in [800, 2000]$.

Notice that in the intermediate range, $k \in [100, 600]$, the value of the compressible energy is much higher than the incompressible energy, as indicated in Fig 6.15, therefore the total kinetic energy could also be divided into 3 distinctive regions. This result is very similar to the one obtained in [40] which concentrates on analyzing the spectra in 3D case.

(a) Energy plot for $\bar{\gamma} = 5.67 \times 10^{-2}$

(b) Enstrophy plot for $\bar{\gamma} = 5.67 \times 10^{-2}$

(c) Energy plot for $\bar{\gamma} = 1.33 \times 10^{-1}$

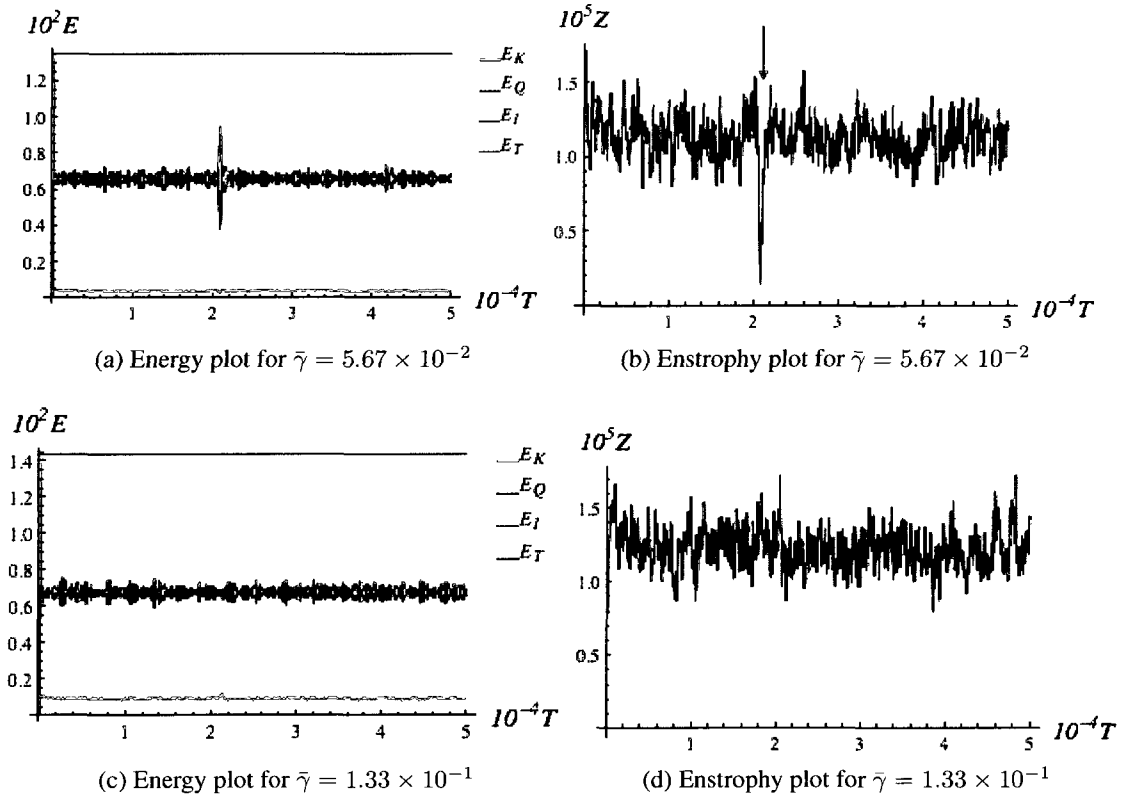(d) Enstrophy plot for $\bar{\gamma} = 1.33 \times 10^{-1}$

FIG. 6.2: Destruction of Poincaré recurrence.

Bicubic fitted random phase is chosen to be initial condition. The ratio of averaged internal energy to the kinetic energy. For $\bar{\gamma} = 0.0567$, the semi-Poincaré period is still recognizable as the sharp decay of incompressible kinetic energy. At T_p, however, the enstrophy plot indicates no depletion of vortices which is in sharp contrast with the results obtained in Chap 5. At $\bar{\gamma} = 0.133$, no Poincaré recurrence can be observed.

(a) Energy conservation. E_k: kinetic energy, E_Q: quantum energy, E_I: internal energy, E_T: total energy.

(b) Internal energy

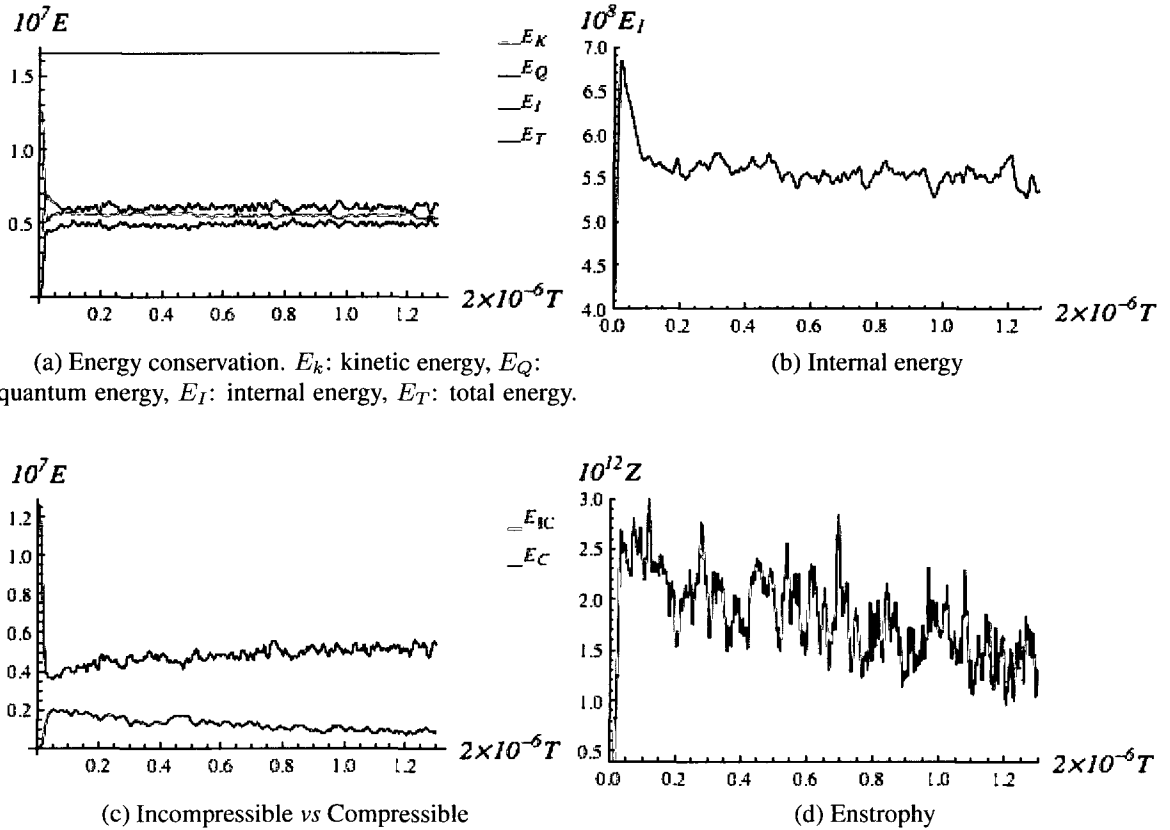(c) Incompressible *vs* Compressible

(d) Enstrophy

FIG. 6.3: Evolution of the energies and enstrophy.

The energy components are computed once per 50 iteration. The total times span displayed on the figures is $650'000$. The parameters for this simulation are: temporal step $a = 0.01$; coupling constant $g = 5.0$; amplitude $h = 0.025$.

$10^7 E$

1.5
1.0
0.5

$\_\_E_K$
$\_\_E_Q$
$\_\_E_I$
$\_\_E_T$

$0.2 \quad 0.4 \quad 0.6 \quad 0.8 \quad 1.0 \quad 2 \times 10^{-5} T$

(a) Energy conservation

$10^8 E_I$

7.0
6.5
6.0
5.5
5.0
4.5
4.0
3.5

$0.0 \quad 0.2 \quad 0.4 \quad 0.6 \quad 0.8 \quad 1.0 \quad 2 \times 10^{-5} T$

(b) Internal energy

$10^7 E$

1.2
1.0
0.8
0.6
0.4
0.2

$\_\_E_{IC}$
$\_\_E_C$

$0.2 \quad 0.4 \quad 0.6 \quad 0.8 \quad 1.0 \quad 2 \times 10^{-5} T$

(c) Incompressible vs Compressible

$10^{12} Z$

3.0
2.5
2.0
1.5
1.0
0.5
0.0

$0.0 \quad 0.2 \quad 0.4 \quad 0.6 \quad 0.8 \quad 1.0 \quad 2 \times 10^{-5} T$
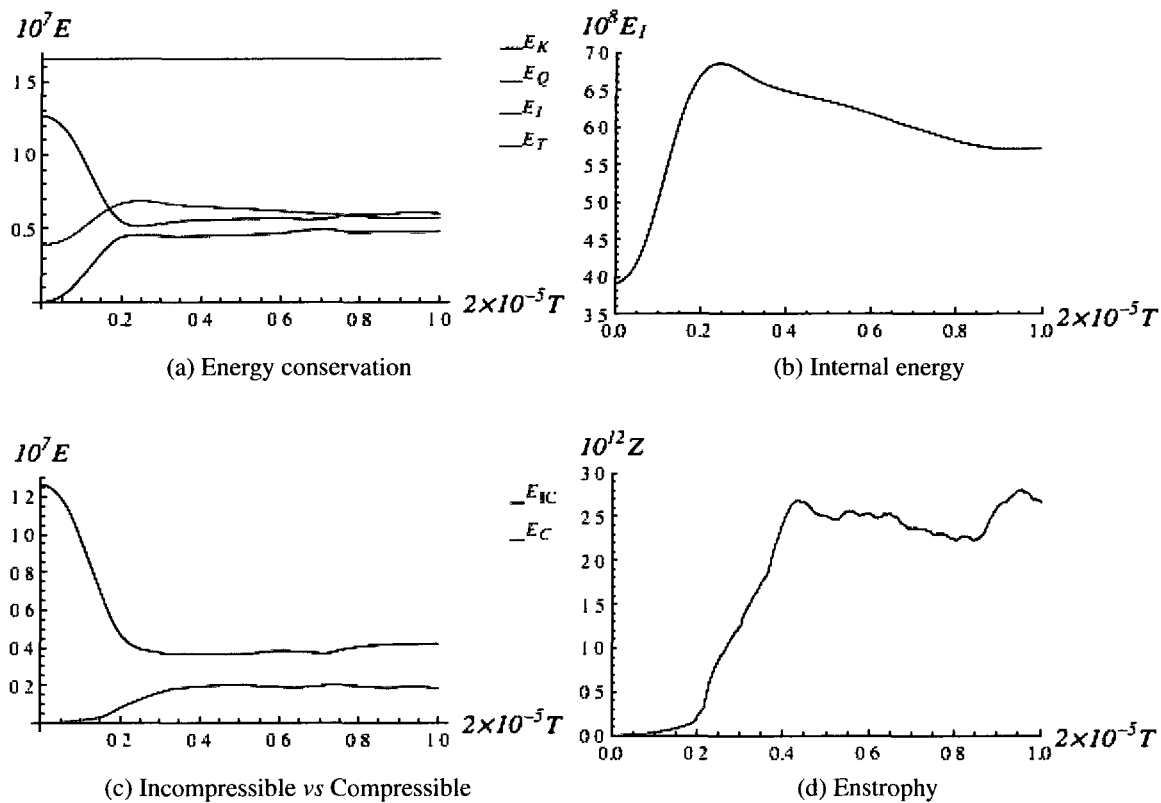
(d) Enstrophy

FIG. 6.4: Blowup of $t \in [0, 5'0000]$.

The first $50'000$ is characterized by the rapid generation of vortices. This can be confirmed by the rapid increase of internal energy and the incompressible kinetic energy. The enstrophy reaches its maximum round $t = 20'000$, indicating the vortex number has reached its maximum.
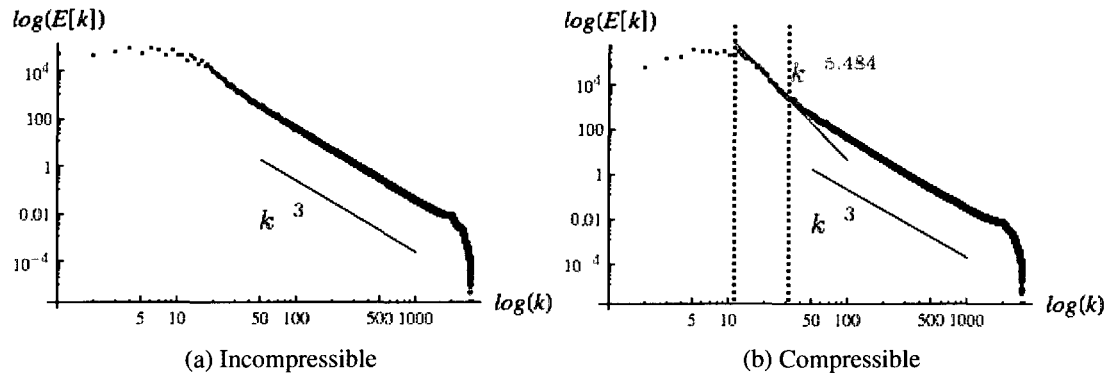
(a) Incompressible   (b) Compressible

FIG. 6.5: Spectra for medium interaction regime.

The slopes are: incompressible $s_{ic} = -3.004$; compressible $s_c = -3.024$. The space between the black dashed lines is the intermedium region between low k (almost flat) and high k (k^{-3} law).
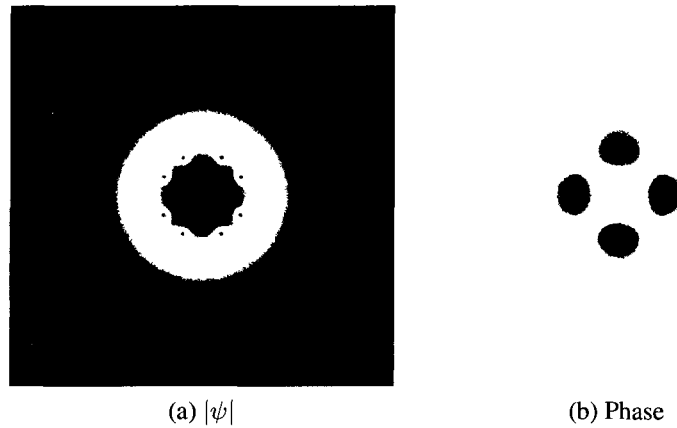

(a) $|\psi|$ (b) Phase

FIG. 6.6: Vortex input on Grid=8192^2.

The vortices in the same quadrant have the same charge, while vortices at neighboring quadrant have opposite charge. The amplitude of each vortices has the form of $\tanh[w_v \sqrt{a}\, r]$. The parameters in this simulation are: time step $a = 0.01$; coupling strength $g = 5.0$; initial wave function amplitude $h = 0.025$; vortex radius factor $w_v = 0.1$. The distance between each vortex and the center is 916 lattice units. Winding number $n = 1$.
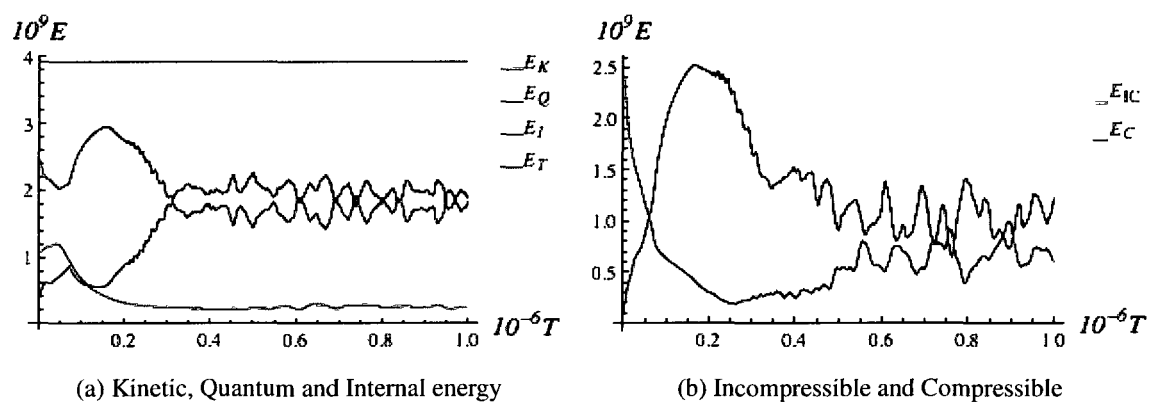
(a) Kinetic, Quantum and Internal energy   (b) Incompressible and Compressible

FIG. 6.7: Evolution of energies with vortices embedded in a Gaussian background.
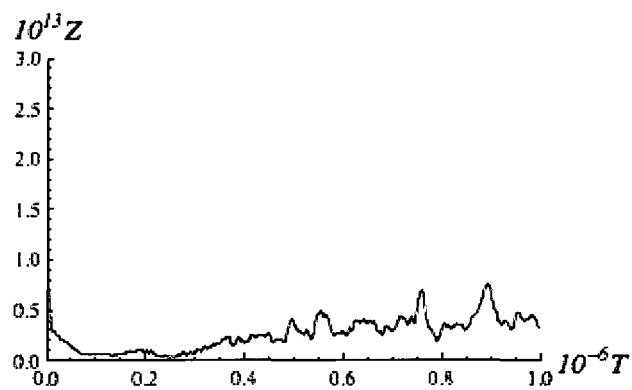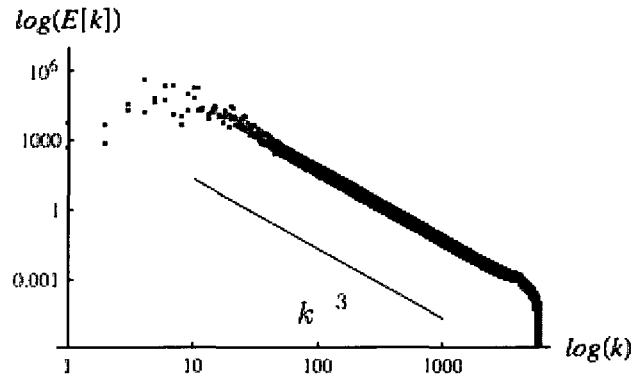

FIG. 6.8: Enstrophy fluctuation.

FIG. 6.9: The spectra for Compressible and Incompressible.

The red color stands for the incompressible spectra, blue for the compressible one. The purple line shows the k^{-3} power law.
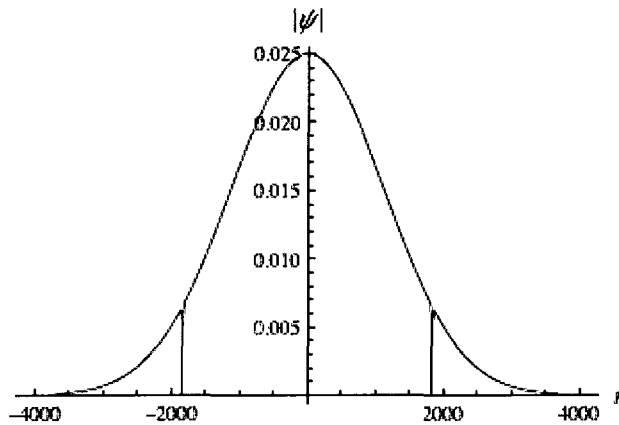

FIG. 6.10: Intersection with $y = 2x$.

The dips around ± 2000 indicate the position of the two vortices. The displacement factor for 8 vortices are $d_1 = 0.1$, $d_2 = 0.2$. The vortices are positioned at $(\pm d_1 L, \mp d_2 L)$ and $(\pm d_2 L, \mp d_1 L)$. Vortices in the same quadrant have the same charge; neighboring quadrants host opposite charges. Initial amplitude $h = 0.025$, coupling strength $g = 5.0$, Gaussian width $w_g = 4 \times 10^{-5}$, vortex radius factor $w_v = 1$. The vortices are highly localized. The bulk density $\bar{\rho}$ is larger than in previous simulation, as is the internal energy.

(a) Energy evolution
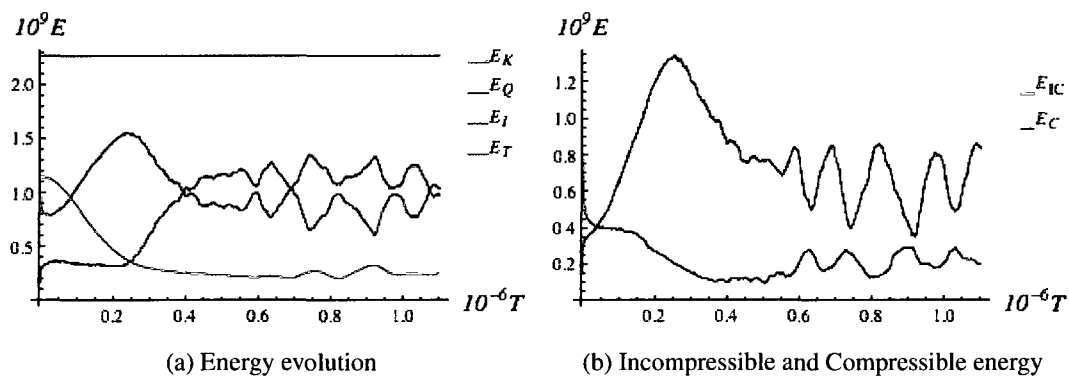
(b) Incompressible and Compressible energy

FIG. 6.11: Energy conservation for vortex radius factor $w_v = 1$.

The energy components are stored every 100 iteration. Compare this result with that in Fig 6.7, there are less fluctuations in the energies, a sign indicating less vortices being generated or annihilated.
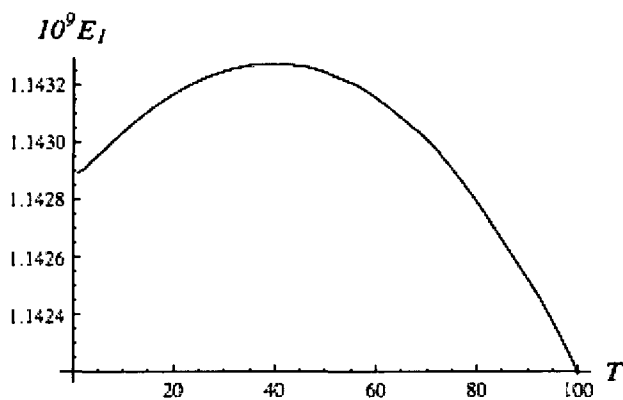
FIG. 6.12: Increase of internal energy for $t \in [0, 10000]$, $w_v = 1$.
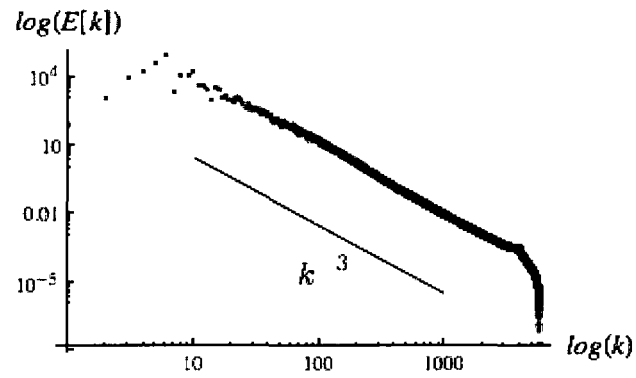
FIG. 6.13: Incompressible spectra at $t = 10^6$.

$s_{IC} = 2.998$ with fitting range $k \in [500, 2000]$. The incompressible spectra almost monotonically follows the k^{-3} power law between $k \in [20, 2000]$.
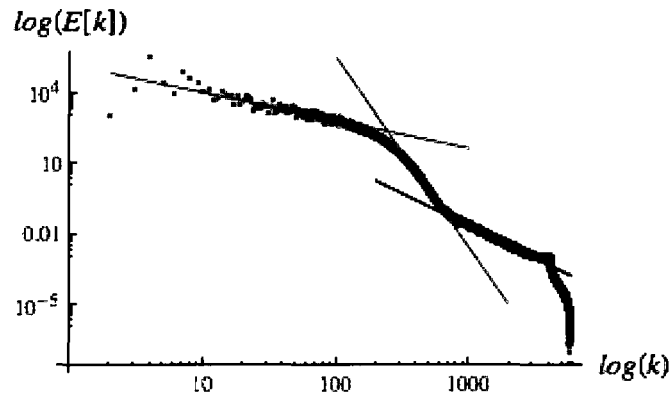
FIG. 6.14: Compressible energy spectra at $t = 10^6$.

Red line: $k^{-1 \ 192}$, fitting range $k \in [50, 100]$; Green line: $k^{-8 \ 117}$, fitting range $k \in [500, 600]$; Purple line: $k^{-2 \ 762}$, fitting range $k \in [800, 2000]$.

FIG. 6.15: The comparison between E_{IC} and E_C at $t = 10^6$.

Red colored spectra is the *Incompressible*, blue colored being the *Compressible* kinetic energy.

CHAPTER 7

Conclusion and Outlook

The QLG algorithm has proven to be an efficient method to simulate the nonlinear GP system when the internal energy is at most comparable with the kinetic energy. The unitarity embedded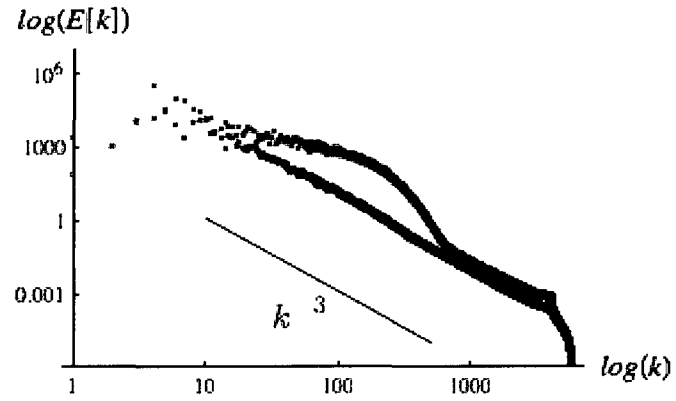 in QLG enables the unconditional conservation of density. For the low internal energy case ($E_{int} \lesssim 0.01 E_{kin}$), the accuracy of QLG could conserve the total energy to 10 significant digits, which rivals any other highly accurate method.

For 2D quantum turbulence, the ratio $\bar{\gamma}$ between the internal energy and the kinetic energy is crucial in determining whether Poincaré recurrence could be observed. It has been demonstrated in our numerical simulations that when $\bar{\gamma} \lesssim 0.05$, Poincaré recurrence occurs at a short time T_P, and this occurrence time is independent of initial conditions. When $\bar{\gamma} > 0.05$, the Poincaré recurrence is destroyed.

The spectral analysis of our simulations reveals that there is no evidence for a $k^{-5/3}$ power law for the incompressible energy in the regime $\bar{\gamma} \lesssim 1$ The incompressible energy spectra always exhibited a k^{-3} wave number dependence, which is closely associated with the existence of vortices. When the vortices are depleted from the system, the incompressible spectra shows a steeper slope and a discontinuity at high wave numbers. It is the

compressible energy spectra that demonstrates multiple distinctive regions in the spectra, and this multiple power law is dependent on the initial condition. A possible explanation is that the quantum fluid doesn't satisfy enstrophy conservation, which is the cornerstone for existence of dual cascade. To thoroughly examine the transition between 2D quantum turbulence and 2D classical turbulence, one needs to perform simulations at the Thomas-Fermi regime which is beyond the current capability of QLG.

The next stage of extending this research will be focused on broadening the applicable parameter range of QLG. Since the unitary feature of QLG is built upon diffusion ordering, which locks the temporal/spatial mesh, a modification of QLG to accommodate large internal energy poses an interesting challenge. Furthermore, many interesting quantum phenomenon involves rotation, such as the generation of vortices arrays in a rapidly rotating frame. To study these problems, QLG needs to be modified to incorporate boundary conditions other than periodicity, and the angular momentum operator $\hat{\mathcal{L}} = \mathbf{r} \times \hat{\mathcal{P}}$ also needs to be incorporated into the local unitary collision streaming operation.

Although QLG demonstrates almost ideal scalability on large number of processors, improving its I/O performance is challenging on huge grids. A close examination of the paralleled I/O routine, such as HDF5, could provide a better insight about optimization of QLG on large clusters. At the current stage, the QLG codes are written with MPI libraries which target distributed memory architecture. To improve the performance of QLG, the thread-sharing model, such as OpenMP, could be combined with MPI. This approach is becoming more and more promising with the impending peta-scale clusters equipped with larger shared memory nodes. However, because of the extremely uniform load balancing over the nodes of the QLG algorithm, initial experiments by Jost [private communications] showed little gain in utilizing openMP-MPI hybrid on a large number of cores (cores>1024).

APPENDIX A

Conservation Laws

Neother's theorem states that if a transformation of a physical system leaves its action unchanged, then there exists a conservation law associated with this transformation. To derive the conservation laws of the quantum fluid, the Einstein notation is used and ∂_a designates as a 4 dimensional Euclidean derivative.

The lagrangian density of GPE governed BEC system is:

$$\mathscr{L} = \frac{\imath}{2}(\bar{\psi}\partial_t\psi - \psi\partial_t\bar{\psi}) - |\nabla\psi|^2 - \frac{g}{2}|\psi|^4 - V(\mathbf{x},t)|\psi|^2.$$

To derive the conservation laws, one could perform the following transformation with η being a small real number.

- Phase rotation:

$$\psi \rightarrow \psi e^{\imath\eta} = \psi + \imath\eta\psi + \mathcal{O}[\eta^2];$$

$$\bar{\psi} \rightarrow \bar{\psi}e^{-\imath\eta} = \bar{\psi} - \imath\eta\bar{\psi} + \mathcal{O}[\eta^2];$$

$$\mathscr{L} \rightarrow \mathscr{L}.$$

The invariance of $\mathscr{L}$ results in density conservation:

$$\partial_a[\frac{\partial\mathscr{L}}{\partial(\partial_a\psi)}\delta\psi + c.c.] = \partial_t(\bar{\psi}\psi) + i\nabla \cdot (\psi\nabla\bar{\psi} - \bar{\psi}\nabla\psi)$$

$$= \partial_t\rho + \nabla \cdot (\rho\mathbf{v})$$

$$= 0,$$

where the density $\rho = \bar{\psi}\psi$, and the fluid momentum $\rho\mathbf{v} = i(\psi\nabla\bar{\psi} - \bar{\psi}\nabla\psi)$.

- Space translation:

$$\psi \rightarrow \psi(x_a + \eta_a) = \psi(x) + \eta_a\partial_a\psi(x) + \mathcal{O}[\eta_a^2];$$

$$\bar{\psi} \rightarrow \bar{\psi}(x_a + \eta_a) = \bar{\psi}(x) + \eta_a\partial_a\bar{\psi}(x) + \mathcal{O}[\eta_a^2];$$

$$\mathscr{L} \rightarrow \mathscr{L}(x_a + \eta_a) = \mathscr{L}(x) + \eta_a\partial_a\mathscr{L}(x) + \mathcal{O}[\eta_a^2].$$

The conservation of energy and momentum could be expressed through the 4×4 tensor:

$$T_{a,b} = \frac{\partial\mathscr{L}}{\partial(\partial_a\phi_\gamma)}\partial_b\phi_\gamma - \mathscr{L}\delta_{a,b}, \tag{A.1}$$

where $\{\phi_\gamma\}$ are the fields in $\mathscr{L}$. In this case, $\phi_1 = \psi$, $\phi_2 = \bar{\psi}$. The tensor obeys the following equation [44]:

$$\partial_a T_{a,b} = -\partial_b\mathscr{L}.$$

The total energy is conserved when $\partial_t\mathscr{L} = 0$, which produces:

$$\partial_a T_{a,0} = 0.$$

Momentum conservation holds provided $\partial_{x_i}\mathscr{L} = 0$. The conservation of momentum along i direction is:

$$\partial_a T_{a,i} = 0.$$

A useful set of equations are listed below to map wave function ψ, $\bar{\psi}$ into hydrodynamic variable density ρ and current $\rho\mathbf{v}$.

$$
\left.\begin{aligned}
\partial_i\rho &= \psi\partial_i\bar{\psi} + \bar{\psi}\partial_i\psi \\
-i\rho v_i &= \psi\partial_i\bar{\psi} - \bar{\psi}\partial_i\psi
\end{aligned}\right\} \Rightarrow
\left\{\begin{aligned}
\psi\partial_i\bar{\psi} &= \frac{1}{2}(\partial_i\rho - i\rho v_i) \\
\bar{\psi}\partial_i\psi &= \frac{1}{2}(\partial_i\rho + i\rho v_i)
\end{aligned}\right.
\tag{A.2}
$$

For the momentum conservation in the x direction, the related tensor components are:

$$
T_{t,x} = \frac{i}{2}(\bar{\psi}\partial_x\psi - c.c.)
$$

$$
T_{x,x} = -2\partial_x\psi\partial_x\bar{\psi} - \mathscr{L}
$$

$$
T_{y,x} = -\partial_y\bar{\psi}\partial_x\psi - c.c.
$$

$$
T_{z,x} = -\partial_z\bar{\psi}\partial_x\psi - c.c.
$$

The term $T_{t,x}$ is nothing but the current in x direction:

$$
T_{t,x} = -\frac{1}{2}\rho v_x
$$

To map $T_{x,x}$ into $\{\rho, \rho\mathbf{v}\}$, one resorts to the GPE to eliminate $\partial_t\psi$ and $\partial_t\bar{\psi}$. By using (A.2), it could be shown that:

$$
T_{x,x} = -\frac{1}{2}\{g\rho^2 - \nabla^2\rho + \frac{1}{\rho}[(\partial_x\rho)^2 + (\rho v_x)^2]\}.
$$

After multiplying both denominator and numerator with ρ, the terms $T_{y,x}$ and $T_{z,x}$ could be mapped to the following expression through (A.2):

$$
T_{y,x} = -\frac{1}{2\rho}[\partial_x\rho\partial_y\rho + \rho^2 v_x v_y]
$$

$$
T_{z,x} = -\frac{1}{2\rho}[\partial_x\rho\partial_z\rho + \rho^2 v_x v_z]
$$

Consider the case when $V = 0$. Applying the conservation law $\partial_a T_{a,x} = 0$ and noticing that $\frac{1}{\rho}\partial_a\rho\partial_b\rho = 4\partial_a\sqrt{\rho}\partial_b\sqrt{\rho}$, one finally arrives at momentum conseravtion:

$$
\partial_t(\rho v_x) + \partial_i[\rho v_i v_x + 4\partial_i\sqrt{\rho}\partial_x\sqrt{\rho} + g\rho^2 - \nabla^2\rho] = 0
$$

The y-direction and z-direction conservation can be obtained in the same way.

- Time translation. The relevant terms for energy conservation in tensor T are:

$$T_{t,t} = \nabla\bar{\psi} \cdot \nabla\psi + \frac{g}{2}|\psi|^4 + V|\psi|^2;$$

$$T_{i,t} = -\nabla\bar{\psi}\partial_t\psi + c.c. \qquad , i = x, y, z.$$

Using the same technique as in the space translation, one could express these tensor elements in the $\{\rho, \rho\mathbf{v}\}$ representation:

$$T_{t,t} = |\nabla\sqrt{\rho}|^2 + \frac{1}{4}\rho v^2 + \frac{g}{2}\rho^2 + V\rho;$$

$$T_{i,t} = \frac{1}{2\rho}[\partial_i\rho\nabla \cdot (\rho\mathbf{v}) - \rho v_i \nabla^2\rho] + \frac{1}{4\rho^2}\rho v_i(\nabla\rho \cdot \nabla\rho + \rho^2 v^2) + (g\rho + V)\rho v_i.$$

If the external potential is only dependent on position $V = V(\mathbf{r})$, the conservation of energy then is formulated as:

$$\partial_t\{2|\nabla\sqrt{\rho}|^2 + \frac{1}{2}\rho v^2 + g\rho^2 + 2V\rho\} = \qquad (A.3)$$

$$- \nabla \cdot \{\rho\mathbf{v}(2g\rho + 2V) + \frac{1}{2}\rho v^2\mathbf{v} - \frac{\nabla\rho}{\rho}\nabla \cdot (\rho\mathbf{v}) - 2\sqrt{\rho}\mathbf{v}\,\nabla^2\sqrt{\rho}\}.$$

APPENDIX B

Padé Approximation

To approximate a divergent function $f(x)$, the Taylor expansion requires that all the coefficients of the polynomials need to be known, which is not practical for numerical purposes and so a different summation routine is desired. Among the alternatives, Padé summation usually provides good estimate of $f(x)$ and only requires finite numbers coefficients in the asymptotic representation.

The idea of Padé summation is to use rational polynomials to represent the $f(x)$. A typical Padé series reads:

$$P_M^N = \frac{\sum\limits_{n=0}^{N} a_n \, x^n}{1 + \sum\limits_{m=1}^{M} b_m \, x^m}. \tag{B.1}$$

The coefficients $\{a_n, b_m\}$ are determined by the asymptotic behavior of $f(x)$ at the boundaries. During the process, it could be found that $\{a_n, b_m\}$ is constructed from a finite set $\{a_0, ..., a_p; b_1, ..., b_q\}$.

To study the vortices in the GP system, it is convenient to represent the GPE in polar coordinates. The vortex solution takes the form $\psi = A(r)e^{i l \theta}$, with l being the winding

number. Inserting this function into the GPE, one arrives at the radial equation:

$$A''(r) + \frac{1}{r}A'(r) - \frac{l^2}{r^2}A(r) + [1 - A^2(r)]A(r) = 0.$$

The boundary condition for the vortex amplitude is set to be $A(r \to 0) = 0$ and $A(r \to \infty) = 1$. The asymptotic forms around $r = 0$ and $r = \infty$ are:

$$r \to 0 : A(r) = r^l \sum_{i=1} a_i r^{2i-1};$$

$$r \to \infty : A(r) = \sum_{j=1} b_j r^{-2j}.$$

This asymptotic form (even order separated from odd order) allows one to employ the modified Padé approach [9], which states that $A(r)$ could be approximated by the square root of the rational functions:

$$Q_M^N = r^l \sqrt{\frac{\displaystyle\sum_{n=0}^{N} a_n x^{2n}}{1 + \displaystyle\sum_{m=1}^{M} b_m x^{2m}}}.$$

Since $A(r \to \infty) = 1$, one could set $M = N+l$ and $b_M = a_N$. To simplify the asymptotics, one can resort to the differential equation for the density $A^2(r)$, thereby eliminating the square root:

$$\rho''(r) + \frac{1}{r}\rho'(r) - \frac{1}{2\rho(r)}[\rho'(r)]^2 - \frac{2l^2}{r^2}\rho(r) + 2[1 - \rho(r)]\rho(r) = 0. \qquad \text{(B.2)}$$

Inserting Q_M^N into Eq B.2, and matching different orders of r and setting their coefficients to 0, the $M + N$ coefficients can be determined from $M + N$ equations. To illustrate this procedure, the winding number $l = 1$ is taken as an example. Consider first the Padé order $\{N, M\}$ with $N = 1$ and $M = 2$. The density is approximated by :

$$\rho(r) = r^2 \frac{a_0 + a_1 r^2}{1 + b_1 r^2 + a_1 r^4}.$$

3 equations are needed to solve the coefficients. The 3 equations are the 3 coefficients of r^2, r^4, r^6, on equating these coefficients to 0, one arrives at:

$$\sim r^2 : a_0 = \frac{4a_1}{4b_1 - 1};$$

$$\sim r^4 : a_1 = 0; \quad a_1 = \frac{-5 + 68b_1 - 192b_1^2}{128 - 768b_1};$$

$$\sim r^6 : b_1 = \frac{5}{48}; \quad b_1 = \frac{1}{8}; \quad b_1 = \frac{1}{3}.$$

Since the density should be non negative, the only meaningful solution obtained above is $\{a_0 = \frac{11}{32}, a_1 = \frac{11}{384}, b_1 = \frac{1}{3}\}$. Table B.1 gives the Padé coefficients for different winding number l when $N = 1$.

When the 2D GP system contains multiple vortices, the total wave function will be ap-

Coefficients	$l = 1$	$l = 2$	$l = 4$
a_0	0.34375	0.025644	1.134241×10^{-5}
a_1	0.0286458	0.000626418	7.93214×10^{-8}
b_1	0.333333	0.191094	0.105909
b_2	-	0.0196963	6.00755×10^{-3}
b_3	-	-	2.44308×10^{-4}
b_4	-	-	8.03615×10^{-6}

TABLE B.1: Padé coefficients for different winding number l with $N = 1$.

proximated by the product of each vortex provided that the vortices are well separated (intervortex length $l_v \gg \xi$), as shown in Fig B.1.
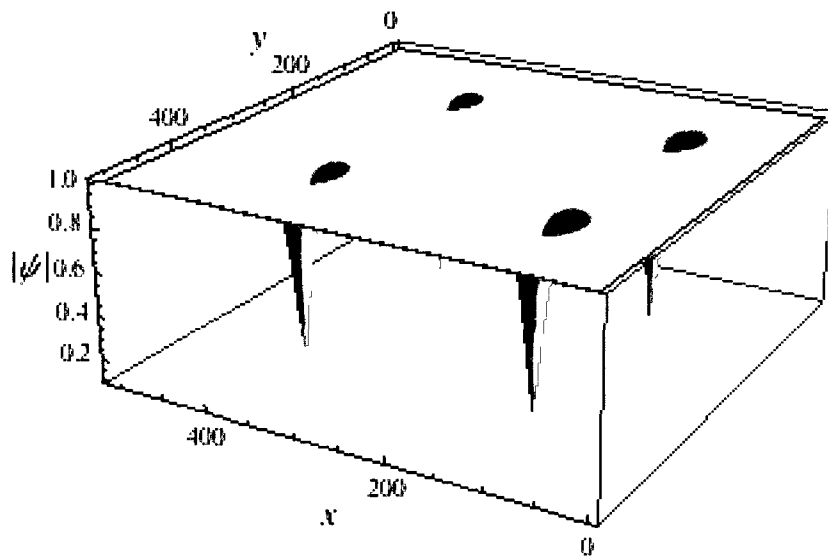
FIG. B.1: Pade approximation of 4 vortices.

Each vortex has winding number 1, spacial scaling $\Delta x = 0.1$, coupling constant $g = 1$. The underlining grid size is 512^2. Equivalently, the coherence length $\xi = 10$, which is much less than the intervortex distance $l_v = 256$.

BIBLIOGRAPHY

[1] T.-L. Horng, C.-H. Hsueh, S.-W. Su, Y.-M. Kao, and S.-C. Gou, Phys. Rev. A **80**, 023618 (Aug 2009).

[2] G. Vahala, J. Yepez, and L. Vahala, Physics Letters A **310**, 187 (2003).

[3] R. Feynman, R. Leighton, and M. Sands, *The Feynman Lectures on Physics* (Addison Wesley, 2006).

[4] M. Tsubota, ArXiv e-prints **21** (Apr. 2009), 0901.4600.

[5] W. F. Vinen, Journal of Low Temperature Physics **145**, 7 (November 2006).

[6] E. A. L. Henn, J. A. Seman, G. Roati, K. M. F. Magalhães, and V. S. Bagnato, Phys. Rev. Lett. **103**, 045301 (Jul 2009).

[7] Y. Castin and R. Dum, Phys. Rev. Lett. **77**, 5315 (Dec 1996).

[8] C. Pethick and H. Smith, *Bose-Einstein condensation in dilute gases* (Cambridge University Press, 2002).

[9] N. G. Berloff, Journal of Physics A Mathematical General **37**, 1617 (Feb. 2004).

[10] C. Nore, M. Abid, and M. E. Brachet, Physics of Fluids **9**, 2644 (1997).

[11] L. D. Landau and E. M. Lifschitz, *Fluid mechanics*, 2nd ed. (Elsevier, 2007).

[12] A. N. Kolmogorov, Proceedings: Mathematical and Physical Sciences **434**, 9 (1991).

[13] A. N. Kolmogorov, Proceedings: Mathematical and Physical Sciences **434**, 15 (1991).

[14] H. Grant, R. Stewart, and A. Moilliet, Journal of Fluid Mechanics **12**, 241 (1962).

[15] R. H. Kraichnan, Physics of Fluids **10**, 1417 (1967).

[16] P. Kundu and I. Cohen, *Fluid Mechanics* (Academic Press, 2002).

[17] G. K. Batchelor, Physics of Fluids **12**, II (1969).

[18] C. V. Tran and J. C. Bowman, Physica D Nonlinear Phenomena **176**, 242 (Mar. 2003).

[19] E. Kozik and B. Svistunov, Phys. Rev. B **77**, 060502 (Feb 2008).

[20] M. Machida, N. Sasa, T. Kano, V. S. L'vov, O. Rudenko, and M. Tsubota, ArXiv e-prints(Aug. 2010), arXiv:1008.3050.

[21] V. S. L'vov, S. V. Nazarenko, and O. Rudenko, Phys. Rev. B **76**, 024520 (Jul 2007).

[22] M. Kobayashi and M. Tsubota, Phys. Rev. Lett. **94**, 065302 (Feb 2005).

[23] R. Numasato, M. Tsubota, and V. S. L'vov, ArXiv e-prints(Feb. 2010), arXiv:1002.3667.

[24] N. G. Parker and C. S. Adams, Phys. Rev. Lett. **95**, 145301 (Sep 2005).

[25] D. A. Wolf-Gladrow, *Lattice-Gas Cellular Automata and Lattice Boltzmann Models: An Introduction* (Springer, 2000).

[26] S. Succi, *The Lattice Boltzmann Equation for Fluid Dynamics and Beyond (Numerical Mathematics and Scientific Computation)* (Oxford University Press, USA, 2001).

[27] P. L. Bhatnagar, E. P. Gross, and M. Krook, Phys. Rev. **94**, 511 (May 1954).

[28] B. R. Keating, *Methods for stabilizing high Reynolds number Lattice Boltzmann simulation*, Ph.d.dissertation, The College of William and Mary (Jul 2008).

[29] S. S. Chikatamarla, S. Ansumali, and I. V. Karlin, Physical Review Letters **97**, 010201 (2006).

[30] B. Keating, G. Vahala, J. Yepez, M. Soe, and L. Vahala, Physical Review E **75**, 036712 (2007).

[31] L. Zhong, S. Feng, P. Dong, and S. Gao, Physical Review E **74**, 036704 (2006).

[32] Y. S. Kivshar and D. E. Pelinovsky, Physics Reports **331**, 117 (2000).

[33] P. A. E. M. Janssen and J. J. Rasmussen, Physics of Fluids **26**, 1279 (1983).

[34] B. M. Boghosian and W. Taylor, Phys. Rev. E **57**, 54 (Jan 1998).

[35] J. Yepez and B. Boghosian, Computer Physics Communications **146**, 280 (2002).

[36] J. Yepez, G. Vahala, and L. Vahala, ArXiv e-prints(May 2009), arXiv:0905.0886.

[37] J. Yepez, G. Vahala, L. Vahala, and M. Soe, Phys. Rev. Lett. **103**, 084501 (Aug 2009).

[38] W. H. Press, S. A. Teukolsky, W. T. Vetterling, and B. P. Flannery, *Numerical recipes in C (2nd ed.): the art of scientific computing* (Cambridge University Press, New York, NY, USA, 1992).

[39] R. Keys, IEEE transactions on Signal Processing, Acoustics, Speech, and Signal Processing **29** (1981).

[40] G. Vahala, J. Yepez, L. Vahala, M. Soe, B. Zhang, and S. Ziegeler, "Poincare recurrence and intermittent loss of kelvin wave cascades in quantum turbulence," (2011), to appear in Phys.Rev.A.

[41] H. Takeuchi, N. Suzuki, K. Kasamatsu, H. Saito, and M. Tsubota, Phys. Rev. B **81**, 094517 (Mar 2010).

[42] W. Bao, D. Jaksch, and P. A. Markowich, Journal of Computational Physics **187**, 318 (May 2003).

[43] M. Leadbeater, T. Winiecki, D. C. Samuels, C. F. Barenghi, and C. S. Adams, Phys. Rev. Lett. **86**, 1410 (Feb 2001).

[44] H. Goldstein and C. P. Poole, *Classical Mechanics* (Addison Wesley, 2001).

VITA

Bo Zhang

Bo Zhang was born in Tai An, Shandong Province, China, on November 21, 1982. After finishing high school in 2000, he entered Beijing Normal University to study physics and received his B.S. degree in 2004. Upon finishing undergraduate study, he came to Unite States to pursue Ph.D. in physics in College of William and Mary. He received M.S. in College of William and Mary in 2006 and obtained his Ph.D. in August, 2011.